

<https://doi.org/10.15388/vu.thesis.801>

<https://orcid.org/0000-0001-8555-5803>

VILNIUS UNIVERSITY

CENTER FOR PHYSICAL SCIENCES AND TECHNOLOGY

Žygimantas Vosylius

# Characterization and Mitigation of Mismatch Effects in Solar Cell Testing Using Advanced LED-based Solar Simulators

**DOCTORAL DISSERTATION**

Natural Sciences,  
Physics (N 002)

VILNIUS 2025

The dissertation was prepared between 2019 and 2024 at the Institute of Photonics and Nanotechnology, Faculty of Physics, Vilnius University.

**Academic Supervisor** – Prof. Dr. Vincas Tamošiūnas (Vilnius University, Natural Sciences, Physics, N 002)

This doctoral dissertation will be defended in a public meeting of the Dissertation Defense Panel:

**Chairman** – Prof. Dr. Nerija Žurauskienė (Center for Physical Sciences and Technology, Natural Sciences, Physics, N 002).

**Members:**

Dr. Kristijonas Genevičius (Vilnius University, Natural Sciences, Physics, N 002).

Prof. Dr. Jonas Gradauskas (Vilnius Gediminas Technical University, Natural Sciences, Physics, N 002).

Prof. Dr. Vygintas Jankauskas (Vilnius University, Natural Sciences, Physics, N 002).

Dr. Pāvels Onufrijevs (Riga Technical University, Latvia, Natural Sciences, Physics, N 002).

The dissertation will be defended at a public meeting of the Dissertation Defense Panel at 11.00 on 10<sup>th</sup> September 2025 in conference room A101 of the National Center for Physical Sciences and Technology.

Address: Saulėtekio ave., Vilnius, Lithuania  
Tel. +370 5 264 9211; e-mail: [office@ftmc.lt](mailto:office@ftmc.lt)

The text of this dissertation can be accessed at the library of Vilnius University as well as on the website of Vilnius University:

<https://www.vu.lt/naujienos/ivykiu-kalendorius>

<https://doi.org/10.15388/vu.thesis.801>

<https://orcid.org/0000-0001-8555-5803>

VILNIAUS UNIVERSITETAS  
FIZINIŲ IR TECHNOLOGIJOS MOKSLŲ CENTRAS

Žygimantas Vosylius

# Inovatyvūs saulės imitatoriai saulės elementų testavimui, naudojant didelės galios šviestukus: spektrų nesutapimo įtakos tyrimai ir mažinimas

**DAKTARO DISERTACIJA**

Gamtos mokslai,  
Fizika, (N 002)

VILNIUS 2025

Disertacija rengta 2019–2024 metais Vilniaus universiteto Fizikos fakulteto Fotonikos ir nanotechnologijų institute.

**Mokslinis vadovas** – prof. dr. Vincas Tamošiūnas (Vilniaus universitetas, gamtos mokslai, fizika, N 002)

Gynimo taryba:

**Pirmininkė** – prof. dr. Nerija Žurauskienė (Fizinių ir technologijos mokslų centras, gamtos mokslai, fizika, N 002).

**Nariai:**

Dr. Kristijonas Genevičius (Vilniaus universitetas, gamtos mokslai, fizika, N 002).

Prof. dr. Jonas Gradauskas (Vilniaus Gedimino technikos universitetas, gamtos mokslai, fizika, N 002).

Prof. dr. Vygintas Jankauskas (Vilniaus universitetas, gamtos mokslai, fizika, N 002).

Dr. Pāvels Onufrijevs (Rygos technikos universitetas, Latvija, gamtos mokslai, fizika, N 002).

Disertacija ginama viešame Gynimo tarybos posėdyje 2025 m. rugsėjo mėn. 10 d. 11 val. Nacionaliniame fizinių ir technologijos mokslų centre (NFTMC), A101 auditorijoje.

Adresas: Saulėtekio al. 3, Vilnius, Lietuva  
tel. +370 5 264 9211; el. paštas [office@ftmc.lt](mailto:office@ftmc.lt)

Disertaciją galima peržiūrėti Vilniaus universiteto ir bibliotekoje ir VU interneto svetainėje adresu:

<https://www.vu.lt/naujienos/ivykiu-kalendorius>



## ACKNOWLEDGEMENT

I would like to express my sincere thanks to my supervisor Prof. Dr. Vincas Tamošiūnas for his help and dedication throughout all these years.

Also, I would like to thank Dr. Algirdas Novičkovas, Dr. Klemensas Laurinavičius, Darius Antonovič and Prof. Dr. Eugenijus Gaubas for their input in designing, constructing, and evaluating the simulators.

And finally, thanks to all colleagues and friends, especially Dr. Justina Anulytė, Dr. Ernesta Bužavaitė-Vertelienė, Kristina Aponienė, Dr. Vilius Vertelis, Dr. Tomas Daugalas and Dr. Dovydas Banevičius for sharing their academical and life experience as well as moral support.

## LIST OF ABBREVIATIONS

AM	Air Mass
ARC	Anti-reflective coating
BPC	Back Point Contact
BSF	Back Surface Field
CIGS	Copper Indium Gallium Selenide
<i>EQE</i>	External Quantum Efficiency
FWHM	Full-Width at Half-Maximum
IBC	Interdigitated Back Contact
IR	Infrared
LBIC	Light Beam Induced Current
LED	Light Emitting Diode
MCPCB	Metal Core Printed Circuit Board
<i>NU</i>	Non-uniformity
PECVD	Plasma-Enhanced Chemical Vapor Deposition
PERC	Passivated Emitter and Rear Cell layer
PV	Photovoltaic
a-Si	Amorphous silicon
c-Si	Crystalline silicon
mc-Si	Multi-crystalline silicon
poly-Si	Poly-crystalline silicon
$\mu$ c-Si	Micro-crystalline silicon
<i>SID</i>	Spectral Irradiance Deviation (interval-wise)
SLG	Soda-lime glass
<i>SMM</i>	Spectral Mismatch
<i>SPC</i>	Spectral Coverage
<i>SPD</i>	Spectral Deviation
<i>SR</i>	Spectral Responsivity
STC	Standard Test Conditions
TCO	Transparent Conductive Oxide
<i>TI</i>	Temporal Instability
TOPCon	Tunnel Oxide Passivating Contact
UV	Ultraviolet

## CONTENTS

INTRODUCTION.....	9
Main goal.....	10
Objectives.....	10
Novelty and relevance .....	11
Layout of the thesis .....	11
Author contribution .....	12
Thesis statements.....	13
LIST OF PUBLICATIONS.....	14
1   LITERATURE REVIEW .....	16
1.1   Solar cells.....	16
1.2   Solar simulators .....	30
1.3   LED-based solar simulators .....	36
1.4   Standards for solar simulators.....	38
1.4.1 Spectral match.....	39
1.4.2 Spatial Non-Uniformity ( <i>NU</i> ).....	40
1.4.3 Temporal Instability.....	40
1.4.4 Spectral Coverage ( <i>SPC</i> ) and Spectral Deviation ( <i>SPD</i> ).....	41
1.4.5 Spectral Mismatch ( <i>SMM</i> ).....	42
2   METHODS .....	46
2.1   LEDs, Reflectors, and Data Sources for Simulations .....	46
2.2   Measurement system.....	46
2.3   Distribution simulation .....	47
2.4   Generating the spectra.....	49
2.5   Solar cell simulation .....	50
3   RESULTS AND DISCUSSION.....	53
3.1   First prototype of Solar Simulator with mirror system .....	53
3.1.1 Mirror system simulation.....	54
3.1.2 Light source geometry optimization .....	55
3.1.3 Optimization results .....	57
3.1.4 Adhering to the novel standard.....	62

3.2	Minimal set of light sources for A+ class solar simulators .....	62
3.2.1	LED-only solar simulator .....	63
3.2.2	Hybrid solar simulator .....	64
3.3	Reduction of <i>SMM</i> – 1 factor .....	65
3.3.1	c-Si .....	66
3.3.2	a-Si .....	70
3.3.3	CdTe .....	74
3.3.4	$\mu$ c-Si .....	78
3.4	Many light-source solution .....	82
3.5	Simultaneous optimization for multiple solar cell types .....	83
3.6	Solar cell response simulations .....	86
3.6.1	Surface recombination currents .....	87
3.6.2	Al-BSF solar cell .....	88
3.6.3	PERC solar cell .....	93
3.6.4	IBC solar cell .....	99
3.6.5	A comparison between different technologies .....	102
3.7	Manufacturability of proposed designs .....	105
4	CONCLUDING STATEMENTS .....	109
5	LIST OF REFERENCES .....	112
APPENDIX .....		124
A1. Properties of simulator configurations with abbreviated names ....		124
A2. Models of considered light sources. ....		125
A3. Examples of MATLAB scripts .....		126
SANTRAUKA .....		130

## INTRODUCTION

Solar simulators are devices that allow for controllable measurement of the properties of solar cells under indoor conditions. Several kinds of lamps can be used as light sources with suitable filters, such as various gas discharge lamps, halogen lamps, light emitting diodes (LEDs), and their combinations [1].

In one of the first works in which 1 Sun irradiance was achieved within a  $200\text{ mm} \times 200\text{ mm}$  area, LEDs were used to augment the spectrum of halogen emitters in the 375 nm to 680 nm spectral range and provided up to  $590\text{ W/m}^2$  irradiance [2]. The growing availability of high-power LED devices has led to multiple and sometimes divergent optimization pathways. An LED-only solar simulator for small laboratory devices of up to 5 cm in size was demonstrated using 19 LEDs of six different models with a significantly simplified light concentration solution based on individual reflectors for a part of the LED array in [3].

International Electrotechnical Commission standard IEC 60904-9 sets the requirements for solar simulators and was recently updated with the third edition [4]. According to the standard, three letters are used to classify the performance of the solar simulator according to spectral content, spatial uniformity, and temporal stability, respectively. Classes of A+, A, B, C, or U (unclassified) are assigned based on each of these three characteristics, defining a three-letter performance rating for the device.. The spectral content is evaluated in six spectral ranges within 300 nm to 1200 nm, according to the latest standard version. However, an older specification of ranges within 400 nm to 1100 nm is also provided for backward compatibility reasons.

Rapid developments of high-power LED technology and availability of high-efficiency LEDs in multiple spectral ranges paved the way for compact, low power-consumption, scalable, highest-class LED-only simulators. However, the discreteness of LED spectra and a lack of effective IR devices opens new challenges in spectral mismatch domain.

Geometrical properties of solar simulator optical systems, and possible spectral mismatch scenarios promoted by the fluctuation of physical parameters in various types of solar cells may result in discrepancies between the cell's working conditions under the Sun and a solar simulator. Numerical exploration of these phenomena provides insight on how to reduce undesirable errors and inconsistencies.

## Main goal

The main goal of this study is to develop and demonstrate novel LED-only and hybrid solar simulators matching at least AAA-class requirements with the least possible number of types of light sources, to investigate the spectral mismatch effects for multiple solar cell types, and to propose comprehensive strategies to reduce the influence of these spectral mismatch effects.

## Objectives

1. Design and demonstrate an AAA class LED-based solar simulator for 5-inch or larger industrial solar cells with the least possible number of types of industrially available light sources, preferably with only one kind per interval defined in IEC 60904-9;
2. Develop algorithms of rational management of LED-based and hybrid solar simulator spectra for minimizing the effects caused by spectral mismatch in cases of crystalline silicon (c-Si), amorphous silicon (a-Si), cadmium telluride (CdTe), and microcrystalline silicon ( $\mu$ c-Si) solar cells of standardized spectral responsivity as defined in IEC 60904-9 standard;
3. Verify the robustness of developed spectral mismatch effect reduction techniques by performing a comprehensive series of simulations for multiple industrial solar cell types, including the specific influences of doping changes, recombination parameters, and substrate thickness changes.

## Novelty and relevance

A novel, modular, and scalable design of AAA-class LED-only solar simulators was demonstrated, allowing for testing of industrial solar cells up to 5 inches in diameter with just 22 LED devices. This design allows for cost-effective and efficient testing of solar cells of different sizes or module configurations. This flexibility is significant for research and development in photovoltaic technologies, where diverse testing conditions are often required.

Peculiarities of photocurrent deviations, spectral coverage changes, and spectral mismatch effects were studied in detail for multiple solar cell technologies in the context of testing with LED-based solar simulators. An efficient pathway to the near elimination of spectral mismatch effects is revealed for the dominating type of industrial solar cells – crystalline silicon-based ones. It is demonstrated that such an effect can be achieved with a very targeted application of just two additional kinds of LED sources of 365 nm and 1050 nm peak wavelengths. A similar efficient technique based on the application of UV LEDs was also proposed for CdTe and microcrystalline silicon types.

Detailed simulation series of physical phenomena occurring in solar cells when changing doping concentrations, absorbers' thicknesses, and carriers' lifetimes under illumination of LED-based solar simulators were performed. Results of these simulations reveal that the validity of the proposed spectral mismatch effect mitigation techniques extends way further than the simplified models of the current IEC 60904-9:2020 standard requires.

## Layout of the thesis

This thesis consists of an Introduction, Literature Review and Methodology chapters followed by Results and Discussion, as well as Concluding Statements.

In Literature Review (Ch. 1) the designs of solar cells and solar simulators are briefly discussed, with more emphasis on silicon-based solar cells and LED-based solar simulators. Moreover, novel standards for solar simulators' specifications are presented with details on verification of various parameters.

The Methodology chapter (Ch. 2) overviews the data and tools required for the simulations of irradiance and spectral distributions of a solar simulator model as well as  $E_{QE}$  and  $j-V$  calculations for a given solar cell design under the proposed simulator's irradiance. Measurement system, used to characterize constructed designs of solar simulators is reviewed as well.

The Results and Discussion (Ch. 3) consists of three main parts over seven subsections. Chapter 3.1 examines the construction and steps for improvement of a scalable LED-only solar simulator designs employing double reflectors. Chapters 3.2 – 3.5 delve into minimization of spectral mismatch induced effects for modeled LED-only and Hybrid (halogen enhanced) solar simulators using the least possible number of distinct irradiance sources in cases of virtual spectral responsivities of c-Si, a-Si,  $\mu$ c-Si and CdTe solar cells. Chapter 3.6 investigates the influence of physical parameters of silicon solar cells on the spectral mismatch induced effects under the illumination of previously optimized spectra. The effects of doping concentration, absorbers' thickness, and carriers' lifetime variation in Al-BSF, PERC and IBC solar cells are studied.

The Concluding Statements (Ch. 4) summarize the results obtained by the irradiance and spectral distribution simulations as well as simulations of solar cell physical properties' variations.

### Author contribution

The author has designed the first prototype of a solar simulator used in this work and measured irradiance and spectral distributions of the generated illumination. The Author also made all ray-tracing, spectral distribution, and solar cell response simulations, using POV-Ray, MATLAB, and PC3D software.

The conceptualization and methodology were developed by Prof. Dr. Vincas Tamošiūnas (Institute of Photonics and Nanotechnology, Vilnius University); both the first and the second simulator designs were constructed by Dr. Algirdas Novičkovas (Institute of Photonics and Nanotechnology, Vilnius University); the second simulator design was finalized by Dr. Klemensas Laurinavičius (the Center for Physical Sciences and Technology), and simulations of solar cell response using TCAD software were made by Darius Antonovič and Prof. Dr. Eugenijus Gaubas (Institute of Photonics and Nanotechnology, Vilnius University).



## Thesis statements

1. Only 22 LEDs are necessary to illuminate an area of  $14\text{ cm} \times 16\text{ cm}$  according to requirements for AAA class solar simulators in the 400 nm to 1100 nm spectral range, with a new simulator design proposed in this thesis and related publication.
2. A+ class spectrum as defined in IEC 60904-9:2020 can be composed by employing only four types of high-power industrial LEDs (cool white, 740 nm, 850 nm, and 1050 nm).
3. Spectral mismatch errors  $SMM - 1$  can be reduced by at least an order of magnitude by adding two additional 365 nm and 940 nm LED types to the first minimum set in the case of c-Si solar cells.
4. The same set of six source types can also be optimized for CdTe and  $\mu\text{c-Si}$  solar cells, allowing for lower  $SMM - 1$  values in comparison with commercial Xe-lamp based solar simulators.
5. Robustness of optimization results obtained with idealized external quantum efficiency spectra of IEC 60904-9:2020 is confirmed by more detailed simulations of the influence of doping changes, recombination parameters, and substrate thickness changes in the case of industrial c-Si solar cells.

## LIST OF PUBLICATIONS

### Basis of dissertation

[P1] Žygimantas Vosylius, Algirdas Novičkovas, Klemensas Laurinavičius, Vincas Tamošiūnas, “Rational Design of Scalable Solar Simulators With Arrays of Light-Emitting Diodes and Double Reflectors,” *IEEE Journal of Photovoltaics*, vol. 12, no. 2, pp. 512-520, 2022, doi: 10.1109/JPHOTOV.2021.3136783.

[P2] Žygimantas Vosylius, Algirdas Novičkovas, Vincas Tamošiūnas, “Optimization of LED-Based Solar Simulators for Cadmium Telluride and Microcrystalline Silicon Solar Cells,” *Energies*, vol. 16, no. 15, pp. 1-15, 2023, doi: 10.3390/en16155741.

[P3] Žygimantas Vosylius, Darius Antonovič, Algirdas Novičkovas, Eugenijus Gaubas, Vincas Tamošiūnas, “Rational selection of light sources for LED-based solar simulators,” *Solar Energy*, vol. 265, 2023, doi: 10.1016/j.solener.2023.112064.

### Other publication

[P4] Vincas Tamošiūnas, Andrzej Urbanowicz, Žygimantas Vosylius, Gintautas Tamulaitis, “Terahertz tomography for testing wrapped scintillating crystals,” *Radiation Physics and Chemistry*, vol. 226, 2025, doi: 10.1016/j.radphyschem.2024.112176.

## List of conference presentations

[C1] Žygimantas Vosylius, Algirdas Novičkovas, Vilius Kavaliauskas, Klemensas Laurinavičius, Vincas Tamošiūnas, “Scalable solar simulators based on arrays of light-emitting diodes,” *Functional Materials and Nanotechnologies FM&NT-2020*, Vilnius, Lithuania, November 23-26, 2020. Poster session online.

[C2] Žygimantas Vosylius, Algirdas Novičkovas, Vincas Tamošiūnas, “Material dependent peculiarities of testing solar cells using solar simulators based on light emitting diodes (LEDs),” *Advanced Materials and Technologies 2022*, Palanga, Lithuania, August 22-25, 2022. Poster session.

[C3] Žygimantas Vosylius, Vincas Tamošiūnas, Maksim Jemeljanov, Gintautas Tamulaitis, “Radiometric imaging and pulsed X-ray-based studies of light collection from scintillating crystals,” *Advanced Properties and Processes in Optoelectronic Materials and Systems*, Vilnius, Lithuania, October 5-7, 2022. Poster session.

# 1 LITERATURE REVIEW

## 1.1 Solar cells

Solar cells are photovoltaic (PV) devices that convert sunlight, the greatest energy source on Earth, directly to electricity without any intermediate heat engine or revolving mechanism. PV modules have no moving parts, minimizing maintenance requirements and prolonging lifetime, while generating electricity without producing greenhouse or any other gases nor noise.

The global PV cumulative capacity grew from 1.2 TW in 2022 to 1.6 TW in 2023, accounting for 13 % of total renewable energy generation (including hydroelectric and nuclear energy) and 5.3 % of total global electricity generation [5]. China alone has experienced immense growth in this field during the last decade. In 2023, it contributed 662 GW (or over 40 %) cumulative PV capacity and 120 % domestic growth of 235 GW new PV installations [6]. During this period, the EU commissioned 61 GW of new PV systems, totaling around 300 TW of cumulative PV capacity.

With global surface temperature and energy-related greenhouse gas emissions still reaching record highs every year (+1.28°C [7] and 40 GtCO<sub>2e</sub> [5] accordingly), renewable energy remains one of the greatest solutions to combat climate change. Therefore, the research on PV devices and their complement systems, such as solar simulators, power converters, storage devices, and energy transmission networks, is increasingly topical.

Even for a perfect solar cell, its maximum efficiency  $\eta$  and photocurrent are still limited by semiconductors bandgap, carrier recombination, and the fact that, while blue light has roughly twice the energy of red light, one photon still generates one free electron with the excessive energy being lost as heat. For a single junction solar cell with a specified bandgap energy, the maximum light to electric power conversion efficiency is known as detailed balance limit or Shockley-Queisser limit. Assuming that photons with lower energy than the bandgap energy do not interact with the solar cell, the photons with the energy above the bandgap energy are perfectly converted into electron-hole pairs, the temperature of a cell is 298.15 K, and it is illuminated by a standard AM1.5G solar spectrum [8] – the theoretical maximum limit of the solar cell parameters as a function of the bandgap can be calculated [9]. As seen in Fig. 1(a), the theoretical maximum efficiency for single junction cell is  $\eta = 33.16$  % in a semiconductor with  $E_g = 1.34$  eV bandgap.

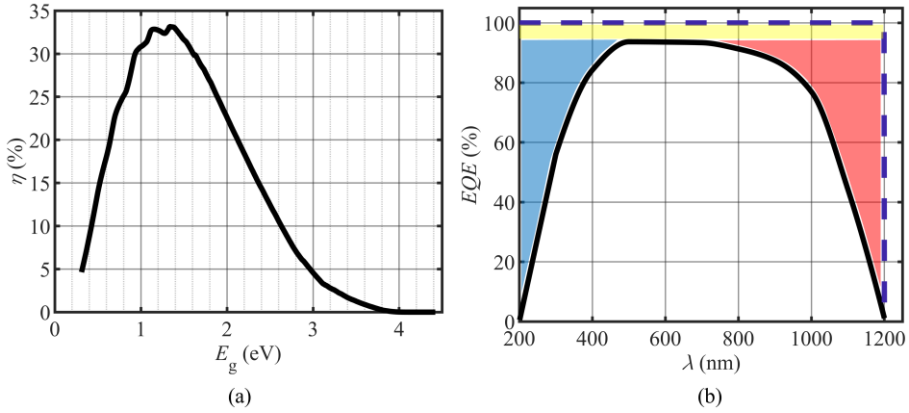


Fig. 1. (a) The theoretical maximum limit of the solar cell parameters as a function of the bandgap [9], and (b) external quantum efficiency for the ideal (dashed blue line) and real (solid black line) photodetector.

Nevertheless, the real-life PV devices are not ideal, and the number of charge carriers collected by the electrodes of the device is smaller than the number of incident photons on its surface. The ratio of these numbers is called External Quantum Efficiency (EQE) [10]. While quantum efficiency ideally has the square shape, dropping to zero at the wavelength, corresponding to the bandgap energy of a given material (Fig. 1(b), dashed blue line), it is reduced: at shorter wavelengths due to front surface recombination (Fig. 1(b), blue area); at longer wavelengths due to rear surface recombination and low diffusion lengths (Fig. 1(b), red area); and overall reduction of quantum efficiency can be caused by reflections, shading and low diffusion lengths (Fig. 1(b), yellow area).

All the differences in the configurations and material properties of the solar cells results in wide variety of the devices and their efficiencies.

### Crystalline silicon (c-Si)

The first ever solar cell was developed at Bell Laboratories using crystalline silicon [11]. It already showed an approximately 6 % conversion rate, delivering power from the sun into the load at a  $60 \text{ W/m}^2$  rate and exceeding the previously shown efficiency of the thermoelectric junction six-fold [12]. Nowadays, c-Si solar cells still play a particularly significant role in the photovoltaics market. In 2023, Si-wafer-based PV technology accounted for about 97 % of total production [13] and is becoming even more dominant every year. China alone has produced 271 GW of c-Si solar modules during H1 2024 [14].

As the name suggests, crystalline silicon technology employs wafers with an ordered crystal structure and as few grain boundaries and impurities as possible. They typically have better material parameters but are also more expensive. Czochralski process [15] is a commonly adopted method to crystallize such wafers as it provides relatively large scale, low impurity monocrystal – perfect properties for industrial wafer slicing. Still, this method is slow and expensive, and it incorporates oxygen into the ingot, which then creates complexes with the boron dopant, degrading the carrier lifetime [16]. In laboratory setups or niche markets, where higher purity of ingots is needed, other wafering techniques, such as Float Zone (FZ) [17] or Edge Defined Film Fed Growth (EFG), can be deployed [18].

Another advantage of crystalline silicon, and probably the main reason for its early adoption, is its broad absorption spectrum, which effectively encompasses most of the solar emission spectrum. The absorption coefficient of intrinsic silicon at 300 K compared to the AM1.5G solar spectrum is presented in Fig. 2.

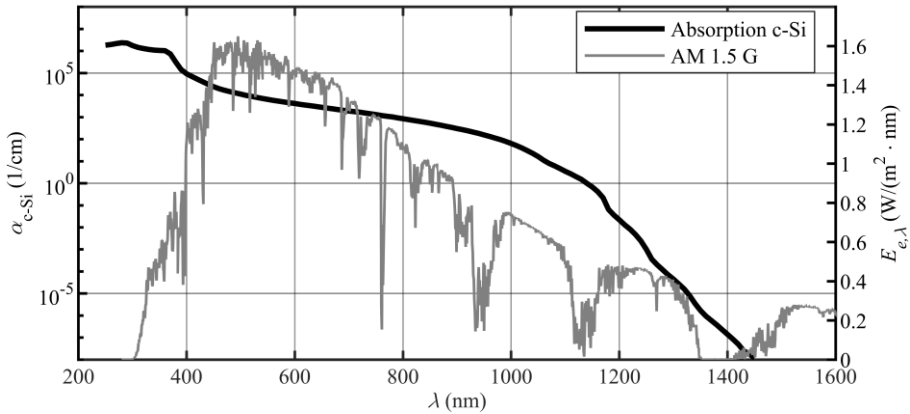


Fig. 2. Absorption spectrum of intrinsic silicon at 300 K [19] and AM1.5G reference solar spectrum.

As a result of the colossal usage of c-Si, the effort to maximize efficiency provides several different architectures of cells as well as hybrid ones, employing different principles on the same device. For a long time, Back Surface Field (BSF) technology has been the leading choice in the market. BSF reduces surface recombination velocity by creating an electric field, which presents a barrier for minority carriers, maintaining their concentration in the bulk of the device. A typical Al-BSF solar cell structure is presented in Fig. 3.

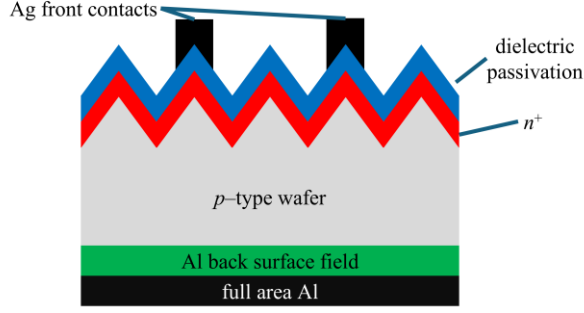


Fig. 3. Schematic of aluminum back surface field solar cell. (adapted from [20])

Starting around 2013, BSF technology gradually gave way to other technologies, eventually occupying a negligible market share in 2023. The main contender, most popular nowadays, is Passivated Emitter and Rear Cell (PERC) technology (Fig. 4). This architecture adds an aluminum oxide passivation layer and silicon nitride anti-reflective coating to the rear side of the device. Moreover, aluminum alloyed local contacts are being used instead of full area contact, which, together with the dielectric layer, further reduces unwanted recombination and allows up to 25 % efficiency in the laboratory [21].

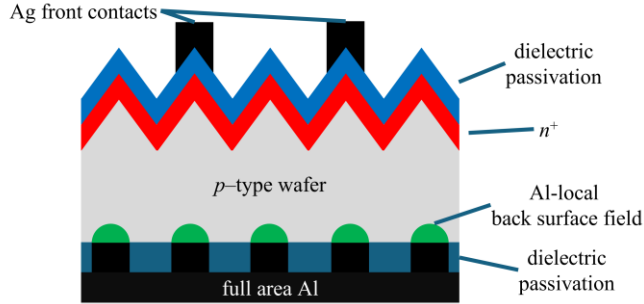


Fig. 4. Schematic of passivated emitter rear contact (PERC) solar cell. (adapted from [20])

Novel c-Si solar cell architectures are going even further regarding the passivation layers. Auger recombination, free carrier absorption, and bandgap narrowing are still the main issues with Al-BSF and PERC solar cells [22]. Solar cells with carrier-selective passivating contacts (CSPCs) aim to address these problems effectively. A notable example is the architecture, employing Tunnel Oxide Passivating Contacts (TOPCon) [23] (Fig. 5) combined with heavily doped Si thin film as a full-area electron contact in an n-type c-Si solar cell with boron-doped front side emitter. With this type of cell structure, efficiencies of up to 25.1 % are reported [24]. Moreover, the market share of

passivated contacts on  $n$ -type Si technologies is rapidly growing, and has already exceeded 25 % in 2023 [13].

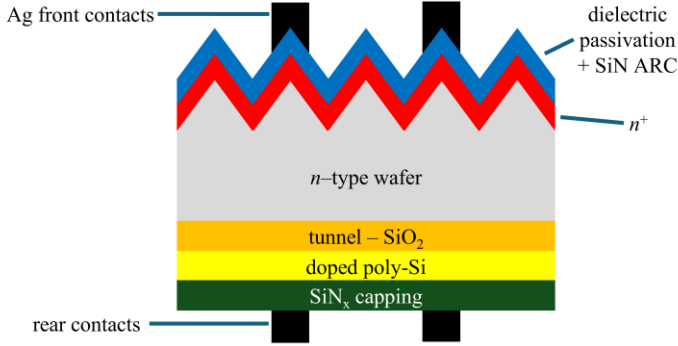


Fig. 5. Schematic view of TOPCon solar cell. (adapted from [23])

One more approach to greater efficiencies exploits architecture with all or part of the front contact grids moved to the rear of the device. In this case, the hole-electron pairs are generated in a bulk region with a very high carrier lifetime. They are collected at interdigitated, heavily doped junctions on the back side of the cell. Thus, this device is called an *Interdigitated Back Contact* (IBC) solar cell [25, 26] (Fig. 6). Localized back contacts with reduced contact recombination losses, gridless front surface granting more light to pass to the absorption layer, backside metallization providing internal rear surface reflection and very low series resistance are the key design features contributing to the high efficiency of this architecture [27]. The contacts being on one side of the device also eases electrical mounting and maintenance.

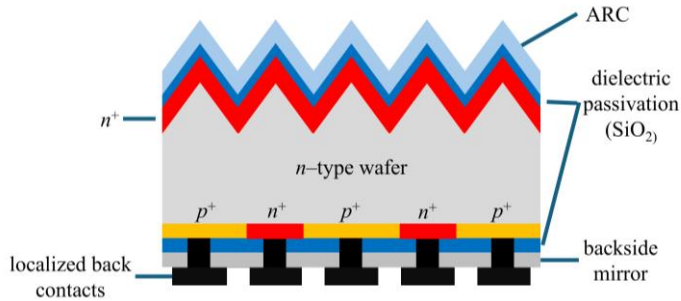


Fig. 6. Schematic view of an IBC solar cell. (adapted from [26])

Moreover,  $n$ -type wafers are used in IBC cells, which, unlike  $p$ -type ones, do not suffer from light-induced degradation and are less sensitive to impurities such as iron, resulting in cheaper and easier fabrication of  $n$ -type silicon. On the other hand, the doping is less homogeneously distributed across the wafer, compared to  $p$ -type silicon, leading to varying electronic



properties within one wafer and lowering the yield of solar cell production [26]. Nonetheless, improvements in the areas of edge loss, series resistance, and emitter recombination have led to IBC solar cells with a total area efficiency of 25 % [23], and the steadily growing employment of this technology during the last decade has resulted in taking around 5 % of the market share in 2023 [13].

### *Multicrystalline silicon (mc-Si)*

Multicrystalline silicon is a lower-quality material version of crystalline silicon. If an ideal c-Si ingot comprises an ideal lattice, mc-Si, by definition, consists of separate grains (1 mm – 10 cm of size [28]). Grain boundaries introduce extra defect energy levels, resulting in highly localized recombination regions and reduced minority carrier lifetime. Additionally, grain boundaries can block carrier flow and create shunting paths, allowing current flow across the  $p$ - $n$  junction, thus further decreasing solar cell performance.

Anyhow, techniques to produce mc-Si wafers are much simpler and cheaper than those used in c-Si manufacturing. A big slab of multicrystalline silicon can be grown in a crucible just by melting silicon and then slowly but precisely cooling it down. Of course, more sophisticated growing techniques and finer grain control allow better performance, such as directional solidification [29], or lowering grain size, creating so-called *polycrystalline silicon* (poly-Si), consisting of many small crystalline grains (1  $\mu\text{m}$  – 1 mm of size), with random orientations. Poly-Si can also be produced into relatively thin films, enabling combinations with other Si technologies, although it presents some parasitic absorption, for which more research is needed [30].

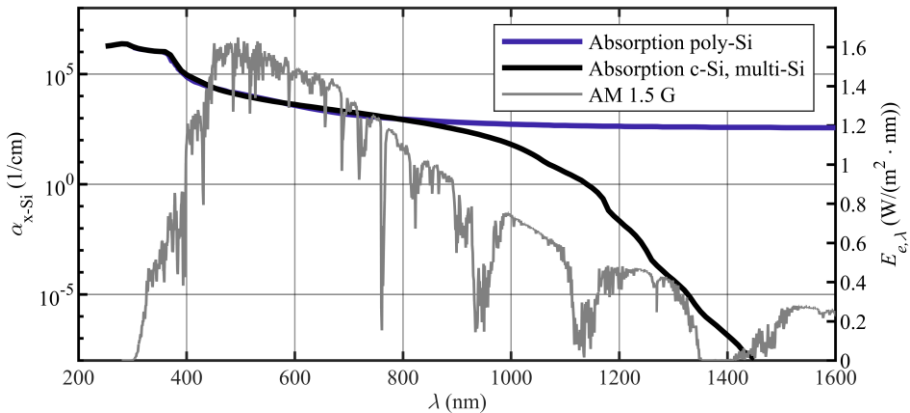


Fig. 7. Absorption spectrum of polycrystalline silicon [30] in comparison with c-Si and multi-Si absorption and AM1.5G reference solar spectra.

Solar cell technologies for mc-Si are similar to those of c-Si, while the cost of mc-Si wafer production was historically cheaper. This solar cell technology has reached efficiencies of 24.4 % [31] and 70 % of global annual production in 2015 [13]. However, advancements of the Czochralski method lowered the c-Si wafer price, resulting in only < 1 % global annual production of mc-Si solar cells in 2023.

### *Amorphous silicon (a-Si)*

Amorphous silicon (a-Si) is a non-crystalline material with no long-range order (Fig. 8). The lack of order results in many dangling bonds serving as the recombination centers, severely reducing the carrier lifetime – one of the main parameters for carrier separation in solar cells. Moreover, these dangling bonds, existing at the order of  $10^{19}/\text{cm}^3$ , pin the Fermi energy level so that the material cannot be doped either *p*-type or *n*-type [32]. This can be solved by incorporating hydrogen atoms in a film during deposition, reducing defect density to  $10^{16}/\text{cm}^3$ , resulting in hydrogenated amorphous silicon (a-Si:H).

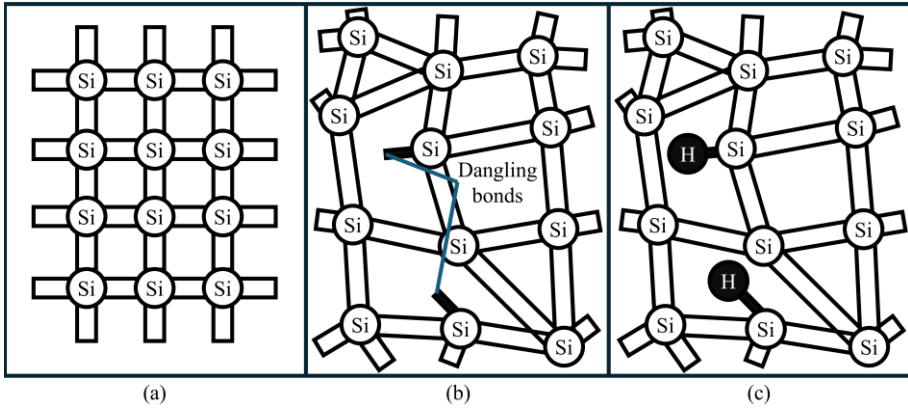


Fig. 8. Schematic structure diagrams of (a) crystalline silicon, (b) amorphous silicon, and (c) hydrogenated amorphous silicon. (adapted from [33])

Hydrogenating amorphous silicon during its deposition using PECVD to about 10% of hydrogen concentration also allows doping with phosphorus (P) and boron (B). Nevertheless, while hole and electron densities are on the same order of magnitude in the intrinsic layer, allowing reasonable drift of carriers through the layer, the diffusion length in doped layers is still low. That is why a simple device based on a-Si usually has a *pin*-type structure. Intrinsic a-Si is a relatively thick (hundreds of nanometers) absorption layer sandwiched between thin (10 nm) *p*- and *n*-doped extraction layers. The doped layers also create an electric field across the intrinsic layer, resulting in a so-called *drift device*, as illustrated in Fig. 9(b).

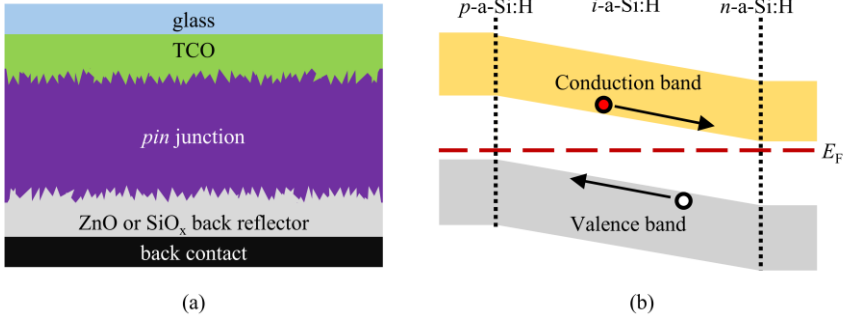


Fig. 9. (a) Schematic view of an example amorphous silicon solar cell and (b) its band diagram. (adapted from [26])

Amorphous silicon is usually employed in thin film solar cells. As mentioned before, *p*-type and *n*-type extraction layers must be at most tens of nanometers thick, and the thickness of the intrinsic layer is chosen as a compromise between enhancement of absorption and shortening the distance for photogenerated carriers to reach the electrodes. Moreover, a-Si:H suffers from light-induced creation of metastable defects, known as the Staebler–Wronski effect, which additionally requires thinning out the absorption layer. While a-Si:H has a well-defined optical threshold at only 1.75 eV ( $\sim 700$  nm), it also has an order of magnitude larger absorption coefficient than c-Si for photons with wavelength  $< 690$  nm (Fig. 10).

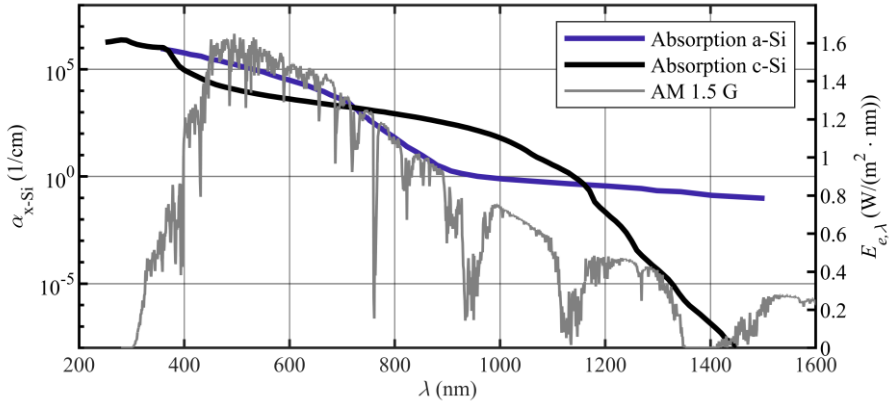


Fig. 10. Absorption spectrum of amorphous silicon [34] in comparison with c-Si absorption and AM1.5G reference solar spectra.

Good photon absorbance, lower temperature coefficient, and the opportunity to manufacture thin film solar cells (Table 1), especially in tandem with other thin-film solar technologies, caught the interest of scientists and manufacturers. That is why a-Si-based technologies took around 9 % of global market share and peaked at more than 1 GW of annual PV module

production in 2011. Anyhow, other thin-film technologies, such as CdTe and CIGS, outcompeted amorphous silicon, resulting in a negligible share in global solar energy production, especially compared with c-Si technologies [13].

Table 1. Photovoltaic Properties for a-Si and c-Si solar cells [33].

Photovoltaic properties	a-Si:H	c-Si
Optical-Electrical Conversion Efficiency	14.0 %	22.3 % – 26.1 %
Bandgap	1.75 eV	1.1 eV
Sufficient Thickness	1~2 $\mu\text{m}$	100 $\mu\text{m}$
Spectral Range (75 % – 85 % QE)	550~700nm	440~650nm
Temperature Coefficient (above 25 % )	-0.2 – -0.25 %/°C	-0.41 – -0.5 %/°C
Area Required / kW ( $\text{m}^2$ )	15	7 – 8

### Microcrystalline silicon ( $\mu\text{c-Si}$ )

Microcrystalline silicon is a mixed-phase material consisting of a-Si:H, embedded nanosized crystallites or conglomerates of nanocrystallites, and grain boundaries. In most cases,  $\mu\text{c-Si:H}$  is grown by plasma-enhanced chemical vapor deposition (PECVD) [35, 36] or hot-wire CVD [37].

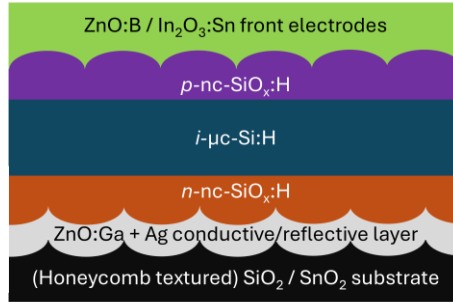


Fig. 11. Schematic view of an example  $\mu\text{c-Si}$ -based solar cell. (adapted from [38])

$\mu\text{c-Si}$  solar cells are another example of thin film cells that underwent significant modifications of the *EQE* spectrum during the last decade of research. The application of honeycomb-shaped textures to the back reflector led to a substantial increase in *EQE* in the 700 nm to 1100 nm range when compared to devices with a flat reflector (Fig. 11, Fig. 12), simultaneously increasing the efficiency of solar cells to 11.9 % [38]. Moreover,  $\mu\text{c-Si}$  has higher carrier mobility than a-Si and does not suffer from light-induced degradation. However, thicker films are required to utilize longer wavelengths of the irradiation, due to the indirect bandgap of silicon crystallites.

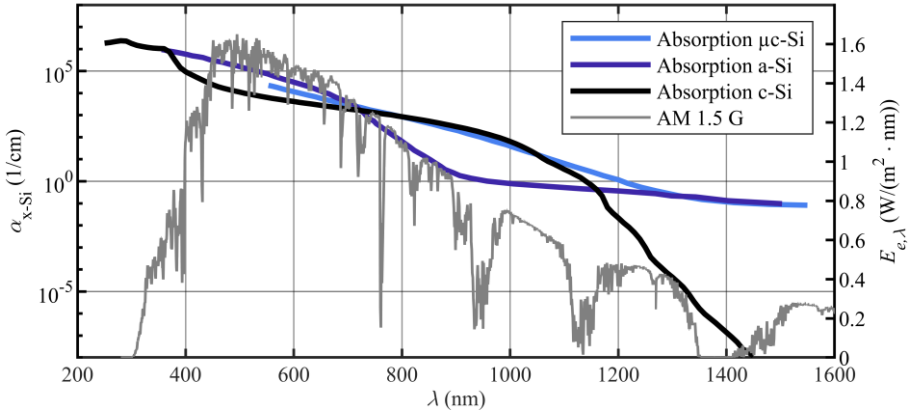


Fig. 12. Calculated optical absorption spectrum of  $\mu\text{c-Si}$ , using constant photoconductivity method (CPM) [39], in comparison with  $\text{c-Si}$ ,  $\text{a-Si}$  absorption, and AM1.5G reference solar spectra.

While neither  $\text{a-Si}$  nor  $\mu\text{c-Si}$  technologies can optimally utilize the solar spectrum, they can be combined into one multijunction cell [26] (Fig. 13). As usual in tandem cells,  $\text{a-Si:H}$  cell goes on top of the device to absorb higher energy photons, while the lower band-gap bottom  $\mu\text{c-Si}$  cell absorbs the red part of the irradiation spectrum.

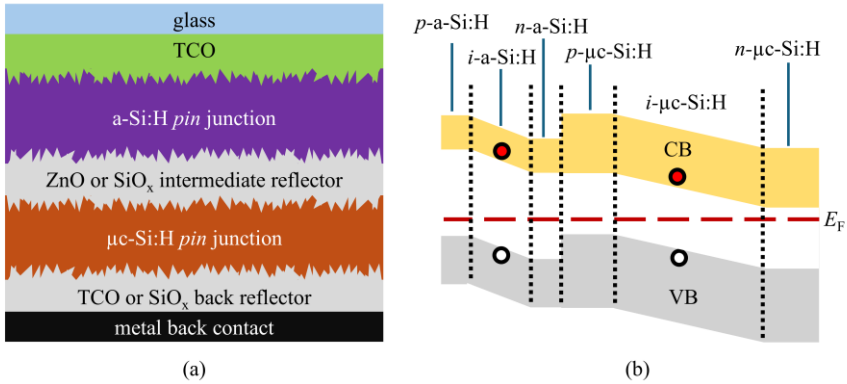


Fig. 13. (a) Schematic view and (b) the band diagram of an example MICROMORPH™ silicon solar cell. (adapted from [26])

One of the most studied concepts is MICROMORPH™ technology (Fig. 13, Fig. 14), in which, for example, 16 or more layers are stacked for the best solar spectrum utilization. A top cell, based on  $\text{a-Si}$  technology with its alloys in tandem with  $\mu\text{c-Si}$  bottom cell, can result in a 13.2 % efficient thin-film device as shown by *Cashmore et. al* [40], while up to 14 % efficiency can be reached through advanced light-trapping techniques [41].

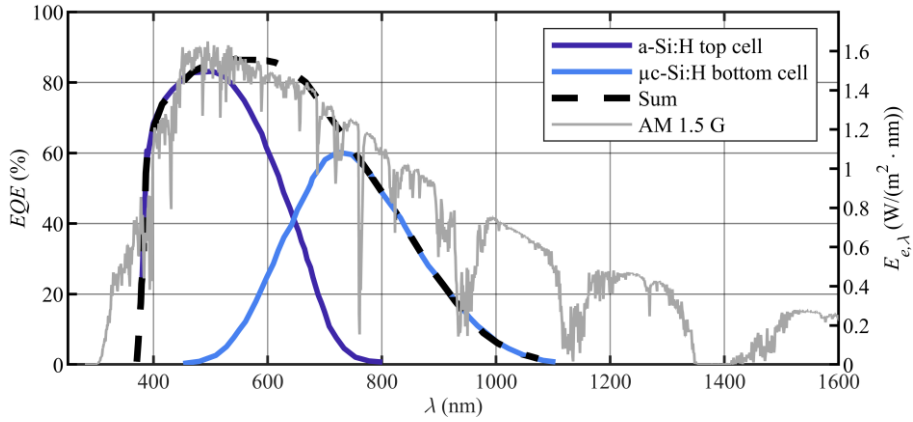


Fig. 14. EQE spectrum of a MICROMORPH™ tandem device (200 nm thick a-Si:H i-layer and 1500 nm thick  $\mu$ c-Si:H i-layer [40]), in comparison with an AM1.5G reference solar spectrum.

Anyhow, as other thin-film technologies showed more potential and greater efficiency, and crystalline silicon cell production skyrocketed during the late 2010s, the global market share of  $\mu$ c-Si and a-Si technologies dropped to negligible margins.

### Cadmium Telluride (CdTe)

The chalcogenides – II–VI, I–III–VI, perovskite and kesterite photovoltaic materials, such as CdTe,  $\text{Cu(In,Ga)Se}_2$ , methylammonium lead triiodide ( $\text{MAPbI}_3$ ) and  $\text{Cu}_2\text{ZnSn(S,Se)}_4$ , respectively, have direct bandgaps that enable light to be absorbed and converted into electricity in semiconductor layers that are just several micrometers thick [42, 43]. So far, more than 25 GW of CdTe-based solar technology has been installed [44], with cell efficiencies now reaching 22,1 % [45] and module efficiency averaging 17 – 18 % at costs competitive with Si modules [46].

CdTe solar cells can serve as a practical example of broadening the high-responsivity spectrum of experimentally demonstrated devices once new technological developments are introduced. In the past, devices of up to 16 % efficiency mostly relied on a relatively simple structure consisting of a copper-doped CdTe (CdTe:Cu) absorber and cadmium sulfide (CdS) buffer layers [26] (Fig. 15, Fig. 16). Current, more than 20 % efficient devices may include graded bandgap absorbers, alternative buffer materials, different absorber doping levels, and additional back contact layers [47]. Studies already show that reaching a performance over 25 % efficiency is possible if carrier recombination at the CdTe interface with the contact layers is reduced [48].

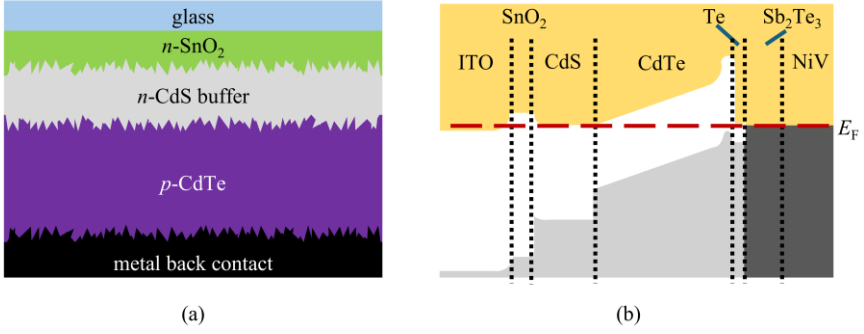


Fig. 15. (a) The layer structure and (b) band diagram of a typical CdTe solar cell. (adapted from [26])

Commercial thin-film CdTe solar cells use Cu-doped ZnTe (ZnTe:Cu) as the hole-selective back contact. However, ZnTe:Cu fails to passivate the back interface or form desired electron reflection to enhance performance [49]. Still, some teams have already identified several tetrahedrally bonded structures (TBSs) and their alloys (AlAs, AgAlTe<sub>2</sub>, ZnGeP<sub>2</sub>, ZnSiAs<sub>2</sub>, and CuAlTe<sub>2</sub>) that have promising properties required for back contacts in CdTe solar cells [50]. Moreover, group V dopants for CdTe and CdSe<sub>x</sub>Te<sub>1-x</sub> layers can improve back contact quality by achieving high hole densities and carrier lifetime with single crystal absorbers and reaching open-circuit voltage greater than  $V_{OC} > 1$  V [51, 52], and As doping in polycrystalline is now on par with Cu-based technology while degrading less, allowing efficiency of 22 % with  $-0.23$  %/°C temperature coefficient [53].

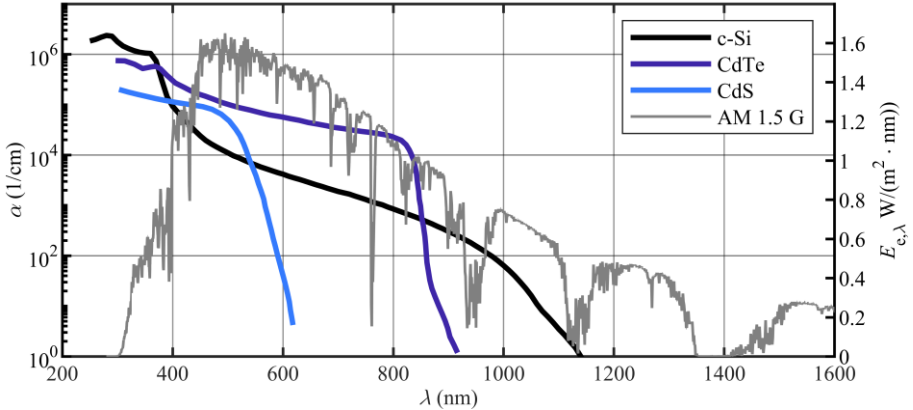


Fig. 16. Absorption spectra of CdTe and CdS in comparison with c-Si and AM1.5G reference spectrum. (data taken from [54])

Cd and Te are toxic, but the concern might be overstated as they are recovered as byproducts of base metal extraction like zinc and copper, and the quantity in PV modules is as low as 0.1 %, even compared to silicon solar

cells (3 – 4 % of Si) [55]. The leading manufacturer of CdTe cells “First Solar” claims that they guarantee recycling materials from end-of-life modules and decommissioned or rejected parts during manufacturing. Although they agree to the fact that a lot of care is needed to retrieve materials from the third-party markets [56].

Overall, the efficiency improvements and relatively low costs determined CdTe technology’s leading role in the thin-film solar cell market. While production seemingly stagnated until 2018, it has skyrocketed, already reaching 2 % of the global PV market share. Moreover, lead manufacturers are keen to reach over 20 GW annual production, which is comparable to the total power of installed modules.

### *Copper Indium Gallium Selenide (CIGS)*

Another perspective group for high-efficiency thin-film solar cells is chalcopyrites – materials based on chalcopyrite ( $\text{CuFeS}_2$ ), but generally consisting of elements from groups I, III, and IV. The I-III-IV semiconductors form tetragonal crystals, and various combinations can provide a wide range of lattice constants as well as band gaps [53] (Fig. 17), while having a direct band gap, hence, high absorbance compared to silicon.

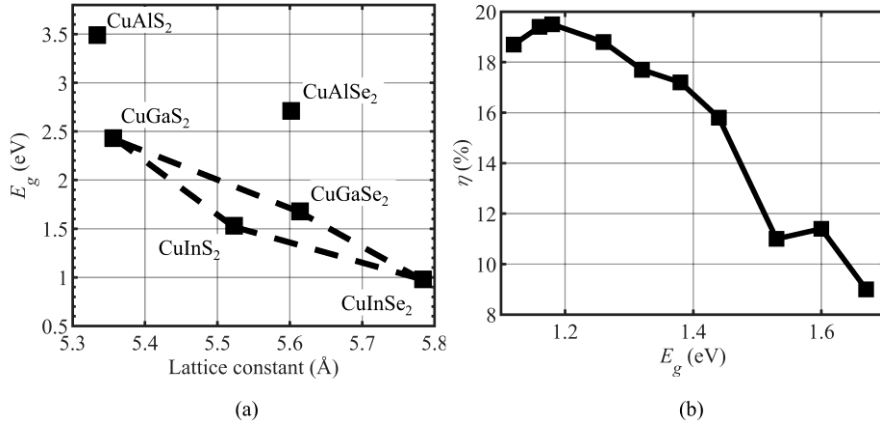


Fig. 17. (a) The band-gap versus the lattice constant for a selection of chalcopyrites (data taken from [57]), dashed lines indicate possible paths for band-gap tuning, (b) solar cell efficiency versus  $\text{Cu}(\text{In}_x\text{Ga}_{1-x})\text{Se}_2$  absorption layer band-gap value. (data taken from [58])

The most common chalcopyrite used for solar cells is a solid solution of copper, indium, or gallium and selenium or sulfur, resulting in a so-called CIGS(S) solar cell ( $[\text{Cu}(\text{In}_x\text{Ga}_{1-x})(\text{Se}_y\text{S}_{1-y})]$ ,  $x$  and  $y$  are numbers between 0 and 1). Different bandgap values can be achieved by tuning the proportions of indium and gallium concentration (Fig. 17(a)). Moreover, similar lattice



constants of these materials allow for better lattice-matching in tandem or band-gap-graded solar cells.

The absorber of a typical device utilizes  $p$ -type CIGS alloy, with low Ga content ( $x \approx 0.3$ ), resulting in an optimal (1.1 – 1.2) eV band-gap (Fig. 17(b)). However, wider band-gap absorbers are desired, and significant improvements are being made in this field [58]. The  $n$ -CdS layer acts as a wide band-gap buffer, although the defect density at the surface requires an additional  $n$ -type CIGS layer in between, creating a buried junction, where the carrier pairs are separated (Fig. 18).

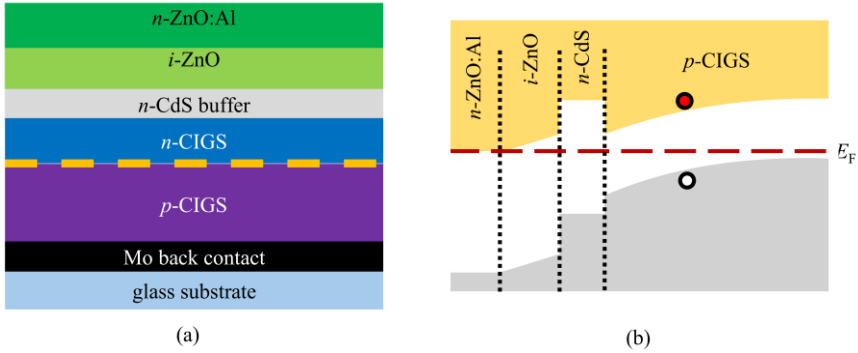


Fig. 18. Typical architecture of CIGS solar cell (dashed yellow line indicates a buried junction), and (b) its band diagram.

CIGS absorbers can be deposited (mostly by sputtering or co-evaporating) not only on soda-lime glass (SLG), but also on flexible substrates. Anyhow, low contamination of bulk absorber with sodium (Na) appears to reduce recombination in  $p$ -type CIGS, and, in amounts of about 0.1 % Na, the incorporation can lead to more than tenfold enhancement of all the parameters [59]. That is why SLG is more favorable as a substrate: it can provide the right amount of Na during film growth. SLG is also a low-cost, well-known material, fabricated on a large scale, and fulfils most of the demands for a proper CIGS substrate, like vacuum compatibility, thermal stability, chemical inertness, and more [60]. Potassium (K) is another alkali that has a similar influence on CIGS as Na, though their roles must be differentiated, especially after being supplied after the growth of the CIGS layer. Additional supplements of Na and K allow flexible devices grown on plastic, which can achieve 20.4 % efficiency, potentially even matching that of poly-Si wafer based devices [61].

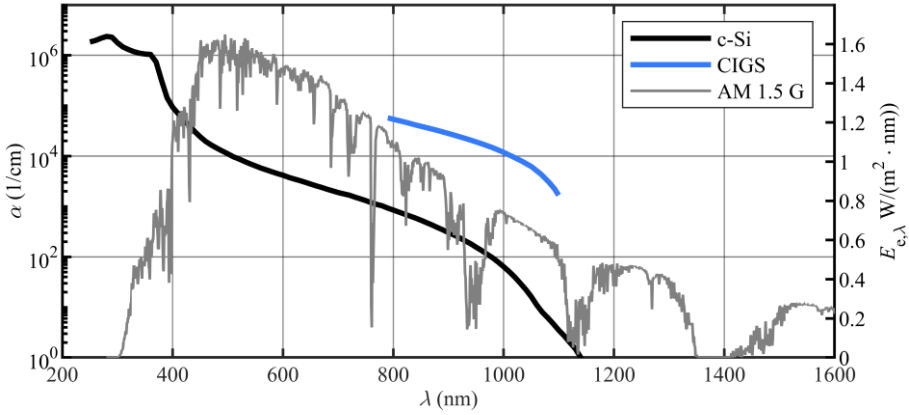


Fig. 19. Absorption spectrum of CIGS (data taken from [54]) in comparison with c-Si and AM1.5G reference spectrum.

As mentioned before, cadmium is toxic, hence, commercial production and sales of typical CIGS solar cells are quite difficult in some regions like the European Union or Japan. That is why Cd-free buffer layers are being investigated thoroughly. Many alternative materials, such as ZnS [62],  $\text{In}_2\text{S}_3$  [63],  $\text{Zn}_{1-x}\text{Sn}_x\text{O}_y$  [64], did not enable the devices to surpass those with CdS buffers. However, the present CIGS solar cell record holder is actually Cd-free [65]. This cell employs  $\text{Zn}(\text{O},\text{S},\text{OH})_x/\text{Zn}_{0.8}\text{Mg}_{0.2}\text{O}$  double buffer layers, deposited by a chemical bath deposition (CBD) and atomic layer deposition (ALD) technique combination which offers much larger band-gap energy ( $\sim 3.37$  eV) and more favorable energetic band alignment than CdS buffer, allowing more blue light to reach the absorber and suppressed recombination at the buffer/CIGS(S) interface respectively. That allowed the best thin-film solar cell technology result – 23.35 % efficiency on SLG. Nonetheless, CIGS is deposited in a complex process, so it is hard to manufacture it on a big scale. Moreover, indium is a rare earth metal also widely used to make transparent conductive oxides (TCO) employed in coatings for displays, other solar technologies or even aircraft windshields [66], making CIGS technology more expensive than CdTe. All these reasons mean that, while CdTe solar cells are being produced increasingly, CIGS technology never reached 2 GW global production and is even slowing down, dropping from  $> 2$  % of global market share in around 2012 to negligible levels nowadays.

## 1.2 Solar simulators

To use the photovoltaic devices effectively, their performance must be determined under real atmospheric conditions [67]. Carrying out such

measurements under natural sunlight in the outdoor environment is not preferable, because the result for the measured device can be significantly affected by various environmental conditions such as temperature, irradiance, or spectral effects, which in turn depend on varying atmospheric conditions, air mass, and albedo [68]. Instead, current-voltage ( $I$ - $V$ ) measurements are performed in a closed laboratory-like environment with the help of solar simulators, due to their simplicity, reproducibility, and reliability [69]. The characteristic values of PV devices, such as  $I$ - $V$  curve, open circuit voltage ( $V_{OC}$ ), short circuit current ( $I_{SC}$ ), and maximum power ( $P_{MAX}$ ), are evaluated, and devices are rated under the so-called Standard Test Conditions (STC). STC corresponds to an irradiance of  $1000 \text{ W/m}^2$ , a defined spectral distribution (such as AM1.5), and a device temperature of  $25^\circ\text{C}$  [70]. In general, solar simulators are calibrated tools that provide a spectrum and optical composition similar to sunlight, with the ability to change conditions on demand to illuminate a PV device or any other solar-irradiance-sensitive subject.

Solar simulators (sometimes called artificial sun) can also be applied in many non-PV cases. Studies on the photodegradation of aging plastics, like low-density polyethylene (LDPE), are being conducted by diverse teams on topics varying from greenhouse cover films in Spain [71] to trash polluting the ocean in South Korea [72]. Solar simulators allow accelerated and constant weathering conditions, resulting in estimation of long-term microplastics and nanoplastics secondary production and thus advanced decision-making on methods for removing plastic litter. Solar irradiation can also be useful for removing pollutants from the water and treating sewage water. A significant impact of osmotic and mechanical stress on the viability of *E. coli* bacteria induced by a solar simulator with a customized reflector was found by Karine *et al.* [73]. In parallel, concerns about the aging materials suitable for solar water disinfection (SODIS) containers are being addressed, simulating solar radiation matching, for example, with the annual dose received in Mekelle, Ethiopia [74].

Other solar simulator uses, with modified spectra or optics, include studies on such topics as sunscreen UVA efficacy [75], ecological research on plants [76] or algae [77], bleaching of reef-building corals [78] and high flux variants for concentrated solar thermal energy applications [79, 80]. Moreover, high-quality, full-spectrum artificial lighting in buildings is proven to be beneficial for the health, productivity, and safety of building occupants by improving vitamin D intake, color rendering, and overall irradiance [81].

The first solar simulators were conceived to simulate the space environment for testing Earth satellites and other spacecrafts. During the 1960s, the National Aeronautics and Space Administration (NASA) sponsored a series of research programs that developed the testing chamber named “Space Environment Test Chamber”.

In the beginning, *carbon arc lamps* (Fig. 20(a)) were selected as a primary light source because their spectral irradiance is closely compatible with AM0 [82], hence being a good choice for space-like simulations. Anyhow, instability during operation, short lifetime, and significant amounts of short-wavelength radiation propagating from the carbon arc [79] led to the hunt for other light sources, concurrently increasing the need for AM1.5-like light sources. While the carbon arc nearly matches the solar spectrum more than any other single light source, it seemed clear that operating difficulties more than overcame this advantage.

NASA-sponsored scientists' next step was to try to use *Mercury Xenon lamps*. This duo combines the UV spectrum of mercury vapor lamps and the IR spectrum of xenon lamps [83]. After testing out various high-intensity commercially available lamps, it was determined that using these enclosed lamps is far more advantageous and desirable for reasonably long operations. Lamp intensity is a linear function of input electrical power, and very uniform spectra from lamp to lamp, with no spectral shifts in the position of the lines with lamp aging, and a wide irradiance spectrum stand for great qualities for solar simulators [84]. However, spectral energy distribution changes within a relatively short lamp lifetime due to darkening of lamp envelope and increased arc spacing, as well as undesirable ozone generation and even unexpected lamp explosions during on-off cycles, eventually resulted in the replacement of this kind of lamp by *Xenon arc lamps* as the first light source option [85].

*Xenon arc lamps* (Fig. 20(b)) are widely used light sources for solar simulators, especially commercially available ones. [86, 87, 88, 89, 90]. Xenon arc lamps produce light by an electric arc passing through an ionized Xe gas in high pressurized (up to 40 bar) enclosures [85]. The generated spectral irradiance is stable, regarding power variations, which also provides a good continuum in the UV and visible wavelengths. Moreover, high-pressure short-arc xenon lamps provide a brighter point source, compared to many other source types, which is required to produce a collimated high-intensity light beam [91]. These lamps create strong emission lines in the 800 nm – 1200 nm wavelength region. However, this disadvantage can be solved by employing an appropriate glass filter or using the lamp in a pulsed regime. *Pulsed xenon arc lamps* can also illuminate large test areas with minimal test sample heating. Still, they are more costly, and the millisecond

duration order of the pulse is inapplicable in the measurements of photovoltaic structures with long response times. Overall, high power consumption, a short life cycle, a need for constant maintenance, complex and crammed optical systems needed, as well as security risks, while operating under high pressures, are the main drawbacks [82], driving a slow but determined shift away from this technology.

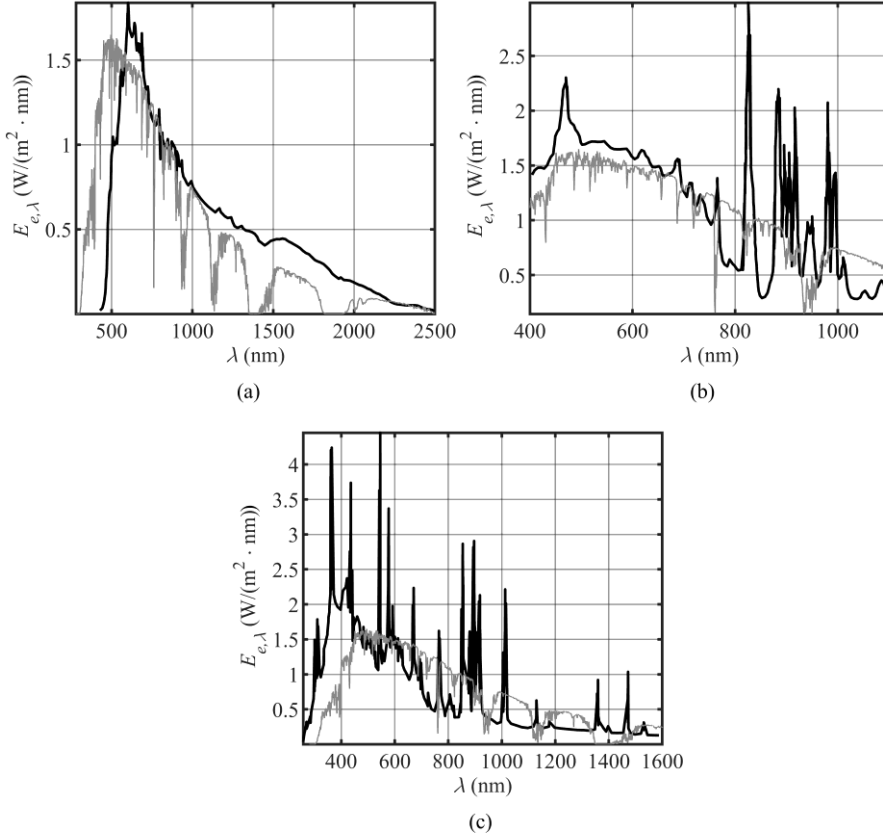


Fig. 20. The spectra of sample solar simulators utilizing: (a) carbon arc lamp [92], (b) Xenon arc lamp [93], (c) metal halide lamp [94].

*Metal halide lamps* (Fig. 20(c)) are gas-discharge lamps similar to mercury vapor lamps, but also filled with metal halide salts, and they operate at medium pressures (5 – 10 bar) [83]. These lamps, while unfiltered, emit close to black body radiation, but with a significant excess in UV and NIR regions compared to the Xenon arc lamp spectrum [94]. Metal halide lamps have high light efficacy, comparably long life-time, and, most importantly, they are relatively inexpensive, resulting in wide employment in industrial or outdoor stadium settings [95]. Nonetheless, by applying adequate filters over the reflectors or in the optical systems, metal halide lamps are utilized in low-cost,

high-flux solar simulators, mainly in concentrator setups [94, 95, 96, 97]. The main drawbacks of this technology are non-ideal spectrum, low collimation quality, and inconsistency in the spectral distribution from one lamp to another of the same type [98].

Other high-flux broad-spectrum light sources for solar simulators include *Argon arc lamps* (Fig. 21(a)) and *High-Pressure Sodium lamps* (HPS) (Fig. 21(b)). Argon arc lamp provides highly uniform and stable irradiation of 6500 K color temperature spectrum [99]. High-pressure (7 bar) argon arc is enclosed in a quartz envelope, which is internally cooled using a rapidly flowing swirling water film. In the configuration with elliptical mirrors, the lamp can achieve power flux intensities equivalent to 5000 suns [100]. High operating pressure, excessive radiation around 300 nm and 800 nm wavelengths, and complicated maintenance are named as the main drawbacks of argon arc lamps [1]. Meanwhile, HPS vapor lamps are efficient energy converters, offering excellent maintenance of light output and long lifetime [101]. Unfortunately, 2100 K color temperature of a standard HPS vapor lamp, with typical resonance lines (D-lines) at around 589 nm result in the most energy of spectral irradiance lying around the yellow region of the visible spectrum [102]. Moreover, these lamps can take a couple of minutes to stabilize, they are expensive, and require auxiliary electrical ballasts to regulate lamp power efficiently [103].

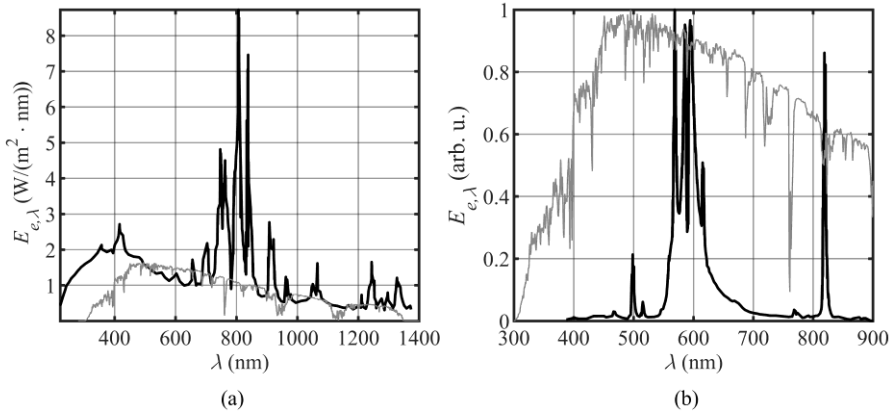


Fig. 21. The spectra of sample solar simulators utilizing: (a) argon arc lamp [100], (b) high-pressure sodium vapor lamp [104].

One of the most modern approaches to solar simulation exploits a *Supercontinuum Laser* (SL) (Fig. 22(a)). Supercontinuum generation occurs when narrow-band laser pulses are subjected to extreme nonlinear spectral broadening in glass, organic or inorganic liquids, gases, and various types of waveguides, most productively in photonic crystal fibers [105]. During the

last decades, high-power SLs that offer spectral coverage from 400 nm to > 2200 nm have become commercially available, allowing highly-focused simulator applications, utilizing the ability to shape the simulated spectrum arbitrarily [106]. The number of tunable zones of the spectrum for SL simulators is two orders of magnitude higher compared to other state-of-the-art technologies [103], allowing a virtually perfect imitation of standard solar spectra, eventually making any spectral mismatch correction redundant [107]. Solar cell degradation, wavelength-dependent characteristics, multi-junction concentrator PVs, and Light Beam Induced Currents (LBIC) are already being investigated, adopting the SL simulator. However, ultra-short pulses and very small illumination spots are the main areas in need of further research [108], [109, 110, 111].

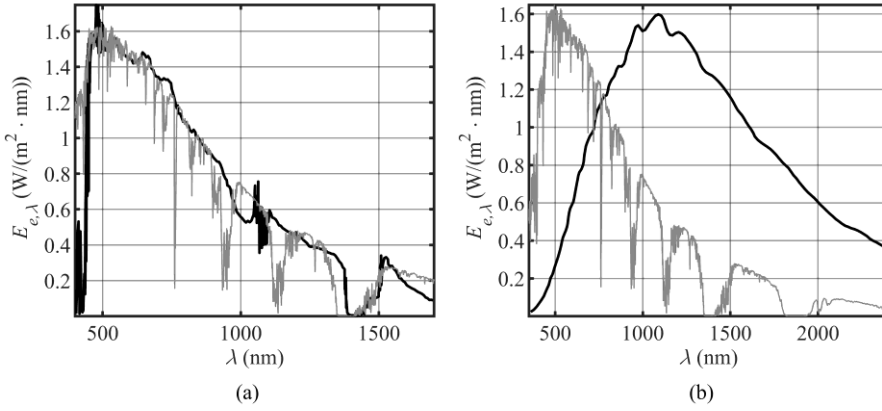


Fig. 22. The spectra of sample solar simulators utilizing: (a) supercontinuum laser [106], (b) quartz-tungsten lamp [112].

The eruption of PV technologies during the last decades means that solar simulators must meet more rigorous requirements for accuracy and reproducibility of measurements. The lack of stability, control, or overall spectral irradiance in the IR region for most of the broad-spectrum light sources led to the exploration of multi-light approaches, where, for example, UV irradiation can be mainly produced by a Xenon arc lamp, and the IR part is enhanced by a *Quartz Tungsten Halogen lamp* [112, 113] (Fig. 22(b)). Investigation of halogen lamp solar simulators themselves started in 1960s [114], however low color temperature (up to only ~3500 K) restricted them to mostly to low spectrum sensitive applications like in concentrated solar collectors [115], other heat related experiments [116] or, by employing some filters, as an affordable solar simulator for testing PV devices in the prototype [117]. Nowadays, Tungsten Halogen lamps are widely used in multi-source

solar simulators as a high-power, low-cost, low-maintenance, and consistent IR emitter [3, 80, 118, 119].

### 1.3 LED-based solar simulators

Around 2000, Light Emitting Diode (LED) technology made a huge development leap, advancing LED applications from a power-on indicator to the mainstream light source [120]. The main advantages of LEDs compared to other light sources are long lifetime (up to 25,000 hours [121], compared to up to 2000 hours for Xe arc lamps [122]), fast response and stabilization, defined colors, physical robustness, lack of toxic materials (e.g., mercury), and greater safety (lower temperature and absence of pressurized chambers) [120]. In accordance with rapid cost reduction, energy efficiency improvement, and output power, these properties were exercised in the first LED-based solar simulators, producing viable measurement concepts and procedures as early as 2003 [123]. The fundamental challenges, most of which are still accompanying this technology, have also been established: lack of spatial uniformity, shortfall in light intensity, spectral discreteness, and possible temporal instabilities due to temperature-induced effects.

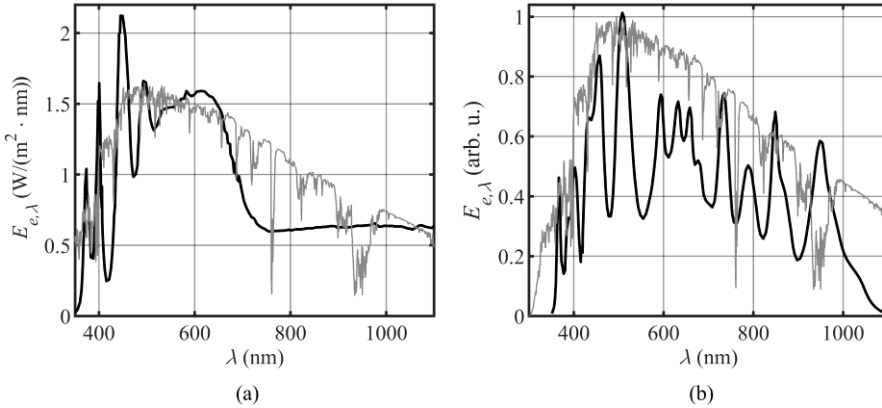


Fig. 23. The spectra of LED-based solar simulators proposed by (a) Bliss *et al.* [2] (2009) and (b) Kolberg *et al.* (2011) [124].

Nevertheless, Bliss *et al.* demonstrated a standalone LED-based solar simulator, achieving more than one Sun intensity and BAA-class (see Table 2, p. 39) over an area of  $(60 \times 60) \text{ mm}^2$  [2] (Fig. 23(a)). This simulator consisted of several hundred LEDs of 8 assorted colors and covered the light spectrum from 375 nm to 680 nm, in conjunction with halogen lights to cover the IR part of the spectrum. Notably, high-power infrared LEDs have



only gained traction in the early 2010s [125], and they are still a hot research topic nowadays [126, 127].

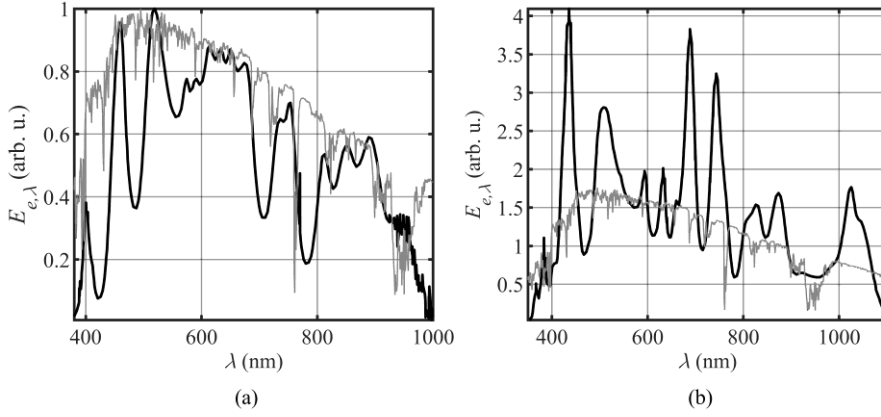


Fig. 24. The spectra of LED-based solar simulators proposed by (a) Hamadani et al. (2012) [128] and (b) Linden et al. (2014) [129].

Lots of distinct designs have been proposed during the last decade. Kolberg et al. proposed a setup with 23 distinct color LEDs that produces a close-matched spectrum to AM1.5 or virtually any other spectrum of interest [124] (Fig 23(b)). Hamadani et al. proposed using 5 m long tapered light guides on LED matrices consisting of 34 high-power LEDs of different wavelengths to promote better mixing of the light rays over a large testing area [128] (Fig. 24(a)). During the last decade, white LEDs, consisting of blue LED and yellow phosphor ( $\text{Y}_{3-x}\text{Gd}_x\text{Al}_{5-y}\text{Ga}_y\text{O}_{12}:\text{Ce}^{3+}$ , YAG:Ce), has become more popular [130], as they are beneficial to broad high-brightness coverage of the visible spectrum from virtually one point, resulting in high illumination uniformity and good spectral characteristics in simulators using six different LEDs without addressing the IR part by Bazzi et al. [131] and a 23-LED full-spectrum AAA-class simulator by Linden et al. [129] (Fig. 24(b)).

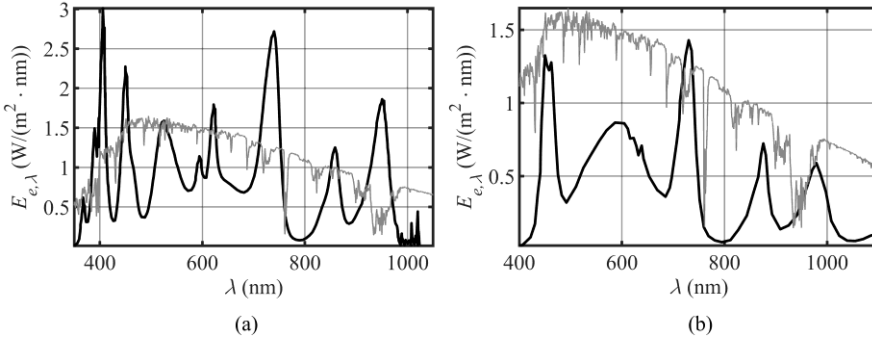


Fig. 25. The spectra of LED-based solar simulators proposed by (a) López-Fraguas et al. (2019) [132] and (b) Esen et al. (2022) [133].

Nowadays, LED-based solar simulators are widely commercially available; their stability, uniformity, and spectral match align with the highest PV industry standards, thus already giving them equal standing with other traditional solar simulators [134, 135, 136, 137]. However, a demand for low-cost or large scale simulators [132, 133, 138], as well as rising standards, especially in spectral coverage and spectral deviation context, bring out novel challenges and research topics in LED-based solar simulator field.

#### 1.4 Standards for solar simulators

For a light source to be classified as a solar simulator, it must be evaluated according to one of three major standards:

- IEC 60904-9 Edition 3 (2020) Photovoltaic Devices – Part 9: Classification of solar simulator characteristics [4];
- JIS C 8904-9 (2017), Part 9: Solar Simulator Performance Requirements (based on IEC 60904-9 Ed. 2 (2007) [139]);
- ASTM E 927-19 (2019) Standard Specification for Solar Simulation for Electrical Performance Testing of Photovoltaic Devices [140].

These standards provide the definitions of and means for determining simulator classifications used to characterize photovoltaic (PV) devices during indoor measurements. In this work, the IEC 60904-9 Edition 3 (2020) [4] standard will be referenced almost exclusively, with the exception of the context of the first simulator prototypes, because they were built before the release of the latest revision.

The novelty of the standard update led to a transitional period during which both current and earlier versions were referenced in recent publications, including studies presenting extensions that are not strictly required under a previous version. For example, an AAA-class solar simulator and an extension of the spectrum into the UV region were demonstrated in [135], but an older version of the standard was referenced.

Solar simulators are classified as A+, A, B, or C based on criteria of: Spectral Distribution match, irradiance Non-Uniformity in the measurement plane, and Temporal Instability of irradiance (see Table 2). All three criteria should be shown in a three-letter combination, one for each (e.g., BAA-class means: B-class for spectral distribution match, A-class for spatial uniformity, and A-class for temporal stability). In case a solar simulator does not meet the minimum requirements of class C, it cannot be classified according to the standard.

Table 2. Definition of solar simulator classifications [4].

	Maximal Spectral Irradiance Deviation ( <i>SID</i> )	Spatial Non-Uniformity ( <i>NU</i> )	Temporal Instability of irradiance	
			Short Term ( <i>STI</i> )	Long Term ( <i>LTI</i> )
A+	0,875 – 1,125	1 %	0,25 %	1 %
A	0,75 – 1,25	2 %	0,5 %	2 %
B	0,6 – 1,4	5 %	2 %	5 %
C	0,4 – 2,0	10 %	10 %	10 %

In the latest edition, several significant technical changes were included:

- Spectral match classification in an extended wavelength range was added (from 400 nm – 1100 nm to 300 nm – 1200 nm);
- A new A+ class was introduced;
- Additional parameters for spectral irradiance evaluation were defined: Spectral Mismatch (*SMM*), Spectral Coverage (*SPC*), and Spectral Deviation (*SPD*)

All of these parameters will be described more extensively in the following chapters. It should also be noted that class A+ is only defined if spectral match evaluation is performed in the extended (300 nm – 1200 nm) wavelength range.

#### 1.4.1 Spectral match

The spectral match of solar simulators is evaluated by calculating the largest relative deviation  $d_i$  of spectral irradiance in six spectral intervals:

$$d_i = \frac{\int_{\lambda_{1,i}}^{\lambda_{2,i}} E_{e,\lambda,\text{SIM}}(\lambda) - E_{e,i,\text{AM1.5G}}}{E_{e,i,\text{AM1.5G}}}, \quad (1)$$

where  $d_i$  is the relative deviation in  $i$ -th wavelength interval,  $E_{e,\lambda,\text{SIM}}(\lambda)$  – spectral irradiance of the solar simulator,  $\lambda$  – wavelength,  $E_{e,i,\text{AM1.5}}$  – required irradiance in the  $i$ -th wavelength interval under AM1.5G conditions ( $i = 1, \dots, 6$ ),  $\lambda_{1,i}$  and  $\lambda_{2,i}$  – the minimum and maximum wavelengths of these ranges, respectively.  $|d_i| \leq 12.5 \%$  should be ensured for the highest A+ classification. These deviations can be larger in cases of lower classification. For example,  $|d_i| \leq 25 \%$  is allowed in the case of A-class. In this work, maximal relative Spectral Irradiance Deviation throughout all spectral intervals, which defines the simulator class, will be shortened to *SID*. The wavelength ranges and irradiance share for each range are presented in Table 3.

Table 3. Global reference solar spectral irradiance distribution provided in “old” and latest IEC standard.

Interval	1 <sup>st</sup>	2 <sup>nd</sup>	3 <sup>rd</sup>	4 <sup>th</sup>	5 <sup>th</sup>	6 <sup>th</sup>
IEC 60904-9 Edition 2 (2007)						
Wavelength range (nm)	400 – 500	500 – 600	600 – 700	700 – 800	800 – 900	900 – 1100
Share of total irradiance	18,4 %	19,9 %	18,4 %	14,9 %	12,5 %	15,9 %
IEC 60904-9 Edition 3 (2020)						
Wavelength range (nm)	300 – 470	470 – 561	561 – 657	657 – 772	772 – 919	919 – 1200
Share of total irradiance	16,61 %	16,74 %	16,67 %	16,63 %	16,66 %	16,69 %

The class for the spectral match of the solar simulator is given according to Table 2.

#### 1.4.2 Spatial Non-Uniformity (*NU*)

The light received from the sun is of uniform intensity and spectral composition on a flat plane, so a solar simulator should also produce uniform irradiation. Usually, some homogenizing optics are used to realize such circumstances. The non-uniformity of irradiance may increase the uncertainty for maximum power determination of PV devices, which is why the test chamber or test apparatus should be considered an integral part of the simulator – its description and technical drawings should be included in the classification report.

For PV cell solar simulators, the measurements should start at the corner of the designated test area, and the step width for moving the irradiance detector should not exceed 1/5 of the smallest dimension of the test plane. Using these measurements, spatial non-uniformity is determined using:

$$NU = \left( \frac{\max_{irr.(A)} - \min_{irr.(A)}}{\max_{irr.(A)} + \min_{irr.(A)}} \right) \times 100\%, \quad (2)$$

where  $\max_{irr.(A)}$  and  $\min_{irr.(A)}$  are the maximum and the minimum irradiance values area-wise, respectively.

The class for the spatial non-uniformity of the solar simulator is given according to Table 2.

#### 1.4.3 Temporal Instability

Temporal instability represents changes in solar simulator irradiation over time. A high temporal instability might lead to unrepeatable and apparently

noisy measurement results. Temporal instability can result from hardware-related factors of the simulator, such as arc flutter in discharge lamps, noise in power supplies, or irradiance change caused by inefficient cooling. There can also be distinct types of instability, such as flickering over a short time ( $< 1$  s) or as irradiance drift over a more extended time (hours, days, ...). That is why short-term instability (*STI*), and long-term instability (*LTI*) need to be evaluated and reported. Temporal instability (*TI*) is calculated using:

$$TI = \left( \frac{\max_{irr.(t)} - \min_{irr.(t)}}{\max_{irr.(t)} + \min_{irr.(t)}} \right) \times 100\%, \quad (3)$$

where  $\max_{irr.(t)}$  and  $\min_{irr.(t)}$  are the maximum and the minimum irradiance values, time-wise, respectively.

The class for the temporal instability of the solar simulator is given according to Table 2.

#### 1.4.4 Spectral Coverage (*SPC*) and Spectral Deviation (*SPD*)

Spectral Coverage and Spectral Deviation from the AM1.5G spectrum are two new values introduced in [4]. They are not yet to be reported, but they can indicate how well the spectrum of the solar simulator matches the reference one. These kinds of parameters are being called for in spite of new solar simulator technologies, especially LED-based technologies, where the three main criteria could be satisfied, but because of the quasi-discrete nature of the simulator spectrum, the  $j$ - $V$  characteristics would be incorrect.

Spectral coverage (*SPC*) measures how much of the reference spectrum is represented in the simulator spectral irradiance. It shows how much of the spectral irradiance from the simulator is at least at 10 % of the irradiance of the reference spectrum at each wavelength step in the 300 nm – 1200 nm wavelength range and can be determined by:

$$SPC = \left( \sum_{E_{sim}(\lambda) > 0.1 \cdot E_{AM1.5}(\lambda)} E_{AM1.5}(\lambda) \cdot \Delta\lambda / \sum_{300 \text{ nm}}^{1200 \text{ nm}} E_{AM1.5}(\lambda) \cdot \Delta\lambda \right) \cdot 100\%, \quad (4)$$

where  $E_{sim}(\lambda)$  is the spectral irradiance of the solar simulator;  $\lambda$  is the wavelength; the standard wavelength step, also used throughout this work,  $\Delta\lambda = 1$  nm;  $E_{AM1.5}(\lambda)$  is the required spectral irradiance under AM1.5G conditions. A 100 % *SPC* means that the entire spectral range of the simulator has at least 10 % of the reference spectrum, while small values indicate the gaps in the simulated spectrum.

Spectral deviation (*SPD*) shows how closely the spectrum of the solar simulator follows the shape of the reference spectrum in the 300 nm – 1200 nm wavelength range and is calculated using:

$$SPD = \sum_{300 \text{ nm}}^{1200 \text{ nm}} |E_{sim}(\lambda) - E_{AM1.5}(\lambda)| \cdot \Delta\lambda \bigg/ \sum_{300 \text{ nm}}^{1200 \text{ nm}} E_{AM1.5}(\lambda) \cdot \Delta\lambda \cdot 100\%. \quad (5)$$

The value of  $SPD = 0 \%$  indicates a perfect match between the simulator and the reference.

#### 1.4.5 Spectral Mismatch (*SMM*)

Despite strict standards about the classification of solar simulators, efficiency measurements of the same cell on different systems can appear quite different, because (a) not all solar simulators provide the same spectral irradiance, and (b) not all solar cells have the same wavelength response. That is why it can be challenging to compare efficiency results between different solar cell technologies, or even the same PV technology irradiated by different solar simulators.

A spectral mismatch (*SMM*) parameter has already been introduced in the early days of the PV technology ([141, 142]) as a means of correcting any  $j$ - $V$  measurements and resulting device metrics in case of the simulator spectrum being different from the reference one (e.g., AM1.5G).

The short-circuit current  $I_{SC}$  is equal to the integral of spectral irradiance multiplied by the spectral response of the PV element, over the wavelength interval of interest:

$$I_{SC} = \frac{1}{D} \int_{\lambda_1}^{\lambda_2} E(\lambda) S(\lambda) d\lambda, \quad (6)$$

where  $D$  – the area under irradiance,  $E(\lambda)$  – spectral irradiance and  $S(\lambda)$  – spectral response.

If we assign four different short circuit currents relating to the reference/test solar cell ( $I^{ref}/I^{test}$ ) under reference/simulator irradiance ( $I_{AM1.5G}/I_{sim}$ ), we get the definition of the spectral mismatch parameter:

$$\frac{I_{sim}^{test}}{I_{sim}^{ref}} = SMM \frac{I_{AM1.5G}^{test}}{I_{AM1.5G}^{ref}}. \quad (7)$$

The area terms cancel out so long as the solar simulator of interest provides uniform illumination on both PV elements. After rearranging, we get an equation for spectral mismatch calculation (Eq. 8).

$$SMM_{ij} = \frac{\int E_{ref}(\lambda) \cdot S_i(\lambda) \cdot d\lambda \int E_{sim}(\lambda) \cdot S_j(\lambda) \cdot d\lambda}{\int E_{sim}(\lambda) \cdot S_i(\lambda) \cdot d\lambda \int E_{ref}(\lambda) \cdot S_j(\lambda) \cdot d\lambda} (i < j), \quad (8)$$

where  $S_i(\lambda)$  and  $S_j(\lambda)$  are spectral responsivities of devices number  $i$  and  $j$ , respectively;  $E_{ref}$  and  $E_{sim}$  are spectral irradiance of a reference source and solar simulator, respectively.

There are two practical cases for which the standard [4] provides the procedures: (a) for known, “real-world” spectral responsivities and (b) when the variation of spectral responsivities is not known.

Estimation of the impact of spectral irradiance on measurement uncertainty when the variation of spectral responsivity is known is based on the statistical analysis of the  $SMM$  factors for multiple PV devices (at least four) of the same technology, where using the Eq. (8)  $SMM$  is calculated for each pair of devices or after defining a reference  $SR$  curve from the set – pairs with the reference one. Then, the sensitivity to the spectral mismatch effects ( $uSMM$ ), which corresponds to the standard deviation, should be reported:

$$u(SMM) = \frac{1}{\mu} \cdot \sqrt{\frac{1}{m} \sum_{1 \leq i < j \leq n} (SMM_{ij} - \mu)^2}, \quad (9)$$

where  $n$  – the number of spectral responsivity data series,  $m = \frac{n^2 - n}{2}$  and  $\mu = \frac{1}{m} \sum_{1 \leq i < j \leq n} SMM_{ij}$ .

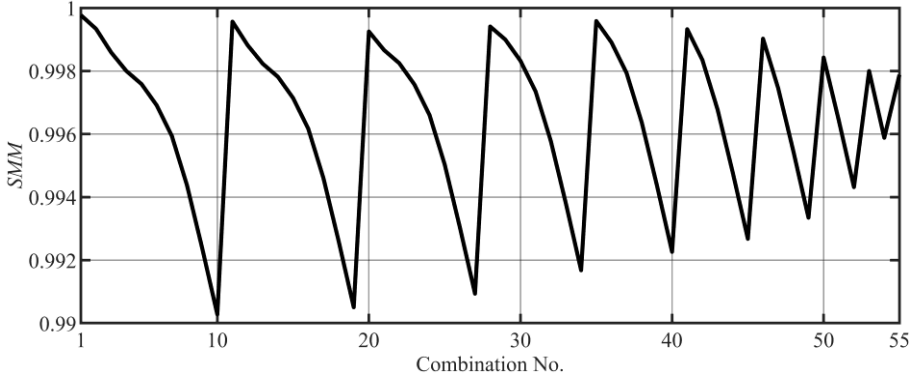


*Fig. 26. An example of spectral mismatch parameter for one of the simulators illuminating each pair of 11 simulated Al-BSF solar cells with varying doping concentration.*

Although sensitivity is the only parameter needed to specify solar simulators,  $SMM$  can also give some insights, especially when  $EQE$  is being gradually changed by varying one solar cell parameter. Fig. 26 visualizes an example of calculated spectral mismatches for one of the simulator spectra

used in this work, illuminating 11 simulated Al-BSF c-Si solar cells with various (and growing) base doping concentrations.

In this work, spectral mismatch comparison will be made with reference *SR* curves defined as the center ones from the set (with the standard parameter value for a given device), which basically coincide with the first branch of complete comparison (Fig. 26, combinations 1 – 10). Moreover, *SMM* – 1 will be plotted to conform better with other visuals, and the first comparison will be made for the reference curve with itself, fixing the middle point at 0 and representing the total number of different devices used better.

In case the spectral responsivity dispersions are not known, or less than four spectral responsivity data sets are available, virtual spectral responses and dispersions can be modeled to evaluate the sensitivity to spectral mismatch error.

A virtual spectral responsivity can be modelled with the four parameters defining the points where it drifts away from spectral responsivity of an ideal photodiode ( $a_2$ ,  $b_1$ ) and the points where the spectral responsivity of the device is above zero ( $a_1$ ,  $b_2$ ) (see Fig. 27, black solid line). The dispersions are modelled by two parameters:

- $x$  – the dispersion unit (nm) of the *SR* around the data points  $a_2$  and  $b_1$ ;
- $k$  – the integer multiplier of the dispersion unit.

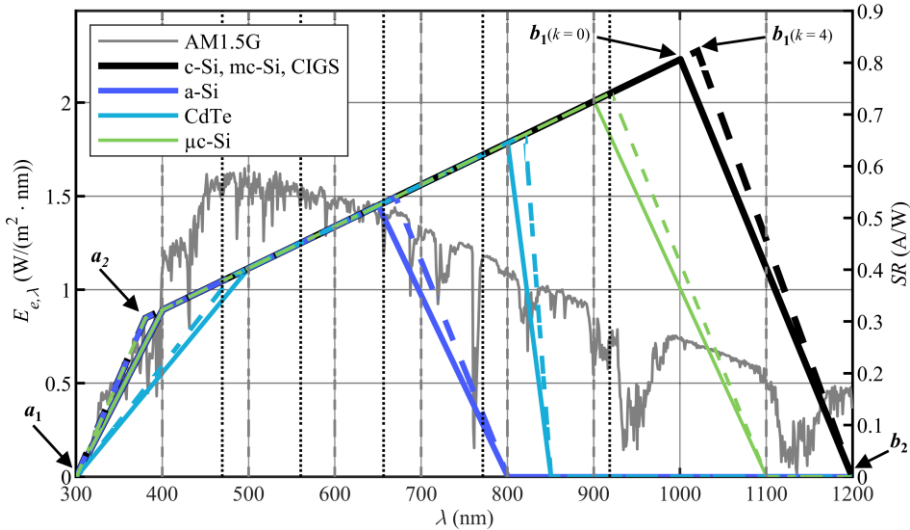


Fig. 27. AM1.5G reference spectrum (vertical grey dashed lines indicate the spectral ranges used for the integration of spectral irradiance in “old” standard [139], dotted lines – “new” standard [4]) and virtual spectral responses of different solar cell technologies. Dashed colored lines show dispersion by  $x = 5$  nm for  $k = 4$ .



The latest IEC standard provides the parameters of the reference spectral responsivity for six different solar cell technologies (c-Si, a-Si, CdTe,  $\mu$ c-Si, multi-c-Si, and CIGS), although the parameters are the same for some of them; that is why effectively four different technologies will be used in this study.

After choosing a reference curve for a desired technology, a minimum of  $k = 4$  dispersion *SR* curves are to be modeled by applying the dispersion parameter  $x$ , effectively compiling five distinct PV devices with slightly different spectral responsivities and *EQE*. A standard default is  $x = 5$  nm, but it can be adjusted to the actual needs (see Fig. 27, black dashed line):

$$a_{2-kx} = a_2 - k \cdot x, \quad (10)$$

$$b_{1+kx} = b_1 + k \cdot x. \quad (11)$$

The two parameters  $a_1$  and  $b_2$  remain fixed. The robustness of a solar simulator should be represented by spectral mismatch errors ( $SMM(k) - 1$ ) as a function of the dispersion. The slope of the regression line indicates the robustness of spectral irradiance.

## 2 METHODS

### 2.1 LEDs, Reflectors, and Data Sources for Simulations

Fifteen spectra of light sources in total were considered during this study. The particular subset of four to eight sources for each simulator configuration is the result of the optimization procedure. The first six light sources have already been used in AAA class solar simulators [3]. Four additional LEDs of different wavelengths were selected in the original 400 nm – 1100 nm range for the finer control of available spectra. These wavelengths were chosen because of the availability of high-power LED devices from multiple manufacturers for lighting, signaling, horticulture, industrial automation, or safety and security applications. Four additional ultraviolet (UV) LED emitters were selected to extend the spectrum to the UV range again, based on the general availability of high-power devices. The spectrum of the Bentham CL2-calibrated emitter (Bentham Instruments Limited, Reading, UK) serves as a spectrum example of a halogen lamp source. A full list of all light sources considered can be found in the appendix A2. To be effectively used in solar simulators, light sources should possess the following key properties: proven effectiveness in other industries; the highest possible power output; and, in the case of narrow-spectrum LEDs, a peak wavelength centered within the target spectral interval to minimize interference with adjacent intervals during power adjustments. Additionally, the light source should be readily available on the market.

Ray data for ray tracing for LZ4 emitters was provided by the manufacturer [143]; other types of data had to be incorporated when designing mixed arrays with and without individual reflectors. The manufacturer provided the dependence of the relative intensity on the angular displacement for BXRA-56C9000-J arrays [144]. However, experimental distributions were used for further modeling to avoid any issues due to the larger emitting area size compared to other LEDs. Photometric data in IES [145] and EULUMDAT [146] file formats were available for used LEDiL “Britney-M” and “Boomerang” reflectors.

### 2.2 Measurement system

Irradiance distribution and spectra were measured by an Avantes AvaSpec 2048 spectrometer with an SMA fiber patch cord and a Thorlabs CCSA2 cosine corrector attached in a rigid light construction with a Thorlabs SM1 tube segment. Computer-controlled stage Standa 8MT195 and

8MT295 stages were used for positioning purposes. Bentham CL2 spectral irradiance standard lamp was installed and used on the same optical table to calibrate the spectrometer without fiber patch cord disconnection. Besides, a BPW 34 B silicon photodiode with a Thorlabs PM100D power meter and a calibrated Thorlabs FDS-1010-CAL silicon photodiode with a digital multimeter were used for irradiance  $NU$  (both equipment) and temporal instability (first equipment) assessment. The responsivity spectrum of the FDS-1010-CAL photodetector is presented in Fig. 28.

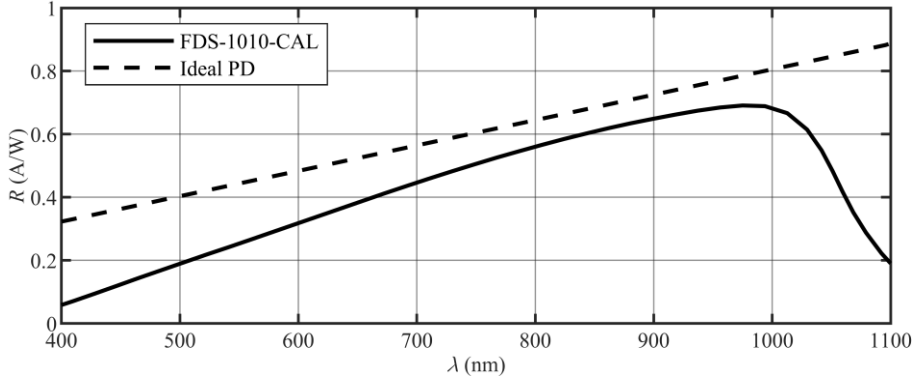


Fig. 28. Responsivity spectrum of an ideal photodiode without current gain (dashed line) and FDS-1010-CAL photodiode [P1] (used for measurements within the wavelength interval defined in the older standard edition).

Multiple spectrum measurement options are envisaged in the [4] standard: monochromators with discrete detectors; spectrometers, based on charge-coupled devices (CCDs), complementary metal oxide semiconductors (CMOSs), or photodiode arrays; multiple detector assemblies with band pass filters; and single detectors with multiple band pass filters. Each of these specific techniques requires separate and complex evaluations of uncertainties for multiple spectral ranges.

### 2.3 Distribution simulation

Custom ray-tracing software was developed in the MATLAB environment to combine algorithms of ray-tracing with processing of experimental, IES (Illuminating Engineering Society), and EULUMDAT (EU luminaire data) data. It is used specifically to simulate the propagation of rays from luminaires with an external reflector of a rectangular parallelepiped shape. The target for useful irradiation area under a simulator, thus the initial length and width of the external reflector, was chosen to be 16 cm  $\times$  16 cm. At the time, a popular wafer size of a cell was M0 (15.6 cm  $\times$  15.6 cm), moreover, half cells

(15.6 cm  $\times$  7.8 cm) were becoming standard, so as to avoid increases in resistive power losses due to higher currents from larger cells [147]. While considering the arrangement of the light sources in the simulator, their symmetries around the center point and the normals of the mirror planes were deduced to be the main conditions to achieve a favorable color mix at the measurement plane. First, an expected intensity distribution was generated without considering the influence of side mirrors and their reflection coefficient. After this step, either experimentally measured irradiance distributions, or calculated by other means irradiance distributions can be added. Afterward, these distributions are “folded” (Fig. 29) with relevant weight coefficients dependent on the number of reflections to obtain the final irradiance distribution with the reflector box. These weight coefficients  $R^N$  are defined based on the number of reflections  $N$  for each square and the mirror reflection coefficient  $R$  (Fig. 30).

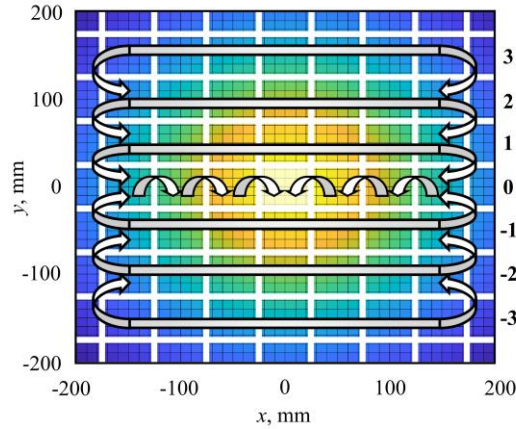


*Fig. 29. Illustration of calculation algorithm with “folding” and adding relevant distributions in the case of square reflector systems [P1].*

This approach allowed for an efficient combination of ray-tracing results, measurement data for LEDs and calculated distributions from manufacturer supplied EULUMDAT or IES files. Such full controls over the algorithm, full modification capabilities, precision and relative ease of software implementation were the primary reasons why, for at least the bulk of preliminary simulations, custom development was selected over other ray-tracing software.

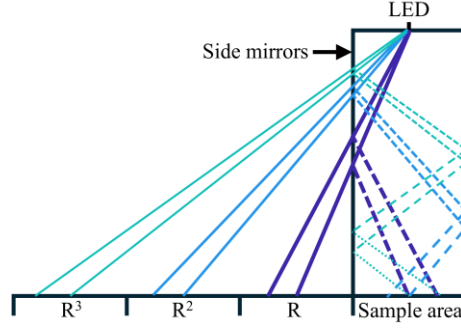


Fig. 30. Illustration of calculation algorithm with ray tracing [P1].

Intricate details related to imperfections of the mirror system were simulated using POV-Ray ray-tracing software. It enabled additional flexibility when simulating variable distances between mirrors or gaps between the mirror system and the measurement plane. However, simulations using reflective surfaces for mirror box showed deviations of irradiance values compared to simulations using our custom-made programs as well as experimental data. Therefore, we used both options depending on the aim.

## 2.4 Generating the spectra

After obtaining an irradiance distribution at the measurement plane, relative irradiance of each light source at any point has been augmented with spectral components from manufacturer supplied or experimental data, usually spanning 300 nm – 1200 nm wavelength range every 1 nm. After factoring and adding all relevant light sources at any given point, full spectral irradiance can be obtained. In most cases of spectral mismatch calculations throughout this work, only one point space-wise has been considered, because it was shown that, at least in our setups, the spectral deviation between different points of measurement plane is minimal, and at the same time that puts more emphasis on the spectral investigation.

Additionally, to produce a spectrum with perfect spectral match (interval-wise), we used the *fmincon* solver from the Matlab Optimization Toolbox [148] for finding minima of constrained nonlinear multivariable functions:

$$[E_e, d_{\max}] = fmincon(f(E_e), E_{e0}, [ \quad ], [ \quad ], [ \quad ], [ \quad ], b_l, b_u, nml(E_e)), \quad (12)$$

where  $E_e$  is a vector of  $N$  irradiance values from  $N$  light sources used for the optimization. This solver also requires the initial values  $E_{e0}$  to be supplied. We used equally distributed irradiance between all sources as a starting condition. The scalar value  $d_{\max} = f(E_e)$  is returned when the value of the

so-called objective function  $f(E_e)$  is minimized. Since our first goal is to find the minimum  $d_i$  for each possible combination of  $N$  sources, the objective function for any particular combination becomes:

$$f(E_e) = \max_i(|d_i|). \quad (13)$$

Pairs of empty square brackets in Eq. (12) indicate omitted *fmincon* parameters. Vectors of lower  $b_l$  and upper  $b_u$  bounds of  $E_e$  values are used for enforcing the required power limits: setting all elements of  $b_l$  to zero prevents negative optical power contributions from individual light sources, while each  $b_u$  element can be set as equal to the total AM1.5G irradiance, preventing any unnecessary restrictions to the algorithm. Optimization problem constraints, such as a requirement to exactly match AM1.5G total irradiance in the 300 nm – 1200 nm wavelength range, are described in  $nlc(E_e)$  function.

Some examples of custom made MATLAB scripts can be found in appendix A3.

## 2.5 Solar cell simulation

Currently, a wide variety of solar cell technologies and materials exists. While mass production costs steadily decrease yearly, expensive laboratory equipment and facilities are often required to fabricate and characterize innovative designs [149]. Computer-aided simulations can help designers understand how a PV device will perform prior to actual fabrication by employing a wide range of mathematical tools based on models that agree with experiments. A reliable and efficient analysis capability, providing realistic solutions of the semiconductor equations, was demonstrated as early as 1975 [150]. The development of personal computers paved way for routine solar cell simulation even in small laboratory setups, utilizing a broad range of simulation tools available today.

Throughout this work, two solar cell simulation tools were used: “Synopsys TCAD” and a non-commercial “PC3D”.

### TCAD

“Synopsys TCAD Sentaurus™” project is a 3D optical simulation software focused on monocrystalline silicon solar cells with textured surfaces, using the Monte Carlo raytracing method [151]. It is a well-established and trusted solution for thousands of users from diverse fields in the semiconductor industry [152].

TCAD introduces a physical model interface linking 3D optical simulations to electrical analysis via two simulation steps [153]. The optical

simulation stage allows users to generate periodic structures, such as pyramid textures, encapsulation materials, glass covers, contact definitions, and, of course, bulk material with a variable doping profile. Then, by performing ray-tracing for the wavelength list provided by the spectrum file, the software simulates the optics of the generated structure and calculates the transmittance, absorbance, total absorbance, and absorbance spectrum, as well as spectral generation, while granting users control of various boundary conditions. The second stage simulates the illuminated  $I$ - $V$  or  $EQE$  curves and extracts PV parameters, like short-circuit current ( $j_{sc}$ ), open-circuit voltage ( $V_{oc}$ ), photogenerated current ( $j_{ph}$ ), efficiency ( $\eta$ ), and fill factor ( $FF$ ). During electrical simulation, the user can control the free carrier absorption and front surface recombination velocity, select the Auger model, trap specification, and Shockley-Read-Hall recombination parameters, or even choose the bandgap narrowing model.

The Synopsys TCAD software package was used to simulate the performance of typical silicon solar cells under the illumination of multiple generated spectra. For this purpose, we used the built-in model of aluminum back surface field (Al-BSF) solar cell example for three-dimensional ray-tracing with pyramid texturing, a 180  $\mu\text{m}$  thick substrate, enabled free carrier absorption, 200  $\mu\text{m}$  thick ethylene vinyl acetate (EVA) encapsulation, and a 1 mm thick glass layer. We only varied the illumination spectrum during our simulations. Also, for AM1.5G reference simulations, we replaced the reference AM1.5G solar spectrum, built-in within Synopsys TCAD, with a higher resolution one published by the National Renewable Energy Laboratory [154].

### PC3D

PC3D is a very accurate non-commercial tool initially developed in 2019 in an effort to combine its widely acclaimed predecessors PC1D and PC2D. Its user interface is provided by Microsoft Excel (Fig. 31), but all calculations are performed in code for faster solutions. PC3D implements a conductive boundary model with a uniformly quasi-neutral bulk [155]. The optical model assumes that the surfaces can be represented as a planar and Lambertian component mix, and for Lambertian light absorption, the distribution of effective path angles changes with the traveled distance uniquely for each wavelength.

The user can define a specific cell design by establishing: doping concentration of bulk absorber; geometric parameters (length, width and height); configuration and type of contact materials; the effective sheet

resistance of the textured surfaces; optical parameters of surface regions, which can be also related to shadowing of front contacts (e.g. transmission of front surface) or metallization of back contacts (e.g. rear surface reflectance); the lifetime of excess carriers (both minority and majority ones); and surface recombination as well as recombination at surface defects or bulk defects. This enables the simulation of a given device's collection efficiency and external quantum efficiency.

Moreover, by defining an absorption spectrum for a chosen material and illumination spectrum (or establishing a monochromatic approach) used, PC3D can be utilized for  $I$ - $V$  curve calculations, including  $P_{\max}$ ,  $V_{oc}$ ,  $j_{sc}$  identification, as well as determination of profiles for carrier generation and recombination, excess carrier concentration, conductance, bulk current and electrothermal dissipation due to recombination, carrier flows or contact resistance. If needed, additional temperature, doping, or circuit models can be applied for more nuanced simulations.

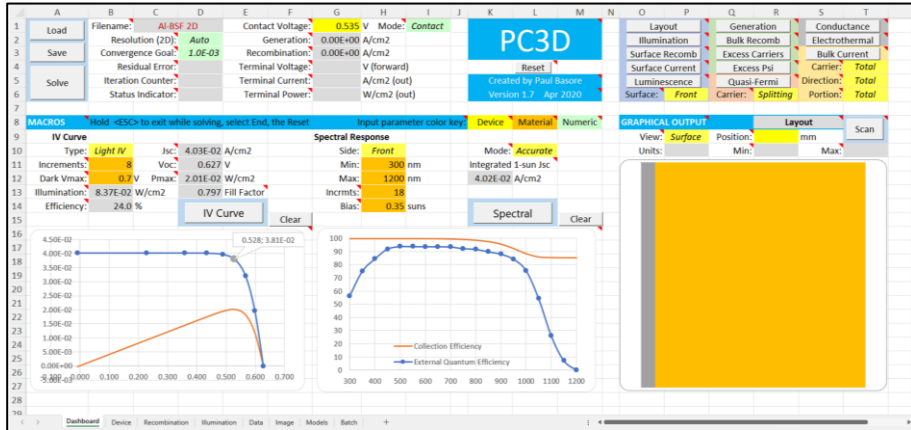


Fig. 31. A sample screenshot of the PC3D main dashboard, taken during calculations of this work.

The creators of PC3D also provide example files for silicon solar cells utilizing Al-BSF, PERC, IBC, and back point contact (BPC) cells with well defined typical architecture and parameter values.



### 3 RESULTS AND DISCUSSION

#### 3.1 First prototype of Solar Simulator with mirror system

Several essential factors were considered when designing the first prototype. The first one was the easy scalability of the design for adaptation to diverse sizes of rectangular modules. As a result, the square shape of the illuminated area and vertical mirrors were selected. These selections also meant a departure from hexagonal LED arrays employed for efficient color mixing in previously demonstrated designs [3, 156]. This also meant that both powerful cool white LED arrays with rectangular metal core printed circuit boards could be employed, simultaneously leading to more complex simulations (Fig. 32).

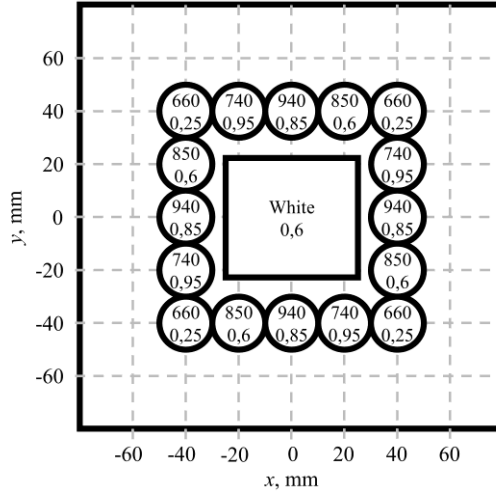


*Fig. 32. Peak wavelengths (in nanometers) and ratios of the required optical power to the maximum one for LEDs [P1].*

The designed LED array was assembled on the aluminum base plate of the custom-built cooling system with a square-shaped mirror system of  $16 \text{ cm} \times 16 \text{ cm}$  base and 20 cm height. This prototype solar simulator used silver-coated glass mirrors of approximately 4 mm thickness. A gap of 5 mm was left between the lower edges of the mirrors and the measurement plane. The irradiance of all LEDs and LED groups was adjusted in several iterations for the best possible spectral match based on the criteria of [139] measured spectral irradiance. Afterward, irradiance distribution was measured, and the results of this measurement are presented in Fig. 33(a).

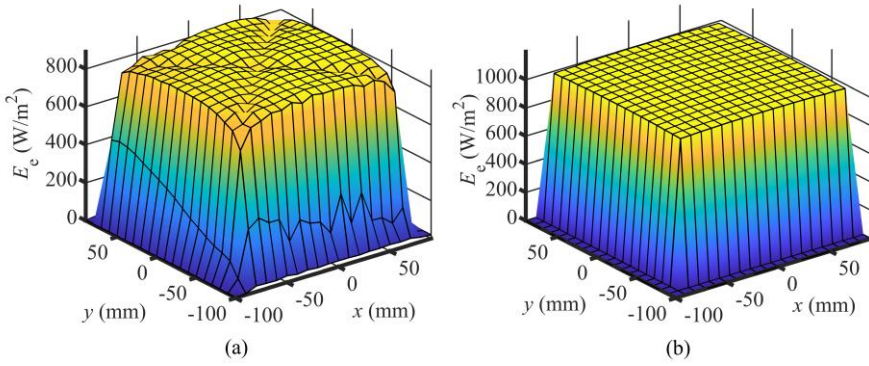


Fig. 33. (a) Measured and (b) simulated irradiance distributions. Dimensions of the metal core printed circuit board (MCPCB) of Bridgelux BXRA-56C9000-J were  $50.8 \times 45.6$  mm. All other MCPCBs were approximately 19 mm in diameter between the mounting holes [P1].

The  $820 - 892 \text{ W/m}^2$  irradiance can be observed in an  $11 \text{ cm} \times 11 \text{ cm}$  central area. It should be noted that this value is obtained for the  $400 - 1100 \text{ nm}$  spectral range and exceeds the requirement of  $759 \text{ W/m}^2$  integral of the tabulated AM1.5G data [8] in this range for one sun irradiance. Unfortunately, essential problems arise due to the “X” shaped area of lower irradiance, which is visible in Fig. 33(a). It limits the area illuminated according to A class requirements (irradiance deviation below 2 % [139]) to just  $8 \times 8 \text{ cm}$ . Furthermore, this area adds constraints for adjusting spectra within the limits of [139], and thus, only a B-class spectral match can be achieved due to a lack of blue light. Additionally, measured irradiance roll-off at the edges is significantly greater and starts earlier than expected from simulations. It is linked to a nonzero gap between the mirror box bottom edges and the spectrometer, as discussed in more detail below.

### 3.1.1 Mirror system simulation

The influence of gaps between the lower mirror box edge and measurement plane and the influence of mirror joints were addressed by an additional ray-tracing simulation series using POV-Ray. First, it was apparent that the proximity of the edges inevitably leads to excess measured  $NU$  compared to A-class requirements. As expected, increasing the gap between the lower mirror box edge and measurement plane (see Fig. 34(a)) resulted in greater and earlier-starting irradiance roll-off. Although the simulated case of a 5 mm gap resembles experimental data quite well, the zero-gap scenario in POV-Ray leads to slightly different results compared to our custom-made code. Second, varying gaps between mirrors at the corners have been

confirmed as the origin of lower illumination values on the diagonals of the measurement plane (see Fig. 34(b)). The gap between the edges of mirrors and the measurement plane of 5 mm was kept constant during this simulation run. So, it shows that even imperfections on a millimeter scale, such as unevenly cut mirror edges or excessive glue, may crucially influence the irradiance distribution.

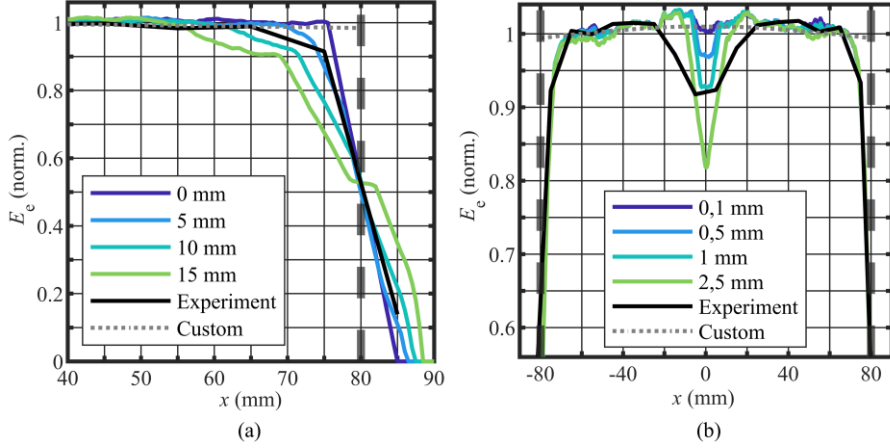


Fig. 34. (a) Dependencies of normalized irradiance on the gap size between the lower mirror box edge and measurement plane and (b) the gap size between mirrors at the corners. “Custom” refers to simulations with custom-made code at 0 mm; “Experiment” refers to measurements with a 5 mm gap [P1].

### 3.1.2 Light source geometry optimization

The origin of the “X” shaped area of lower irradiance can easily be traced to poor mixing due to the central location of the white LED array and imperfections of the mirror system near the corner joints. Irradiance distributions measured for white LED separately and for all other LEDs operating simultaneously are presented in Fig. 35. An “X” shaped area of lower irradiance is visible for white LED, yet much better light mixing is obtained in the case of other LEDs due to their mostly off-axis symmetry locations. Despite the tolerable influence on color mixing properties of the mirror system, these hard-to-account losses near mirror joints and, possibly, other imperfections still lower the overall efficiency of the mirror system. Hence, they also contribute to lower averaged irradiance than predicted by simulations with  $R = 90\%$  assumed reflectance and perfect mirror joints.

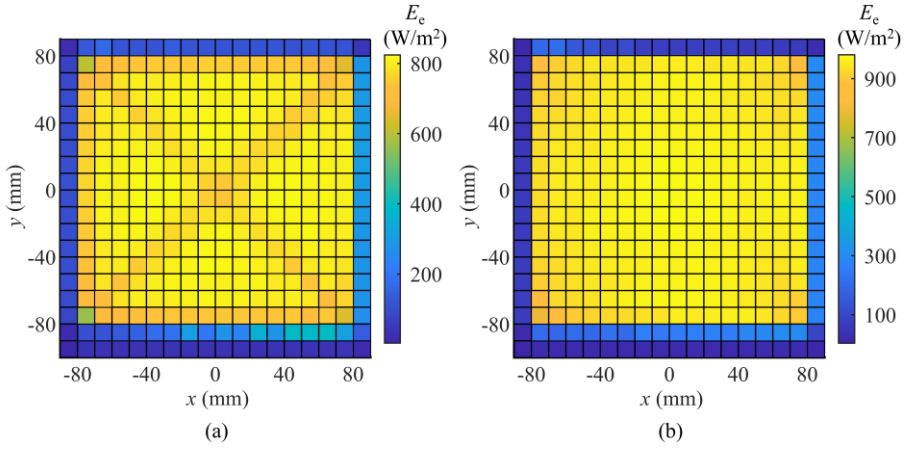


Fig. 35. Measured irradiance distributions with maximum current applied: (a) from white LED array; (b) from all other LEDs. Spectral irradiance distributions were measured first, and the data was integrated afterwards to obtain data for this figure. Minimum irradiance of  $746 \text{ W/m}^2$  is obtained at the center in (a), while the maximum value is  $824 \text{ W/m}^2$  within the central  $80 \text{ mm} \times 80 \text{ mm}$  area. The opposite phenomenon is observed for other LEDs (b), where  $980 \text{ W/m}^2$  maximum is observed near the center, and  $956 \text{ W/m}^2$  minimum is observed in one of the corners [P1].

A series of simulations was employed to address the issues observed while investigating the properties of the first design. First, it was apparent that the proximity of the edges inevitably leads to excess measured  $NU$  compared to A-class requirements. Thus, an enlarged mirror system was studied. A simple mirror-to-mirror distance increase from 16 cm to 20 cm was studied first. Considering the previously discussed available power margin, a single BXRA-56C9000-J array was specified in these simulations. However, this led to increased calculated  $NU$  due to further reduced normalized irradiance near the edges. This feature can be compensated for by an increase of the mirror length to 50 cm, but at the expense of the increased influence of mirror imperfections leading to an increased calculated  $NU$  in the central part (Fig. 36(a)). Smoothing across 15 points was applied to reduce the artifacts occurring due to a finite number of simulated rays. Although this additional problem can be remedied by using two white LED arrays shifted from the center by 23 mm (Fig. 36(b)). These two arrays are used without individual reflectors due to ample optical power available in the first simulator, better mixing of rays from just two arrays, and placement constraints of large  $70 \text{ mm} \times 39 \text{ mm}$  reflectors available for these devices.

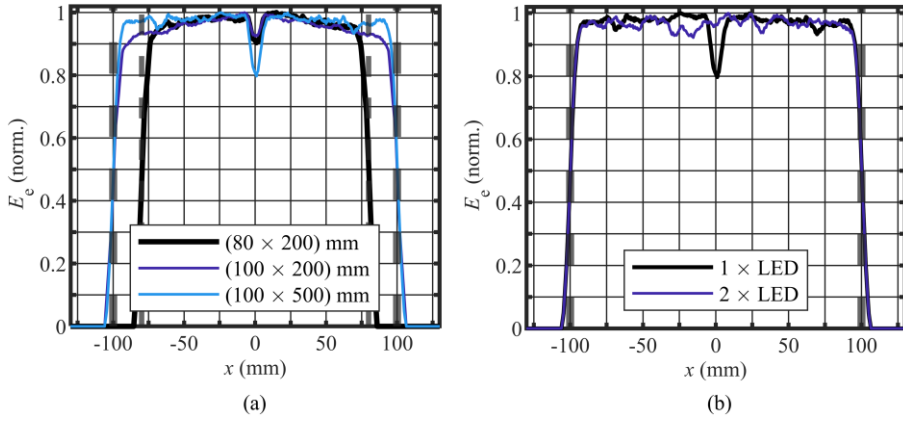


Fig. 36. Simulated normalized irradiance distributions for several sets of (a) mirror box dimensions, and (b) one or two BXRA-56C9000-J arrays [P1].

### 3.1.3 Optimization results

The final layout of simulator after optimization is presented in Fig. 37, together with adjusted positions of other LEDs, which will be discussed later. Enlarged illuminated area and lengthened mirrors also led to a series of other updates. In a previous design (see Fig. 32), 740 and 940 nm devices were operating close to nominal power. Thus, their numbers had to be increased from four to at least six.

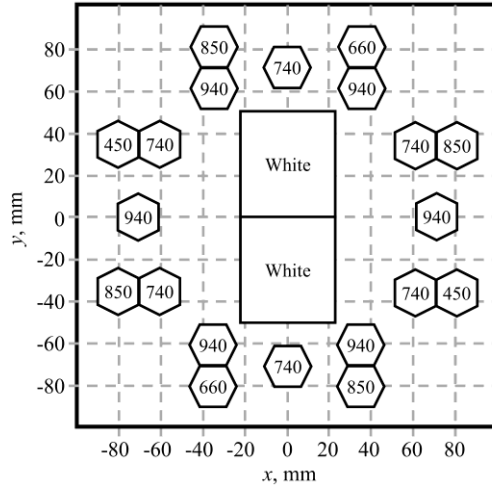


Fig. 37. Updated positions of all LED devices for the second prototype, obtained from optimizations [P1].

Lengthening of the mirrors of the “box” presented the opportunity for better irradiance homogeneity and additional challenges of increased optical losses due to more reflections. Therefore, individual LED reflectors were

considered. Ledil Boomerang C10437 spot type metalized ABS reflectors of up to 90 % optical efficiency were selected to provide narrower initial beams of approximately  $32^\circ$  full-width at half-maximum (FWHM) angle and reduce these external mirror losses. The influence of reflectors was accounted for in simulations using data provided by the manufacturer in EULUMDAT format.

Simulation results for these enhancement scenarios are presented in Fig. 38. Both simulation results for the original array design and two mirror-to-mirror distances (Fig. 38(a)) reveal only “computational noise” due to a finite number of rays, thus confirming the calculated  $NU$  margin available within the design. This margin is only increased when switching to six LEDs and compensates for narrower beams without increasing the calculated  $NU$  (Fig. 38(b)). The same result is also valid for 940 nm array positions, which can be obtained by a simple  $90^\circ$  rotation (see Fig. 37).

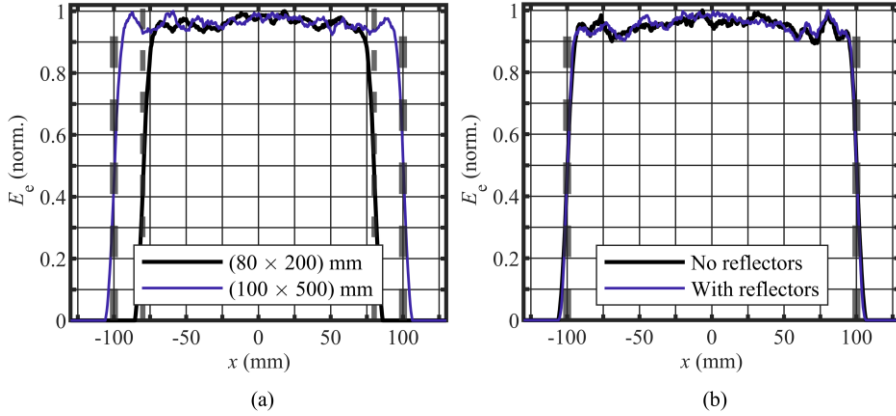


Fig. 38. Simulated normalized irradiance distributions for 740 nm LED arrays: (a) for the original four LED array and various external mirror systems, (b) for the hexagonal six LED array with and without individual reflectors [P1].

The compact placement of the first three LED arrays leaves ample positions for the remaining less powerful LED groups, which are away from the mirror “box” corners and diagonals. An extension of the mirror to a length of 50 cm leads to a relatively uniform calculated irradiance distribution even in the case of only four LEDs of 850 nm peak wavelength with individual reflectors. This result is achieved by placing these devices in a rotated square pattern outside the “rim” of 740 nm and 940 nm LEDs.

Since the majority of blue and red light components in the 400 nm – 500 nm and 600 nm – 700 nm ranges are anyway provided by large and powerful white LED arrays, only two 660 nm devices are envisaged. Also, two 450 nm devices are added for further fine-tuning possibilities.

A real-life version of this simulator design was finalized by dr. Klemensas Laurinavičius. A custom-built aluminum backplane of 4 mm thickness was used as a basis for assembling all LED arrays using screws and thermal paste. Reflectors were mounted to concentrate the radiant flux of LZ4 series LEDs. A plate with LEDs was mounted on a tube-type aluminum heat sink with inner fins, which was forced-air cooled. Afterward, an external mirror system was attached to the same base plate, and the entire simulator prototype was mounted above an optical table. Three double-channel TTi QL564TP programmable power supplies were used as a DC power source for LED devices. Distributions of spectral irradiance within the sample plane were recorded using the measurement system described in Chapter 2.2.

Optimization results are presented in Fig. 39 and Fig. 40. First, irradiance distribution for the entire measurement plane was measured with the spectrometer and cosine corrector at 1 cm steps. These measurement results are presented in Fig. 39. All data is shown in Fig. 39(a). The same data were normalized to a mean irradiance value of  $1043 \text{ W/m}^2$  within the area with  $\leq 2\% \text{ NU}$ , calculated from measurement results according to Eq. (2).

This formula effectively allows for up to 2 % deviation from the mean value to either side, thus only data points between 98 % and 102 % are shown in Fig. 39(b). The rectangle indicates the area of  $14 \text{ cm} \times 13 \text{ cm}$ , which is illuminated according to A-class requirements.

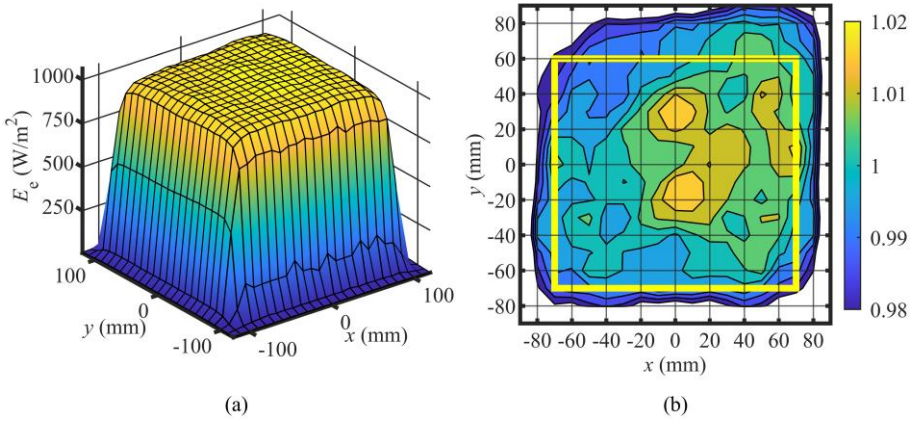


Fig. 39. Characterization results of the second solar simulator prototype: (a) irradiance distribution measured with the spectrometer and the cosine corrector within the entire measurement plane, (b) plot of the same data after normalizing it to  $(E_{e_{\max}} + E_{e_{\min}})/2 = 1043 \text{ W/m}^2 [P1]$ .

Much simpler measurements of short-circuit currents are envisaged in [139] to experimentally evaluate the solar simulator's  $NU$ . Therefore, we also performed photocurrent measurements with BPW 34 B photodiode



(Fig. 40(a)) and calibrated Thorlabs FDS-1010-CAL photodiode (Fig. 40(b)). Thorlabs FDS-1010-CAL provided the possibility of measurements with calibrated sensitivity. Still, it had to be partially covered to maintain currents below the rated maximum of 10 mA, while the entire BPW 34 B photodiode was illuminated during the measurements. Both measurements with photodiodes revealed an even larger area with A-class illumination of  $14\text{ cm} \times 16\text{ cm}$ , which is indicated with a dashed line in Fig. 40(a) and Fig. 40(b). Smoother than predicted by previously discussed simulation results, irradiance reduction near the edges of the mirror system could be noticed in Fig. 39(b). It is much less pronounced in Fig. 40(a) and Fig. 40(b). These differences are consistent with the properties of the CCSA2 cosine corrector described in the manufacturer's datasheet – its normalized efficiency becomes slightly lower compared to the ideal one when departing from the normal incidence. This small efficiency deficit might become important near the edges of the plane with no LEDs directly above. In addition, changes in photodetector responsivities must be considered.

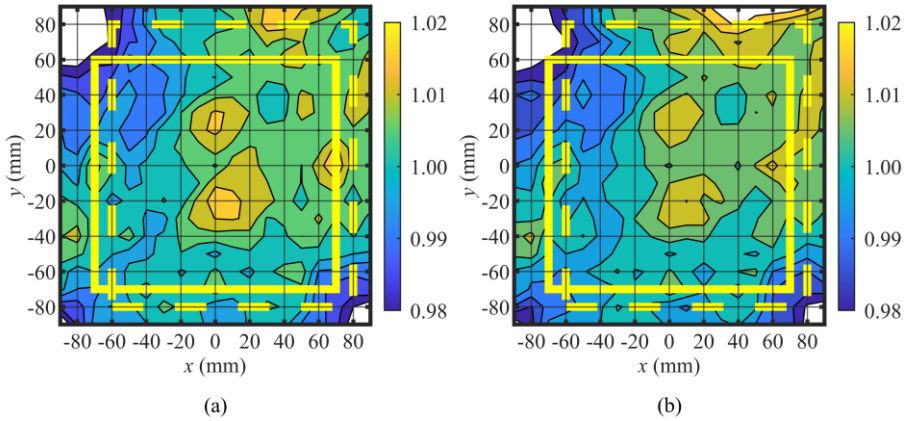


Fig. 40. Photocurrent dependence on coordinates measured with (a) BPW 34 B photodiode and (b) calibrated Thorlabs FDS-1010-CAL photodiode with  $9.3\text{ mm}^2$  clear aperture. Photocurrent values were normalized to the mean values of  $4.9\text{ mA}$  (a) and  $4.28\text{ mA}$  (b), respectively. The thick yellow line indicates a common area for all measurements of at least  $14\text{ cm} \times 13\text{ cm}$ , illuminated according to A-class requirements. Larger areas are obtained when measuring with photodiodes (dashed lines) [P1].

Spectral characterization data is presented in Fig. 41 and Fig. 42. Spectra in the center of the measurement plane, and two points near the corners of the uniformly illuminated area are presented in Fig. 41. Differences in spectra are minor yet could be noticed near  $660\text{ nm}$  due to the small number of LEDs and different distances. Spectral irradiance was integrated within all six spectral



ranges for all data points of a  $14\text{ cm} \times 13\text{ cm}$  rectangle of Fig. 39(b). The result is presented in Fig. 42 and confirms large margins remaining within class A spectral match limits indicated by green dashed lines. These large margins, positions of single-color LED emission peaks near the middle points of the ranges, and the width of the white LED emission spectrum prevent any considerable influence of LED heating and emission drift on the spectral match.

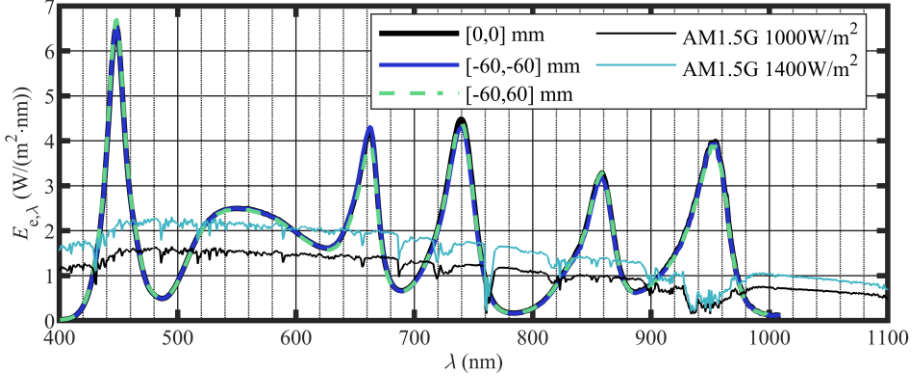


Fig. 41. Spectra of the second solar simulator at the center and near two corners of the measurement plane and reference AM1.5G spectra at 1 Sun and 1.4 Sun irradiance [P1].

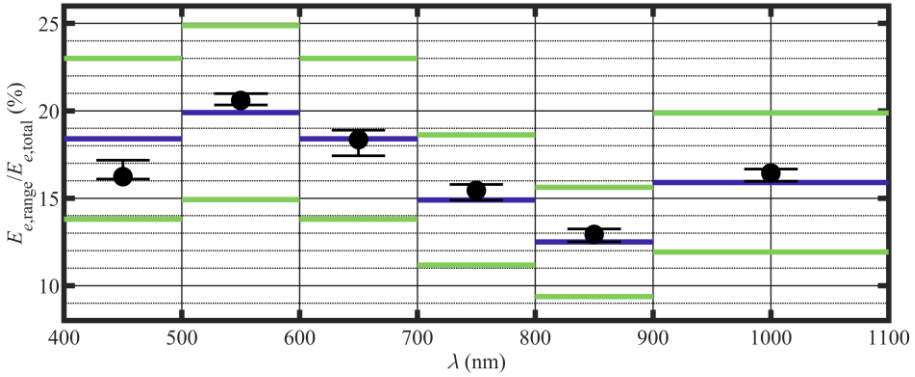


Fig. 42. Distribution of normalized integrated spectral irradiance in all six spectral ranges defined by [3]. Data points are obtained at (0;0), and error bars show the minimum and the maximum deviation in all  $15 \times 14$  points of a  $14\text{ cm} \times 13\text{ cm}$  rectangle of Fig. 39(b). The blue line corresponds to the AM1.5G spectrum, and the green lines indicate the lower and upper limits of deviation for the class A spectral match [P1].

Weighted average responsivities  $R_{\text{avg}}$  were also calculated to reveal further details on how spectra differences might affect the measurement of current–voltage characteristics:

$$R_{\text{avg}} = \frac{\int_{400\text{nm}}^{1000\text{nm}} RE_{e,\lambda} d\lambda}{\int_{400\text{nm}}^{1000\text{nm}} E_{e,\lambda} d\lambda}. \quad (14)$$

First, the responsivity spectrum of an ideal photodiode of 100% quantum efficiency (dashed line in Fig. 28) was processed.  $R_{\text{avg}} = 0.553 \text{ A/W}$  is obtained for the spectrum of our simulator (Fig. 41, [0,0] spectrum). This value is slightly lower than  $R_{\text{avg}} = 0.556 \text{ A/W}$  obtained in the case of AM1.5G spectrum. Lower average responsivity could be expected due to the absence of light above 1000 nm from our LED-based simulator. However, it is mostly offset by a slight deficit of light in the 400 nm – 500 nm range, where sensitivity is lower. Different trends are observed for the FDS-1010-CAL photodiode responsivity spectrum due to low sensitivity above 1000 nm. The average responsivity of 0.409 A/W is calculated for the spectrum of our simulator, and only 0.386 A/W for the AM1.5 G spectrum. These results demonstrate that differences in responsivity spectra of calibrated reference cells and tested cells must be considered even when fully matching AAA class solar simulator requirements.

### 3.1.4 Adhering to the novel standard

The performance of solar simulators can also be evaluated in an extended spectral range of 300 nm to 1200 nm, which was introduced in the most recent standard IEC 60904-9 Ed. 3.0 [4]. Backward compatibility with the wavelength range of 400 nm – 1100 nm is also envisaged in this standard. Without further adjustments, the solar simulator would provide just a B-class spectral match in this extended range due to excess light in the 657 nm – 772 nm range. This excess, however, is easy to remove by simply adjusting the current of 740 nm LEDs. Newly introduced parameters of spectral coverage (*SPC*) and spectral deviation (*SPD*) were evaluated for the extended range based on definitions of [4]. For this solar simulator,  $SPC = 81 \%$  and  $SPD = 72\%$ ; however, IEC 60904-9 Ed. 3.0 also explicitly confirms that there are no requirements defined for these parameters yet. Spatial *NU* and temporal instability would still adhere to the A-class requirements. This spectrum of the experimentally demonstrated AAA class solar simulator will serve as a baseline for further simulations.

### 3.2 Minimal set of light sources for A+ class solar simulators

The introduction of the most recent version of the IEC 60904-9:2020 standard [4] also changed several criteria concerning how solar simulator

spectra must be evaluated. A broader spectral range of 300 nm to 1200 nm is now required, which is split into six narrower bands of nearly equally integrated spectral irradiance. As specified in this standard, almost the entire 300 nm to 1200 nm spectral range is expected to be usable by crystalline or multicrystalline silicon (c-Si or mc-Si) and copper indium gallium diselenide (CIGS) solar cells, with only external quantum efficiency reduction near the edges of this range. Much narrower spectral ranges are assigned to other types of solar cells, such as amorphous silicon (a-Si), cadmium telluride (CdTe), and microcrystalline silicon ( $\mu\text{c-Si}$ ).

The solar simulator spectra were numerically optimized in several steps. First, irradiance from primary sources was adjusted to ensure further compatibility with A+-class requirements at almost 1 Sun irradiance ( $836 \text{ W/m}^2$  in the 300 nm – 1200 nm range) with the minimum number of light sources required (Fig. 43). The naming for all upcoming configurations will be shortened: LED-only simulator configurations will be indicated by the letter “L”, while hybrid ones with halogen lamp-based emitters included will be indicated by the letter “H”. The first digit indicates the number of distinct light sources used (a summarized list can be found in the appendix A1).

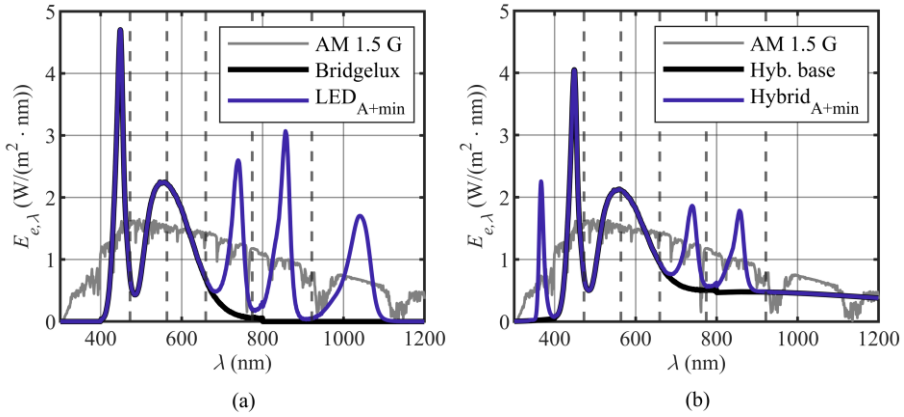


*Fig. 43. Initial simulated spectra designated to be further optimized, shown stepwise in the case of: (a) LED-only simulator and (b) hybrid simulator. Dashed lines correspond to six spectral irradiance intervals defined in [4], with interval numbering starting from the first at 300 nm [P2].*

### 3.2.1 LED-only solar simulator

In the LED-only configuration (Fig. 43(a)), cool white LEDs serve as the main source, providing enough light in the first three spectral intervals. Due to their spectral properties, the minimum irradiance in the first interval with  $d_1 = -12.5 \%$  corresponds to a slight deficiency with  $d_2 = -7.3 \%$  in the

second interval and an excess of light in the third interval with  $d_3 = 8.6 \%$ . Such a selection of the main sources allows us to reach the  $d_i \geq -12.5 \%$  minimum in the next step just by using high-power LEDs of commonly commercially available wavelengths. Minimum irradiance in the fourth and fifth intervals can be reached by adding 740 nm and 850 nm emitters in both (LED-only and Hybrid) simulator configurations. In the LED-only configuration, 1050 nm emitters are added for the sixth interval. Only 4 distinct types of sources in total are sufficient for fulfilling A+-class spectral match requirements. The parameters for the LED<sub>A+min</sub> simulator are presented in Table 4.

Table 4. Parameters of LED<sub>A+min</sub> solar simulator.

Wavelength range interval	$E_{e,\lambda,int} (W/(m^2 \cdot nm))$					SID
	C.White	740 nm	850 nm	1050 nm	Total	
1 <sup>st</sup>	121.55	0.00	0.00	0.00	121.55	-12.50 %
2 <sup>nd</sup>	129.70	0.00	0.00	0.00	129.70	-7.33 %
3 <sup>rd</sup>	151.40	0.33	0.00	0.00	151.73	+8.88 %
4 <sup>th</sup>	28.24	92.94	0.52	0.00	121.70	-12.50 %
5 <sup>th</sup>	1.47	1.37	118.36	0.68	121.88	-12.50 %
6 <sup>th</sup>	0.00	0.00	0.11	121.95	122.06	-12.50 %
Total source $E_e$ ( $W/(m^2 \cdot nm)$ )	432.35	94.65	118.99	122.64	<b>768.62</b>	<b>12.50 %</b>

### 3.2.2 Hybrid solar simulator

In the hybrid configuration (Fig. 43(b)), white LEDs and halogen lamp-based emitters serve as a significant light source combination. An overlap of their spectra might quickly lead to a substantial excess of light in the third interval. By aiming to provide sufficient irradiance from halogen emitters to match the A+ spectrum requirements in at least the sixth spectral interval, we have to limit the irradiance from white LEDs. With the maximum allowable  $d_3 = 12.5 \%$ , compatibility is also ensured in the second ( $d_2 = -10.25 \%$ ) interval, while additional sources remain necessary for the first interval. As in the LED-only case, minimum irradiance can be reached in the fourth and fifth intervals by adding 740 nm and 850 nm emitters. In the hybrid simulator configuration, 365 nm UV LEDs can correct for the light deficiency in the first interval. Only 5 different types of sources in total are sufficient for fulfilling A+-class spectral match requirements. The parameters for the Hybrid<sub>A+min</sub> simulator are presented in Table 5.

Table 5. Parameters of Hybrid<sub>A+min</sub> solar simulator.

Wavelength range interval	$E_{e,\lambda,int} (W/(m^2 \cdot nm))$						SID
	365 nm	C.White	740 nm	850 nm	Halogen	Total	
1 <sup>st</sup>	37.40	102.08	0.00	0.00	7.89	147.37	+6.09 %
2 <sup>nd</sup>	0.00	108.92	0.00	0.00	16.53	125.45	-10.36 %
3 <sup>rd</sup>	0.00	127.15	0.18	0.00	29.45	156.78	+12.50 %
4 <sup>th</sup>	0.00	23.71	49.94	0.22	47.83	121.70	-12.50 %
5 <sup>th</sup>	0.00	1.23	0.74	50.40	69.51	121.88	-12.50 %
6 <sup>th</sup>	0.00	0.00	0.00	0.05	122.01	122.06	-12.50 %
Total source $E_e$ ( $W/(m^2 \cdot nm)$ )	37.40	363.09	50.86	50.67	293.22	<b>795.24</b>	<b>12.50 %</b>

### 3.3 Reduction of SMM – 1 factor

After the first step of creating minimal-source simulators, we have two solar simulator configurations with  $|d_i| \leq 12.5 \%$  and available irradiance margin for either adjusting or adding supplementary sources, depending on specific requirements for various types of solar cells.

Additional minimal set is needed for the c-Si case because the spectral response drops at the wavelengths somewhere between 940 nm and 1050 nm (these values correspond with the types of LEDs used). For this purpose, two sets were simulated: L4.1 and L4.2. In the L4.2 case, all LED devices were the same as those used in the first prototypes. Therefore, the same spectral coverage is retained, since spectra of the removed 660 nm and 450 nm LEDs overlap well with the spectrum of the white one. On the other hand, removing these LEDs leads to an increased SPD of 76 %.

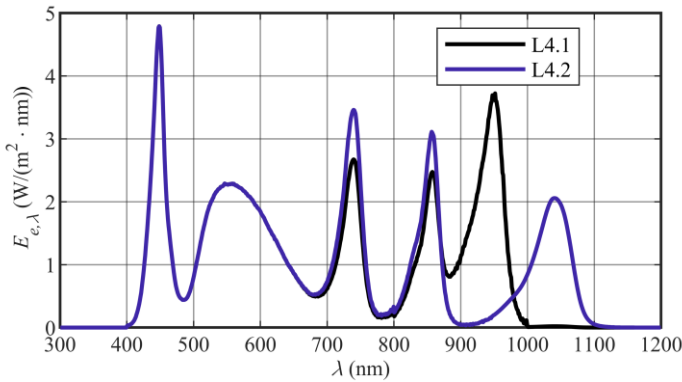


Fig. 44. Spectra of the two starting LED sets L4.1 and L4.2 [P3].

Configuration L4.2 with 1050 nm LED (see Fig. 44) possesses both higher spectral coverage and lower spectral deviation. This result can be attributed to the location of wide, strong absorption bands in the standard AM1.5G spectrum. The spectrum of 940 nm LED overlaps with one of such bands, while one of the 1050 nm LEDs matches the atmospheric transmission window. Therefore, a better spectrum approximation is obtained with a latter one.

In both L4.1 and L4.2 configurations, white LEDs contribute all integrated spectral irradiance in the first three spectral intervals, leading to an exact match of both spectra. The properties of white LEDs and the absence of other light sources also set the limits for  $d_i$  optimization with this set of light sources; cumulative irradiance in the first interval cannot be increased due to excess light in the third one. The parameters for L4.1 and L4.2 simulators are presented in Table 6.

Table 6. Properties of LED-only L4.1 and L4.2 simulator configurations.

	$E_{e\lambda\_int}$ (W/(m <sup>2</sup> · nm))					TOTAL $E_c$ (W/(m <sup>2</sup> nm))	
Source type	C.White	740 nm	850 nm	940 nm	1050 nm		
L4.1	440	97	88	211			
L4.2	440	127	121		148		
	$d_i$ (%)						
Interval	1 <sup>st</sup>	2 <sup>nd</sup>	3 <sup>rd</sup>	4 <sup>th</sup>	5 <sup>th</sup>	6 <sup>th</sup>	$SID$
L4.1	−10.9	−5.6	10.9	−10.5	5.5	10.6	10.9 %
L4.2	−10.9	−5.7	10.9	10.9	−10.9	5.7	10.9 %

### 3.3.1 c-Si

While both four-LED simulators satisfy A+ class spectrum requirements with a margin, their  $SMM - 1$  factors are of the opposite signs when the reference AM1.5G spectrum, and one with  $k = 4$  are compared: negative in the case of L4.1 configuration and positive in the case of the L4.2 configuration. This difference can be attributed to the positions of these peaks with respect to the curve-breaking point in the responsivity dependence on wavelength (Fig. 27): only 1050 nm LEDs would contribute additional photocurrent in the case of solar cells with higher sensitivity above 1000 nm. These results suggest that the influence of the spectral mismatch could be substantially reduced by mixing the light from L4.1 and L4.2 LED sets, switching to a configuration with five LED types.

The dependence of  $SMM - 1$  factor on the irradiance from 1050 nm LED is shown in Fig. 45(b). At approximately 77 % contribution from the L4.2 of LEDs  $SMM - 1 = 0$  is obtained at  $k = 4$  once the responsivity dispersion in both the UV and IR regions is included simultaneously. However, in practice, the front and back of a solar cell can be optimized separately. Since UV light is mostly absorbed near the front surface of solar cells, and part of the IR light can reach the back of the cells, an independent reduction of spectral mismatch effects in the IR and UV ranges would be more comprehensive. Once only responsivity dispersion in the IR range is considered, the optimal contribution percentage from the L4.2 set of light sources shifts to 62 %. Higher in comparison with four-LED configurations, the value of  $SPC = 89 %$  and a lower value of  $SPD = 63 %$  are also obtained for the L5 configuration as a side result.

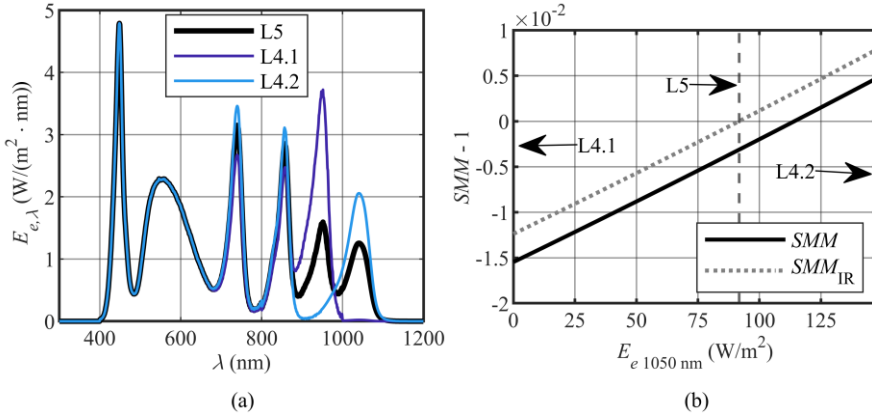


Fig. 45. (a) Spectra of the two starting LED sets and a combination of them L5 in optimal proportion with respect to spectral mismatch error in the IR range and (b) spectral mismatch error (at  $k = 4$ ) and contribution of the IR part to it (at  $k = 4$ ) as a function of the 1050 nm LED power for c-Si technology [P3].

The absence of UV sources in the two four-LED configurations leads to the residue of  $SMM - 1$  factor, which can be corrected by adding UV LEDs. After assessing available additional LEDs, the lowest  $SMM - 1$  factors were obtained with 365 nm LEDs. The resulting L6 spectrum is shown in Fig. 46(a), and the dependences of  $SMM - 1$  ( $k = 4$ ) on the added LED irradiance from 365 nm LEDs are presented in Fig. 46(b). To maintain constant irradiance, the contribution of white LEDs was reduced when one of the UV LEDs in this simulation series was increased. The addition of UV sources compensated for the initial lack of irradiance in the first interval, and available margins in the second and third intervals were sufficient to keep all spectra within A+ requirements.

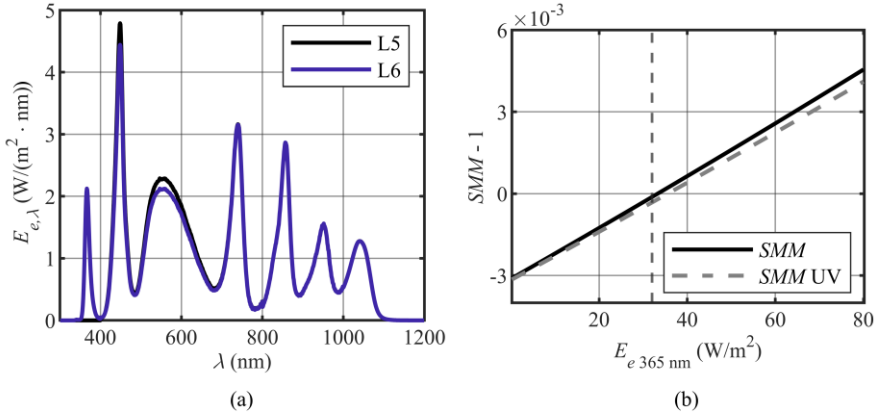


Fig. 46. (a) Spectra of LED only solar simulators: one with 5 and 6 LED types, and (b) spectral mismatch and contribution of the UV part to it ( $k = 4$ ) as a function of the irradiance from the added 365 nm UV LED for the 6-LED solar simulator for c-Si technology [P3].

At  $32\ \text{W}/\text{m}^2$  irradiance from a 365 nm LED, more than one order of magnitude improvement over the initial four-LED configuration is achieved. This irradiance corresponds to the maximum UV LED power limit for A+ class spectrum and is indicated by a vertical dashed line in Fig. 46(b). The addition of 365 nm UV LED also improves both spectral coverage and spectrum deviation to  $SPC = 92\%$  and  $SPD = 61\%$ , respectively. Spectral mismatch errors for all mentioned configurations are presented in Fig. 47, together with their UV and IR components.

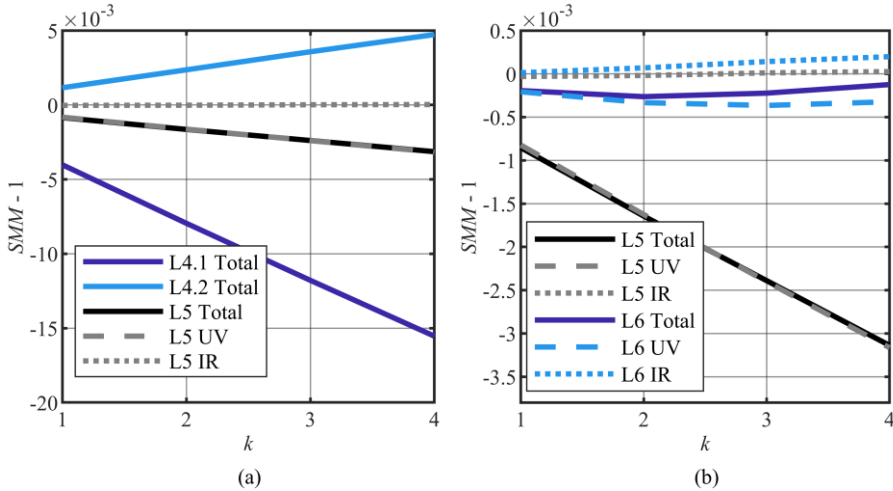


Fig. 47. Spectral mismatch error, as a function of dispersion multiplier  $k$ , for LED-only, c-Si optimized, spectra: (a) L4.1, L4.2, and their combination – L5 spectrum with UV and IR components, (b) L5 and L6 with their UV and IR components [P3].



In the case of a hybrid setup, a broad spectrum of halogen emitters provides an efficient option to improve the spectral coverage between 1100 nm and 1200 nm, while simultaneously replacing one or two LED sources. The H5 spectrum in Fig. 48(a) represents the case of just five distinct types of light sources. It fits into the A+ class requirements with the value of  $SID = 12.3\%$ . This value is caused by two primary reasons: first, the overlap of spectra of white LEDs and halogen emitters leads to excess irradiance in the third interval and to the lack of light in the second and fourth intervals. As a result of better coverage in the IR range,  $SPC = 97\%$  and  $SPD = 38\%$  are achieved.

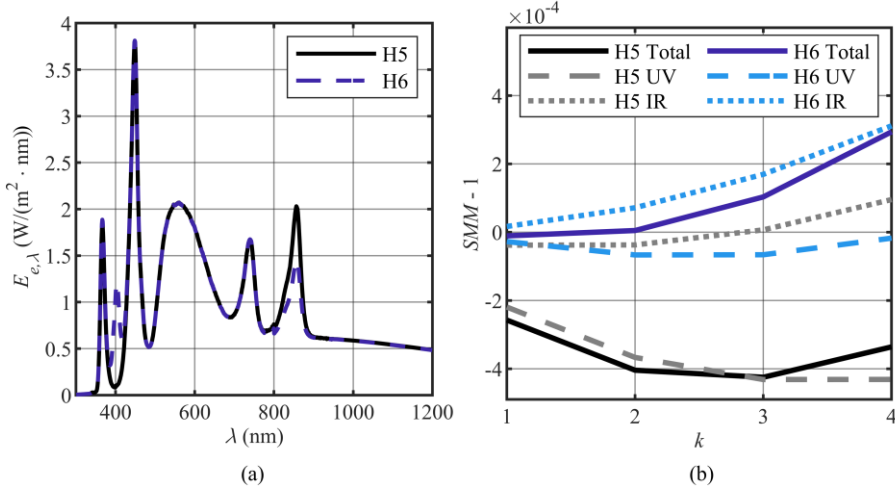


Fig. 48. (a) Spectra of hybrid solar simulators: based on four or five types of LEDs, and a halogen emitter array, optimized for c-Si technology and (b) spectral mismatch error, as a function of dispersion multiplier  $k$  for both spectra with their UV and IR components [P3].

Further improvements can be achieved by adding 405 nm LEDs (see H6 spectrum in Fig. 48(a)), and, simultaneously, filling the gap between the spectra of 365 nm and white LEDs. This leads to further improvement and  $SPC = 98.3\%$ . Multiple light sources in the 1<sup>st</sup> interval and the corresponding fine-tuning possibilities allow for a very low value of  $SMM_{UV} - 1 = -1.8 \cdot 10^{-5}$ , and still low  $SMM_{IR} - 1 = 3.1 \cdot 10^{-4}$  due to retained halogen emitter contribution at the longest wavelengths. Irradiance from 850 nm LEDs had to be reduced to maintain the total irradiance. Parameters for all four mentioned LED-only and hybrid solar simulators are presented in Table 7.

Table 7. Properties of LED-only L5 and L6, and hybrid H5 and H6 solar simulator configurations optimized for c-Si technology.

Source type	$E_{e,\lambda\_int} (W/(m^2 \cdot nm))$								TOTAL
	365 nm	405 nm	C.White	740 nm	850 nm	940 nm	1050 nm	Halo	$E_e (W/(m^2 \cdot nm))$
L5			440	116	108	80	92		836
L6	32		408	116	108	80	92		836
H5	27		339	39	55			376	836
H6	28	23	339	39	32			375	836

Interval	$d_i (\%)$						SID
	1 <sup>st</sup>	2 <sup>nd</sup>	3 <sup>rd</sup>	4 <sup>th</sup>	5 <sup>th</sup>	6 <sup>th</sup>	
L5	-10.9	-5.6	10.9	2.7	-4.5	7.5	10.9 %
L6	5.7	-12.5	2.9	1.4	-4.6	7.6	12.5 %
H5	-4.6	-12.4	12.3	-12.2	4.6	12.2	12.4 %
H6	12.2	-12.2	12.2	-12.2	-11.8	11.8	12.2 %

### 3.3.2 a-Si

Starting with LED<sub>A+min</sub> spectrum, the following steps were taken to optimize the LED-only solar simulator for a-Si solar cells (Fig. 49):

1. Addition of 365 nm LEDs to lower *SMM* on the UV side;
2. Adjustment of 740 nm LEDs up to total AM1.5G irradiance required to lower *SMM* on the red/IR side of the spectrum (resulting in A+-class spectrum).

Additional steps:

3. Adjustment of 740 nm LEDs to further lower *SMM* on the red/IR side of the spectrum, sacrificing the class of the spectrum (bringing down to A-class);
4. Matching the AM1.5G 1 Sun irradiance by lowering the optical power from all LEDs except 740 nm.

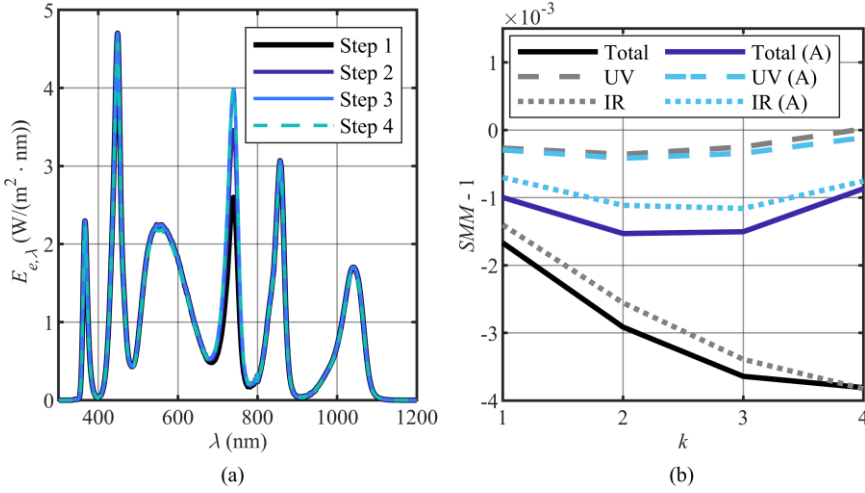


Fig. 49. Results of LED-only simulator optimization for a-Si solar cells: (a) simulated spectra after each optimization step, (b) spectral mismatch error, as a function of dispersion multiplier  $k$  for final optimized spectra with their UV and IR components.

First, a 365 nm LED was added to lower  $|SMM - 1|$  on the UV side. The value of  $E_{e\ 365\text{ nm}} = 34.6\text{ W/m}^2$  (Fig. 50(a)) was selected and fixed, resulting in the lowest mismatch. After that, 740 nm LED power adjustments were made to improve the situation on the red/IR side. At this step,  $E_{e\ 740\text{ nm}} = 127.5\text{ W/m}^2$  has been chosen as the maximal power still adhering to A+-class requirements in the 4<sup>th</sup> interval while simultaneously matching total required irradiance (Fig. 50(b)). Meanwhile, adjustment of 850 nm LED proved unnecessary due to an arbitrarily small influence on  $|SMM - 1|$  parameter at the red/IR side of the spectrum.

Additionally, the spectrum was tweaked to lower  $|SMM - 1|$  even more by allowing a spectral match of A-class only. By selecting 740 nm irradiance at  $E_{e\ 740\text{ nm}} = 147.5\text{ W/m}^2$  (borderline A-class value) at step 3 and lowering the power of all LEDs except the 740 nm one at step 4, maximal  $|SMM - 1|$  dropped more than 3 times (Fig. 50(b)). Such pronounced influence of 740 nm can be attributed to the edge of spectral responsivity of a-Si solar technology sharply dropping in the 650 nm – 800 nm range (Fig. 27). In both A+-class and A-class solutions,  $SPC = 88.7\%$ , while  $SPD$  gets marginally higher, from  $SPD_{A+} = 65.6\%$  to  $SPD_A = 66.0\%$ .

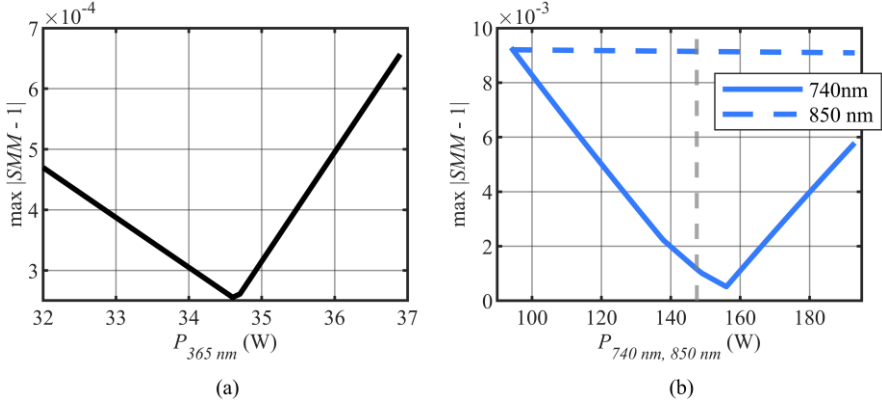


Fig. 50. (a) Spectral mismatch error of UV-side dependence on irradiance of 365 nm LEDs during step 1 (selected  $E_{e\ 365\text{ nm}} = 34.6\text{ W/m}^2$ ), (b) spectral mismatch error of IR-side dependence on the irradiance of red LEDs during step 2 (selected  $E_{e\ 740\text{ nm}} = 127.5\text{ W/m}^2$ ) and step 3 (selected  $E_{e\ 740\text{ nm}} = 147.5\text{ W/m}^2$ ). The dashed vertical line indicates the upper irradiance limit for a 740 nm LED to fulfill A-class requirements.

Starting with the Hybrid<sub>A+min</sub> spectrum, the following steps were taken to optimize the hybrid solar simulator for a-Si solar cells (Fig. 51):

1. Small adjustment of 365 nm LEDs for better *SMM* on the UV side of the spectrum;
2. Adjustment of 740 nm LEDs to lower *SMM* on the red/IR side of the spectrum, as well as making tiny adjustments to the Cool White source to stay in class A+ in the 4<sup>th</sup> interval;
3. Adjustment of 850 nm LEDs to match total AM1.5G irradiance.

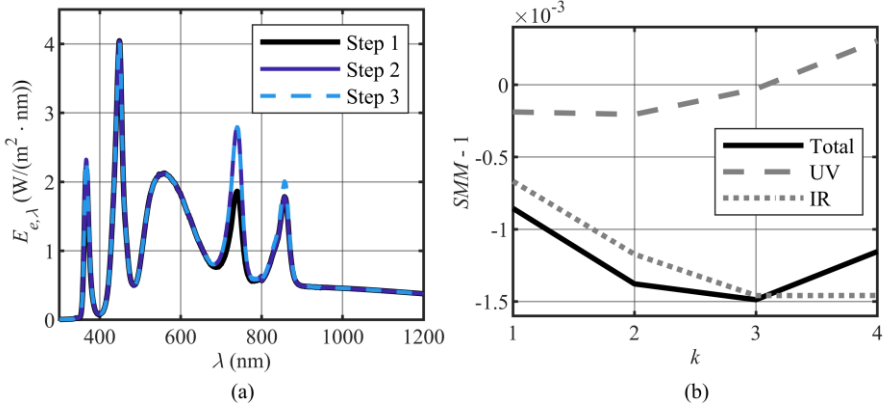


Fig. 51. Results of Hybrid simulator optimization for a-Si solar cells: (a) simulated spectra after each optimization step, (b) spectral mismatch error, as a function of dispersion multiplier  $k$  for final optimized spectrum with its UV and IR components.

Similar to the LED-only simulator, at the first step, 365 nm LEDs were adjusted to fit a-Si technology better and lower  $|SMM - 1|$  of the UV side. In this case, the same value of  $E_{e\ 365\ \text{nm}} = 34.6\ \text{W/m}^2$  was selected and fixed (Fig. 52(a)), although in general it could be different in case the power of the Cool White source was drastically changed. In this case, the Cool white source was lowered by less than 1 W while adding more power to 740 nm LEDs during step 2 (Fig. 52(b)).  $E_{e\ 740\ \text{nm}} = 86.2\ \text{W/m}^2$  was selected and fixed as the upper power limit to stay in A+-class in the 4<sup>th</sup> interval. To achieve the total AM1.5G irradiance required, during the last step, 850 nm LEDs were adjusted (Fig. 52(c)) up to  $E_{e\ 850\ \text{nm}} = 59.3\ \text{W/m}^2$ , while broadband sources (Cool White and Halogen) had to stay fixed, because changes to their power would influence some intervals out of A+-class. Overall, the hybrid simulator shows smaller  $|SMM - 1|$  values compared to the LED-only one, because the halogen source widely covers the 650 nm – 800 nm wavelength range with less pronounced valleys. Moreover, spectral coverage and deviation are significantly improved to  $SPC = 97\%$  and  $SPD = 44.8\ \%$ , respectively.

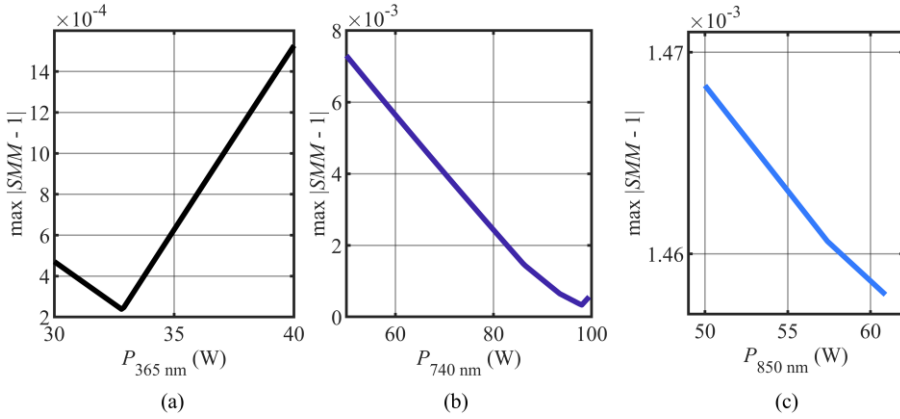


Fig. 52. (a) Spectral mismatch error of UV-side dependence on irradiance of 365 nm LEDs during step 1 (selected  $E_{e\ 365\ \text{nm}} = 34.6\ \text{W/m}^2$ ), (b) Spectral mismatch error of IR side dependence on irradiance of 740 nm LEDs during step 1 (selected  $E_{e\ 740\ \text{nm}} = 86.2\ \text{W/m}^2$ ), and (c) spectral mismatch error of IR-side dependence on the irradiance of 850 nm LEDs during step 2 (selected  $E_{e\ 850\ \text{nm}} = 59.3\ \text{W/m}^2$ ).

Parameters of both solar simulators optimized for a-Si technology are presented in Table 8.

Table 8. Properties of LED-only L5 and hybrid H5 simulator configurations for a-Si technology.

Source type	$E_{e,\lambda, \text{int}}$ (W/(m <sup>2</sup> · nm))						TOTAL $E_e$ (W/(m <sup>2</sup> nm))
	365 nm	C.White	740 nm	850 nm	1050 nm	Halo	
L5 <sub>A+</sub>	34.6	432.4	127.5	119	112.6		836.1
L5 <sub>A</sub>	33.6	420.2	147.5	115.6	119.2		836.1
H5	34.6	362.8	86.2	59.3		293.2	836.1

Interval	$d_i$ (%)						SID
	1 <sup>st</sup>	2 <sup>nd</sup>	3 <sup>rd</sup>	4 <sup>th</sup>	5 <sup>th</sup>	6 <sup>th</sup>	
L5 <sub>A+</sub>	12.41	-7.32	8.96	10.71	-12.16	-12.5	12.5 %
L5 <sub>A</sub>	12.41	-7.32	9.01	24.82	-11.95	-12.5	24.8 %
H5	4.00	-10.43	12.5	12.47	-5.95	-12.50	12.5 %

### 3.3.3 CdTe

Starting with LED<sub>A+min</sub> spectrum, the following steps were taken to optimize the LED-only solar simulator for CdTe solar cells (Fig. 53):

1. Adjustment of 740 nm LEDs to lower *SMM* on the red/IR side of the spectrum;
2. Addition of 365 nm LEDs to lower *SMM* on the UV side;
3. Adjustment of 1050 nm LEDs to match total AM1.5G irradiance required.

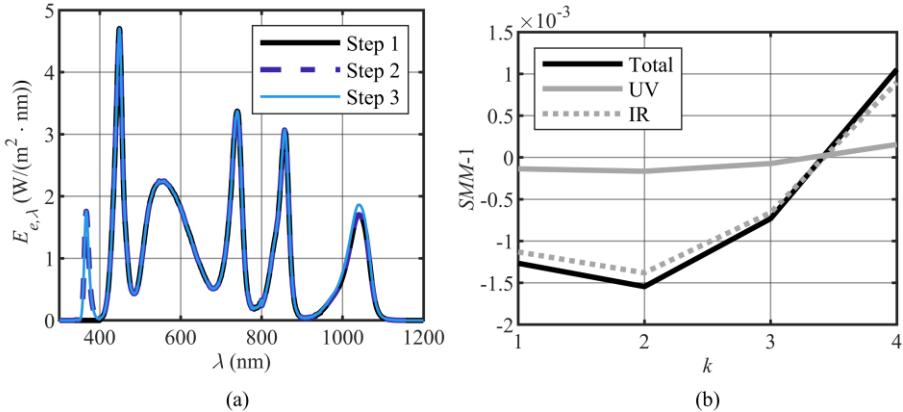


Fig. 53. Results of LED-only simulator optimization for CdTe solar cells: (a) simulated spectra after each optimization step, (b) spectral mismatch error, as a function of dispersion multiplier  $k$  for final optimized spectrum with its UV and IR components [P2].

First, adjustments of both far red 740 nm and 850 nm IR LEDs were evaluated (Fig. 54(a)). Additional irradiance from 850 nm LEDs was found to be detrimental due to the increase in the  $|SMM - 1|$  deviation. Therefore, it was left at the minimum required for an A+-class spectrum in the fifth interval. Adjustment of 740 nm LEDs led to the improvement of this parameter at  $E_{e\ 740\text{ nm}} = 124\text{ W/m}^2$  irradiance, which was then used for the next step. Afterwards, adding 365 nm LEDs led to the minimum  $|SMM - 1|$  value at  $E_{e\ 365\text{ nm}} = 26.5\text{ W/m}^2$  (Fig. 54(b)). Again, this value was fixed before the next step. Finally, to obtain the total required irradiance, 1050 nm LEDs were adjusted. Due to the lack of responsivity of CdTe solar cells in this range, this adjustment did not influence  $SMM$  values (Fig. 54(c)).

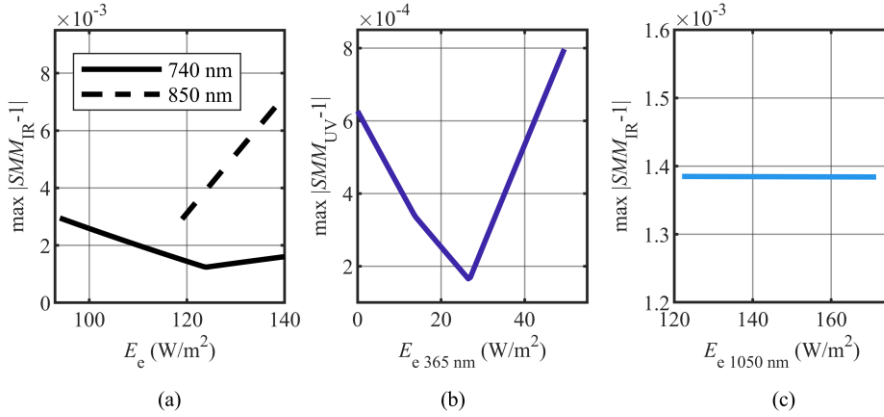


Fig. 54. (a) Spectral mismatch error of IR-side dependence on the irradiance of red LEDs during step 1 (selected  $E_{e\ 740\text{ nm}} = 124\text{ W/m}^2$ ), (b) spectral mismatch error of UV-side dependence on irradiance of 365 nm LEDs during step 2 (selected  $E_{e\ 365\text{ nm}} = 26.5\text{ W/m}^2$ ), and (c) spectral mismatch error of IR-side dependence (or shown lack of) on irradiance of 1050 nm during step 3 (selected  $E_{e\ 1050\text{ nm}} = 134.3\text{ W/m}^2$ ) [P2].

In a similar fashion to the LED-only simulator, starting with the Hybrid<sub>A+min</sub> spectrum, the following steps were taken to optimize the hybrid solar simulator for CdTe solar cells (Fig. 55):

1. Adjustment of the irradiance from halogen lamps to lower  $SMM$  on the red/IR side of the spectrum;
2. Lowering of the irradiance from cool white LEDs to fit into the A+ spectrum limits in the third interval;
3. Adjustment of 365 nm LEDs to lower  $SMM$  on the UV side of the  $EQE$  spectrum;
4. Adjustment of 740 nm and 850 nm LEDs to match the total AM1.5G irradiance required.

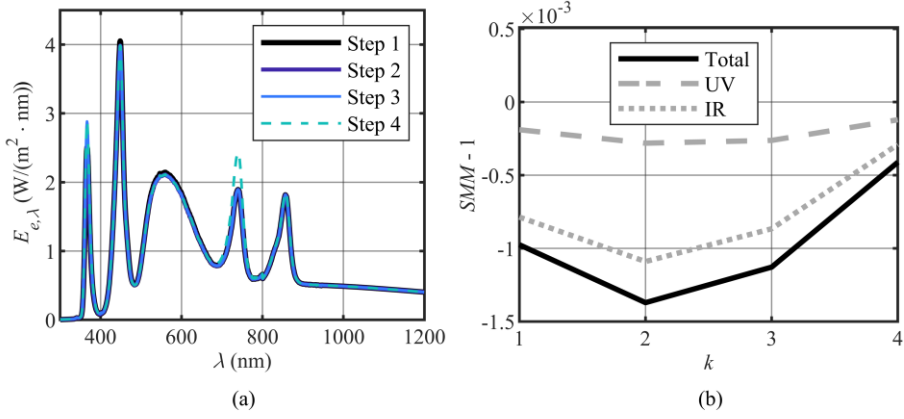


Fig. 55. Results of hybrid simulator optimization for CdTe solar cells: (a) simulated spectra after each optimization step, and (b) spectral mismatch error, as a function of dispersion multiplier  $k$  for the final optimized spectrum with its UV and IR components [P2].

First, the halogen lamp irradiance adjustment led to  $|SMM - 1|$  minimum at  $E_{e \text{ Halogen}} = 313 \text{ W/m}^2$ . This value was then fixed for the next step (Fig. 56(a)). Afterwards, the irradiance of cool white LEDs was lowered to  $E_{e \text{ C.White}} = 357 \text{ W/m}^2$  and fixed to fulfill A+-class irradiance requirements in the third interval. Then, adjustment of 365 nm LEDs led to the minimum  $|SMM - 1|$  value at  $E_{e \text{ 365 nm}} = 43 \text{ W/m}^2$  (Fig. 56(b)). Again, this value was fixed before the next step.

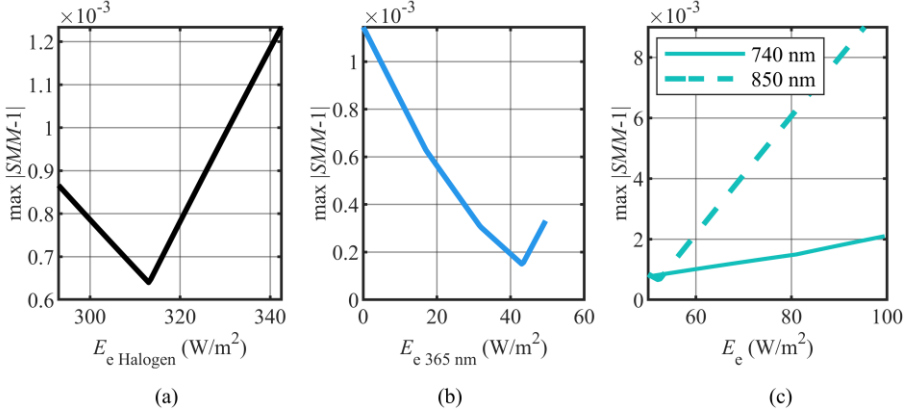


Fig. 56. (a) Spectral mismatch error of IR-side dependence on irradiance of the halogen source during step 1 (selected  $E_{e \text{ Halogen}} = 313 \text{ W/m}^2$ ), (b) spectral mismatch error of UV-side dependence on irradiance of 365 nm LEDs during step 3 (selected  $E_{e \text{ 365 nm}} = 43 \text{ W/m}^2$ ), and (c) spectral mismatch error of IR-side dependence on irradiance of red LEDs during step 4 (selected  $E_{e \text{ 740 nm}} = 67.1 \text{ W/m}^2$ ,  $E_{e \text{ 850 nm}} = 52 \text{ W/m}^2$ ) [P2].



Finally, adjustments of both far red 740 nm and 850 nm LEDs were evaluated (Fig. 56(c)). The  $|SMM - 1|$  trough for 850 nm LEDs was found at  $E_{e\ 850\text{ nm}} = 52\text{ W/m}^2$ , so this value was fixed, and the irradiance of 740 nm LEDs was set to  $E_{e\ 740\text{ nm}} = 67.1\text{ W/m}^2$ , thus obtaining the total required irradiance. Although the  $|SMM - 1|$  values increased after the last step, there is an irradiance limitation in the third interval produced by combining the spectra of cool white LEDs and halogen lamps, leaving the red LEDs the only option to adjust.

Alternatively, further reduction of  $|SMM - 1|$  is possible if the requirement for the A+-class spectrum is relaxed. In this case, after step 1, the irradiance of 740 nm and cool white LEDs was adjusted to their optimal values for minimal  $\max|SMM - 1|$  values on the IR side, also allowing for minimal values of  $\max|SMM - 1|$  to be achieved. After scaling the irradiance of every LED type proportionally up to the required AM1.5G value, the obtained spectrum was class A only due to spectral deviation in the third interval ( $d_3 = +16.9\%$ ). Superimposed spectrum and  $SMM - 1$  factor are presented in Fig. 57.

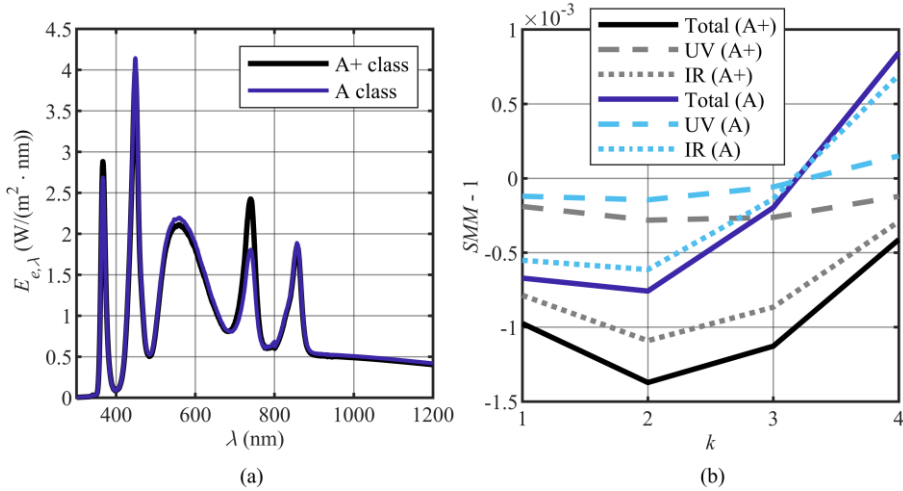


Fig. 57. (a) Simulated spectra of A+-class and A-class simulators and (b) spectral mismatch error, as a function of dispersion multiplier  $k$  for the final optimized spectra with their UV and IR components, for CdTe technology [P2].

The properties of both LED-only and Hybrid solar simulators for CdTe technology are presented in Table 9.

Table 9. Properties of LED-only L5 and hybrid H5 simulator configurations for CdTe technology.

Source type	$E_{e,\lambda, \text{int}}$ (W/(m <sup>2</sup> · nm))						TOTAL $E_e$ (W/(m <sup>2</sup> nm))
	365 nm	C.White	740 nm	850 nm	1050 nm	Halo	
L5	26.5	432.4	124	119	134.3		836.1
H5	47	357	67.1	52		357	836.1
H5A	40	371.3	46.8	52.7		325.3	836.1

Interval	$d_i$ (%)						SID
	1 <sup>st</sup>	2 <sup>nd</sup>	3 <sup>rd</sup>	4 <sup>th</sup>	5 <sup>th</sup>	6 <sup>th</sup>	
L5	6.58	-7.32	8.95	8.23	-12.15	-4.22	12.15 %
H5	12.15	-10.88	12.43	1.02	-8.03	-6.60	12.43 %
H5A	10.27	-7.31	16.86	-11.21	-5.62	-2.94	16.86 %

### 3.3.4 $\mu\text{c-Si}$

Starting with LED<sub>A+min</sub> spectrum, the following steps were taken to optimize the LED-only solar simulator for  $\mu\text{c-Si}$  solar cells (Fig. 58):

1. Addition of 365 nm LEDs to lower *SMM* on the UV side of the spectrum;
2. Adjustment of 1050 nm LEDs to lower *SMM* on the IR side;
3. Adjustment of 740 nm LEDs to match the total AM1.5G irradiance.

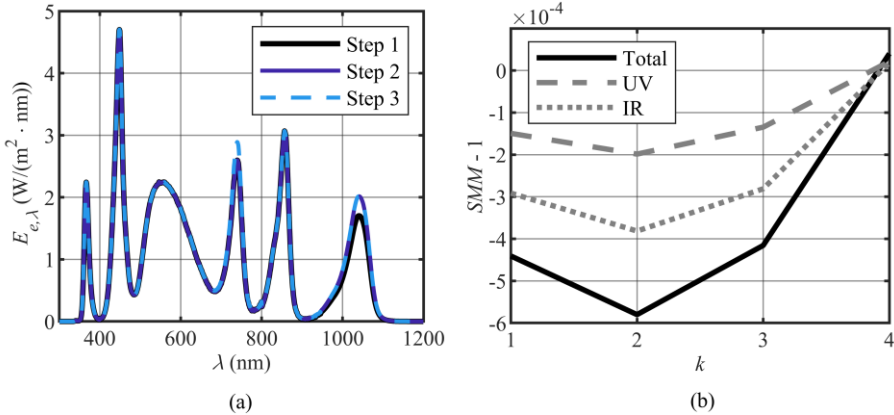


Fig. 58. Results of LED-only simulator optimization for  $\mu\text{c-Si}$  solar cells: (a) simulated spectra after each optimization step, (b) spectral mismatch error, as a function of dispersion multiplier  $k$  for final optimized spectrum with its UV and IR components [P2].

First, 365 nm LEDs were added to minimize  $|SMM - 1|$  in the UV part (Fig. 59(a)). The value of  $E_{e\ 365\ \text{nm}} = 33.8\ \text{W/m}^2$  was found to be optimal and fixed for the next steps. Then, the irradiance of 1050 nm LEDs was adjusted to  $E_{e\ 1050\ \text{nm}} = 145.2\ \text{W/m}^2$ , minimizing  $|SMM - 1|$  on the IR side of the spectrum (Fig. 59(b)). This value was fixed for the next step. Lastly, adjustments of both far red 740 nm and 850 nm LEDs were evaluated (Fig. 59(c)). The infrared part of  $|SMM - 1|$  was found to be more sensitive to irradiation changes of 850 nm LEDs, so a value of  $E_{e\ 850\ \text{nm}} = 119\ \text{W/m}^2$  was fixed, and the irradiance of 740 nm LEDs was set to  $E_{e\ 740\ \text{nm}} = 105.8\ \text{W/m}^2$  to reach the total irradiance required.

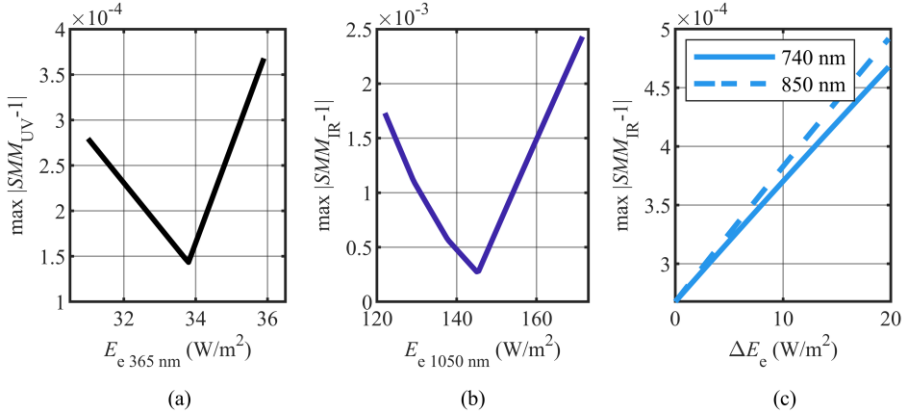


Fig. 59. (a) Spectral mismatch error of UV-side dependence on irradiance of 365 nm LEDs during step 1 (selected  $E_{e\ 365\ \text{nm}} = 33.8\ \text{W/m}^2$ ), (b) spectral mismatch error of IR-side dependence on irradiance of 1050 nm LEDs during step 2 (selected  $E_{e\ 1050\ \text{nm}} = 145.2\ \text{W/m}^2$ ), and (c) spectral mismatch error of IR-side dependence on irradiance adjustment of red LEDs during step 3 (selected  $\Delta E_{e\ 740\ \text{nm}} = 10.0\ \text{W/m}^2$ ) [P2].

For the Hybrid simulator, starting with Hybrid<sub>A+min</sub> spectrum, the following steps were taken to optimize it for  $\mu\text{c-Si}$  solar cells (Fig. 60):

1. Adjustment of the irradiance from halogen lamps within the A+-class limits to lower  $SMM$  on both the UV and IR sides of the spectrum;
2. Adjustment (lowering) of the irradiance from cool white LED to fit in the A+-class limits in the third interval;
3. Adjustment (lowering) of the irradiance from 365 nm LEDs to improve the  $SMM$  on the UV side;
4. Matching the AM1.5G 1 Sun irradiance by lowering the optical power from 740 nm and 850 nm LEDs.

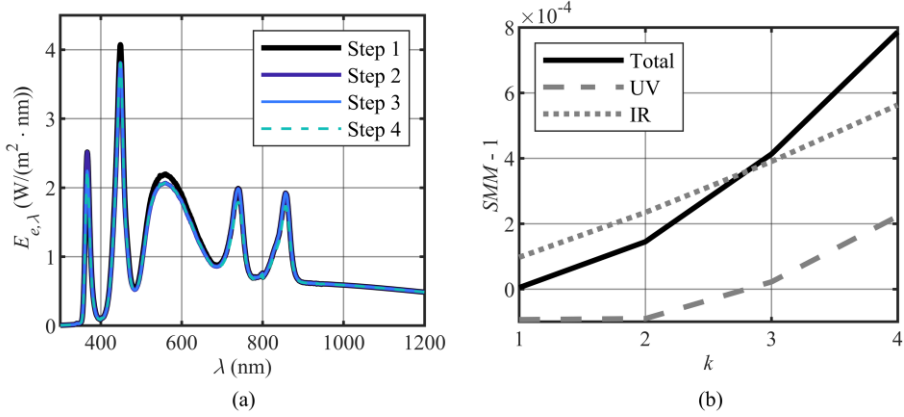


Fig. 60. Results of hybrid simulator optimization for  $\mu c$ -Si solar cells: (a) simulated spectra after each optimization step, (b) spectral mismatch error, as a function of dispersion multiplier  $k$  for final optimized spectrum with its UV and IR components [P2].

First, adjustment of halogen lamp irradiance up to the available maximum to fulfill A+-class irradiance requirements in the sixth interval to lower  $|SMM - 1|$  on the IR side (Fig. 61(a)) led to an irradiance value of  $E_{e \text{ Halogen}} = 377 \text{ W/m}^2$ , which was then fixed for the next step. Then, the irradiance of cool white LEDs was lowered to  $E_{e \text{ C.White}} = 339 \text{ W/m}^2$ , allowing the A+-class irradiation requirement to be met in the third interval (Fig. 61(b)).

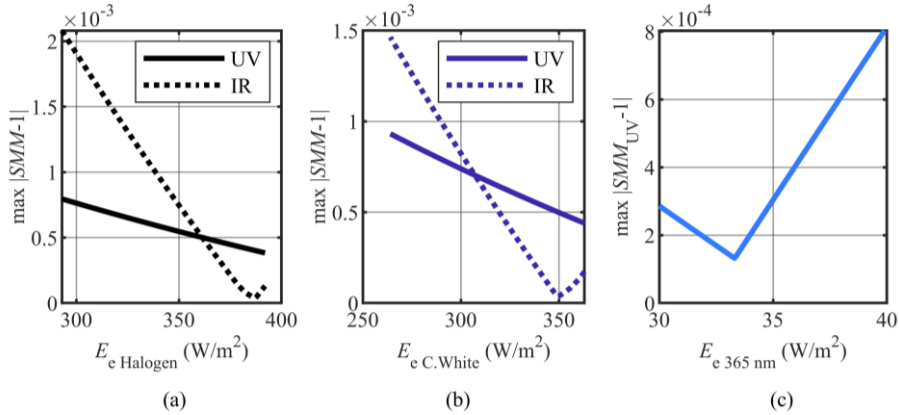


Fig. 61. (a) Spectral mismatch error dependence on irradiance of the halogen source during step 1 (selected  $E_{e \text{ Halogen}} = 377 \text{ W/m}^2$ ), (b) spectral mismatch error dependence on irradiance of the cool white source during step 2 (selected  $E_{e \text{ C.White}} = 339 \text{ W/m}^2$ ), and (c) spectral mismatch error of UV-side dependence on irradiance of 365 nm LEDs during step 3 (selected  $E_{e \text{ 365 nm}} = 33.3 \text{ W/m}^2$ ) [P2].

After fixing that value, additional adjustments to the irradiance of 365 nm LEDs were needed to correct  $|SMM - 1|$  on the UV side (Fig. 61(c)), thus fixing its value at  $E_{e\ 365\text{ nm}} = 33.3\text{ W/m}^2$ . Finally, the total excess of irradiance was subtracted equally from both red LEDs, leading to  $E_{e\ 740\text{ nm}} = 44.5\text{ W/m}^2$  and  $E_{e\ 850\text{ nm}} = 43.3\text{ W/m}^2$  irradiance values.

The optimization results demonstrate that different solar cell types require slightly different optimal spectra, because diverse bandgap energies and other structural differences result in varying utilization of distinct parts of the irradiance spectrum. When comparing LED-only configurations of simulators, higher optimal irradiance from 365 nm LEDs and lower optimal irradiance from 740 nm LEDs can be noticed in the case of  $\mu\text{c-Si}$  solar cells compared to CdTe cells. A similar pattern can also be seen with hybrid solar simulators. However, the required irradiance differences are of the order of tens of  $\text{W/m}^2$  only, as seen from Table 9 and Table 10. Therefore, the same set of light sources can be adaptable to both types of solar cells.

Table 10. Properties of LED-only L5 and hybrid H5 simulator configurations for  $\mu\text{c-Si}$  technology.

Source type	$E_{e,\lambda,\text{int}}\text{ (W/(m}^2 \cdot \text{nm))}$						TOTAL $E_e$ (W/(m <sup>2</sup> nm))
	365 nm	C.White	740 nm	850 nm	1050 nm	Halo	
L5	33.8	432.4	105.75	119	145.2		<b>836.1</b>
H5	33.3	339	43.5	43.3		377	<b>836.1</b>
Interval	$d_i\text{ (%)}$						<b>SID</b>
	1 <sup>st</sup>	2 <sup>nd</sup>	3 <sup>rd</sup>	4 <sup>th</sup>	5 <sup>th</sup>	6 <sup>th</sup>	
L5	11.83	-7.32	8.91	-4.66	-12.29	3.59	<b>12.29 %</b>
H5	-0.12	-12.15	12.46	-9.02	-3.64	12.49	<b>12.49 %</b>

For comparison purposes, spectral mismatch errors were also evaluated for two commercial Xenon solar simulators with spectral data tabulated in [157]. As with LED-based or hybrid solar simulators,  $SMM - 1$  was evaluated in three scenarios: when dispersion is assumed on both sides of the spectrum, when only on the UV side of the spectrum is considered, and when only the IR side is considered. The sums of these calculations are presented in Fig. 62. The largest  $SMM - 1$  moduli were obtained at  $k = 4$  in all cases. As can be seen when comparing with the LED-only and Hybrid simulator data, also presented in Fig. 62, substantially higher values were obtained in the case of a single Xe lamp, while higher values persisted, even with a modified lamp

spectrum. Therefore, the effects of spectrum mismatch should be less pronounced with the optimized simulators presented in this work.

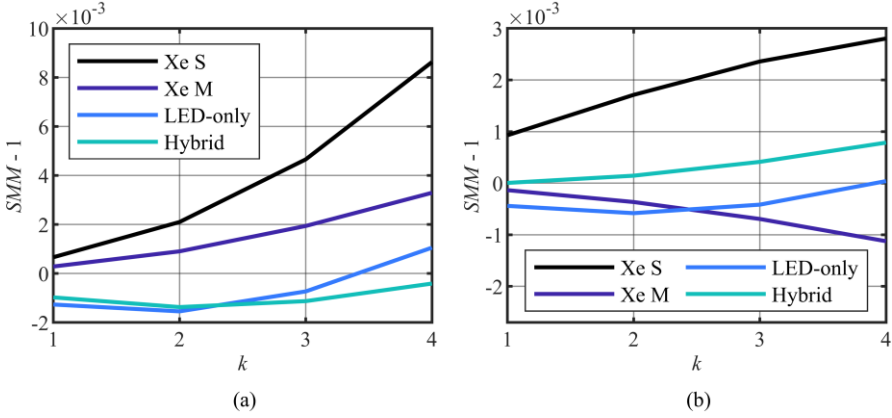


Fig. 62. Dependence of the spectrum mismatch error ( $SMM - 1$ ) on  $k$  for Aescusoft Sol Sim simulator spectra tabulated in [157]: (a) in the case of CdTe solar cells and (b) in the case of  $\mu c$ -Si solar cells. Letters “S” and “M” indicate single-Xe-lamp and modified-Xe-lamp configurations, respectively. Optimized LED-only and hybrid simulator cases are also shown for easier comparison.

### 3.4 Many light-source solution

The above-described optimizations have already led to  $d_i$  values fitting into A+ class requirements. With several additional adjustments,  $SID = 0$  can be achieved with the resulting H8 spectrum shown in Fig. 63. Low  $SMM - 1$  factors and other optimized features are also maintained in this eight-source configuration. Spectral coverage of  $SPC = 98\%$  is ensured due to a hybrid configuration with halogen emitters and a small contribution from 405 nm LED. This particular combination of 365 nm, 405 nm, and white LEDs allows for small values of  $SMM - 1$  in the UV range, while the combination of 1050 nm LEDs and halogen emitters possesses a similar feature in the IR range. The combination of white LEDs and halogen emitters provides all the power required in the third spectral interval, but then the addition of 523 nm LEDs becomes necessary for the second interval to maintain  $d_2 = 0$ . As with all previous configurations, 740 nm and 850 nm LEDs serve as light sources for the fourth and fifth intervals, respectively.

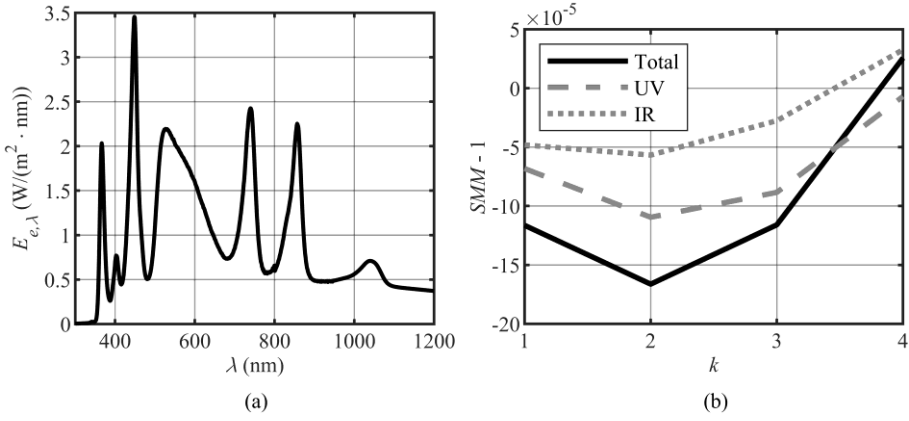


Fig. 63. (a) Simulated spectrum of hybrid H8 optimal ( $SID = 0$ ) simulator, and (b) spectral mismatch error, as a function of dispersion multiplier  $k$  for the spectrum with its UV and IR components for c-Si solar cell technology [P3].

Table 11. Properties of the hybrid H8 simulator configuration.

	$E_{e,\lambda_{\text{int}}}$ (W/(m <sup>2</sup> · nm))								TOTAL
Source type	365 nm	405 nm	Cool White	523 nm	740 nm	850 nm	1050 nm	Halo	$E_e$ (W/(m <sup>2</sup> nm))
H8	30	14	309	73	69	80	20	375	836.1
	$d_i$ (%)								
Interval	1 <sup>st</sup>	2 <sup>nd</sup>	3 <sup>rd</sup>	4 <sup>th</sup>	5 <sup>th</sup>	6 <sup>th</sup>		<i>SID</i>	
H8	0	0	0	0	0	0		0 %	

### 3.5 Simultaneous optimization for multiple solar cell types

Fine-tuning narrow band LEDs like 365 nm and 1050 nm ones has proven useful for minimizing spectral mismatch when the edge slopes of spectral response are nearby or intersect the corresponding LED spectrum. Moreover, as mentioned earlier, the irradiation of light sources with spectra further from the slopes has little to no influence on the spectral mismatch (Fig. 64). Therefore, 740 nm and 850 nm LEDs in L6 and H5 spectra were adjusted to potentially incorporate a simultaneously low  $SMM$  option for a-Si solar cell technology (Fig. 65 and Fig. 66 accordingly).

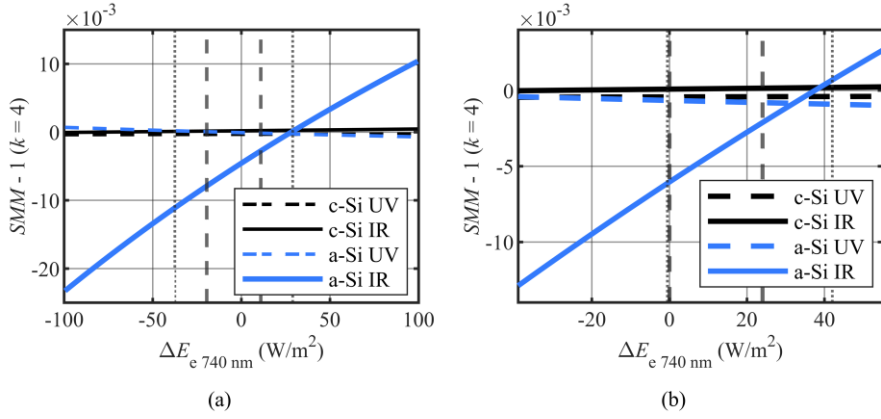


Fig. 64. Contribution of the UV and IR parts to spectral mismatch error (at  $k = 4$ ) as a function of the 740 nm LED's irradiance exchange with 850 nm LED in (a) LED-only L6 and (b) Hybrid H5 simulators. Vertical dashed lines correspond to the irradiance range where the A+ class is achieved, vertical dotted lines – the A class [P3].

For this simulation, the 740 nm LED's irradiance was adjusted together with the irradiance of 850 nm LEDs while monitoring spectral mismatch and keeping the total irradiance constant. It has been determined that in both cases, spectral mismatch for c-Si technology depends weakly on the irradiance of adjusted LEDs, while adding irradiance from 740 nm LEDs (taking away from 850 nm ones) results in smaller  $SMM - 1$  for a-Si solar cells.

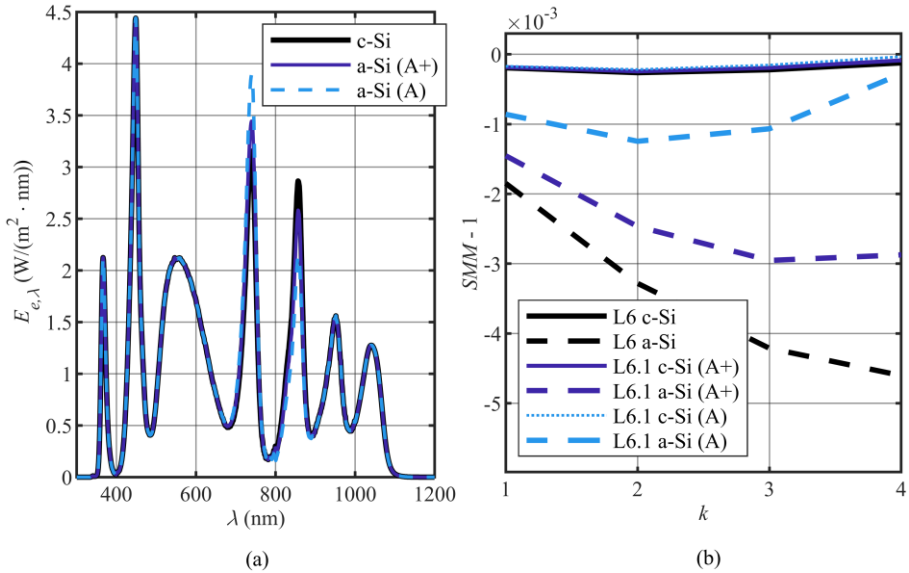


Fig. 65. (a) Spectra of the original and a-Si-optimized L6 simulators, and (b) the total spectral mismatch error, as a function of dispersion multiplier  $k$  [P3].



In the case of the LED-only simulator, by adding 11 W/m<sup>2</sup> from 740 nm LEDs, it is possible to lower the IR contribution of  $SMM - 1$  (at  $k = 4$ ) substantially, as can be seen in (Fig. 65(b)) while still achieving a class A+ spectrum. Moreover, allowing class A spectrum allows for an order of magnitude reduction of  $SMM - 1$  by adding 17 W/m<sup>2</sup> more irradiance.

A similar situation can be found in the case of a hybrid solar simulator. Adding 24 W/m<sup>2</sup> to the irradiance of 740 nm LEDs substantially lowers  $SMM - 1$  while still achieving a class A+ spectrum. Additional 13.5 W/m<sup>2</sup> can diminish  $SMM - 1$  further by more than an order of magnitude, however, only A-class spectrum is obtained in this case (Fig. 66(b)).

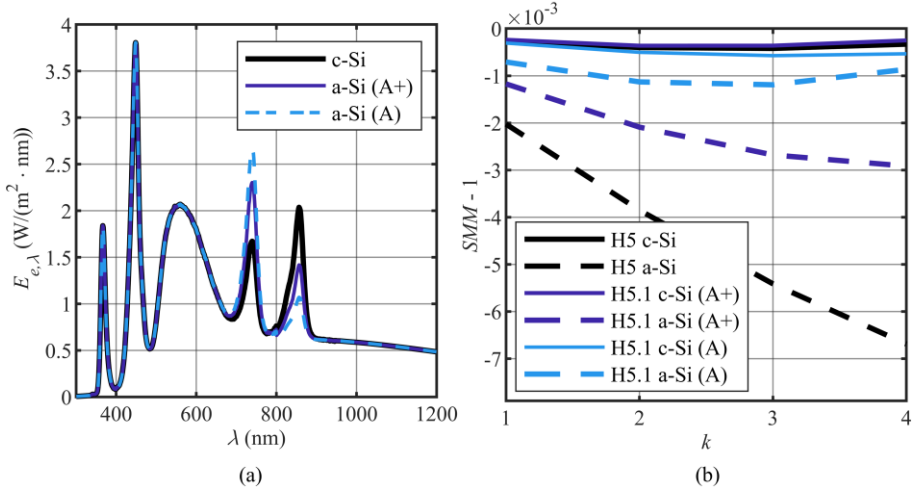


Fig. 66. (a) Spectra of the original and a-Si-optimized H5 simulators, and (b) dependence of the total spectral mismatch error on  $k$  [P3].

These results confirm the advantages of fine-tuning narrow-band LEDs for more universal simulator spectra in the context of different solar cell technologies; nevertheless, compromising spectral deviation can sometimes give even better outcomes.

### 3.6 Solar cell response simulations

Using TCAD software, various  $j$ - $V$  curves have been calculated for Al-BSF c-Si solar cell under the illumination of above discussed spectra.

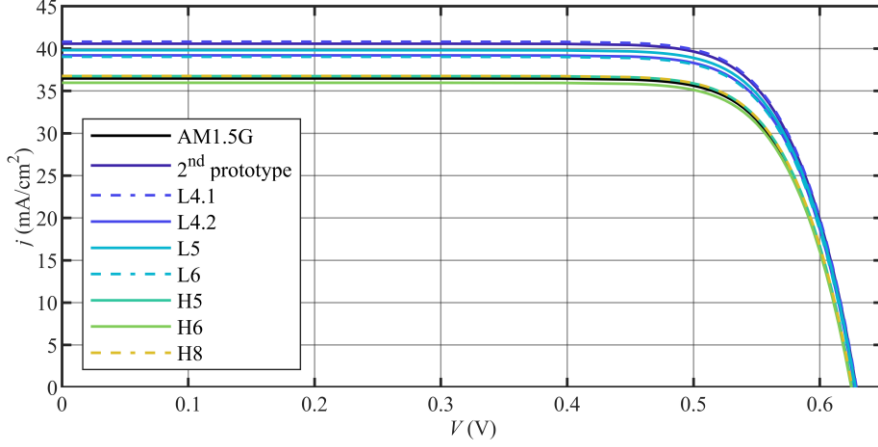


Fig. 67. Simulated  $j$ - $V$  curves for various illumination spectra for Al-BSF c-Si technology [P3].

For the AM1.5G spectrum, values of  $V_{OC} = 0.629$  V and  $j_{SC} = 36.5$  mA/cm<sup>2</sup> are obtained. Up to 12 % higher  $j_{SC}$  values are obtained for all spectra of LED-only simulators presented in Fig. 67. The complete spectra of these solar simulators fit within the high  $EQE$  region between 400 nm and 1000 nm, thus leading to excess photocurrent at the same integrated irradiance level. At the same time, only  $V_{OC}$  differences of the order of 1 mV are obtained.

Applying hybrid irradiation with halogen emitters leads to much closer photocurrent values of  $j_{SC} = 36.7$  mA/cm<sup>2</sup> for H5 and  $j_{SC} = 36.0$  mA/cm<sup>2</sup> for H6 simulator configurations. This effect may be attributed to a better approximation of the AM1.5G spectrum in the 1000 nm to 1200 nm range, where gradual reduction of  $EQE$  occurs. Again, the values  $V_{OC} = 0.625$  V and  $V_{OC} = 0.626$  V remain close to those obtained with AM1.5G irradiance. Strictly enforced values  $d_i = 0$  in the case of the H8 spectrum do not lead to any additional significant changes, with  $j_{SC} = 36.8$  mA/cm<sup>2</sup> and  $V_{OC} = 0.627$  V values obtained.

PC3D software was used to simulate sensitivity to the spectral mismatch effects ( $uSMM$ ) in silicon solar cells in Al-BSF, PERC, and IBC configurations. Five parameters were varied in the vicinity of the default values to obtain distinct  $EQE$  spectra that resemble batches of cells of the same technology with diverse specifications. These parameters were: front surface recombination currents (simulating emitter doping concentration), absorber doping concentration, thickness of the absorptive layer, and minority or majority carrier lifetimes in the base. After acquiring the  $EQE$  spectra, spectral mismatch errors ( $SMM - 1$ ) in comparison with the typical device, and the sensitivity to the spectral mismatch errors ( $uSMM$ ), as specified in the standard, were calculated.

### 3.6.1 Surface recombination currents

First, batches of solar cells with surface recombination current, ranging in values of (1 – 1000)  $fA/cm^2$ , were simulated.

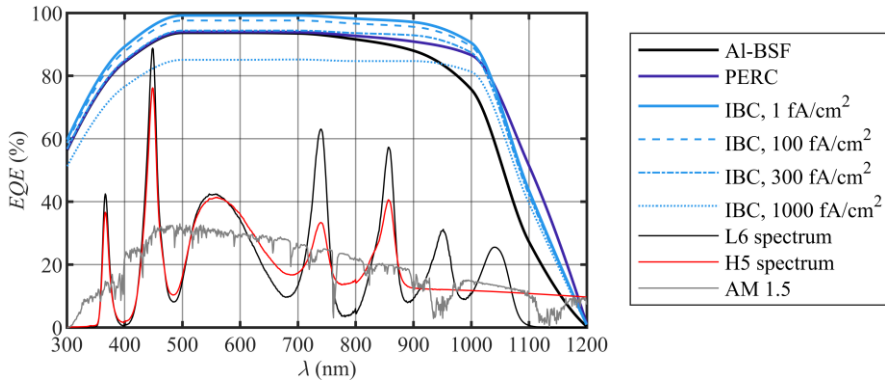


Fig. 68.  $EQE$  spectra of simulated Al-BSF, PERC, and IBC solar cells with different surface recombination current values.

**(L6, H5, and AM1.5 spectra in this and all following figures are given for wavelength-wise reference only)**

It has been established that for Al-BSF and PERC cells, surface recombination does not influence  $EQE$  (Fig. 68). For IBC cell, starting at 100  $fA/cm^2$ ,  $EQE$  begins to drop throughout the whole spectrum, achieving at most 85 % at 1000  $fA/cm^2$  currents, because in IBC cells most of generation happens in the front surface, while the entire collection of both types of charge carriers – at the back surface.

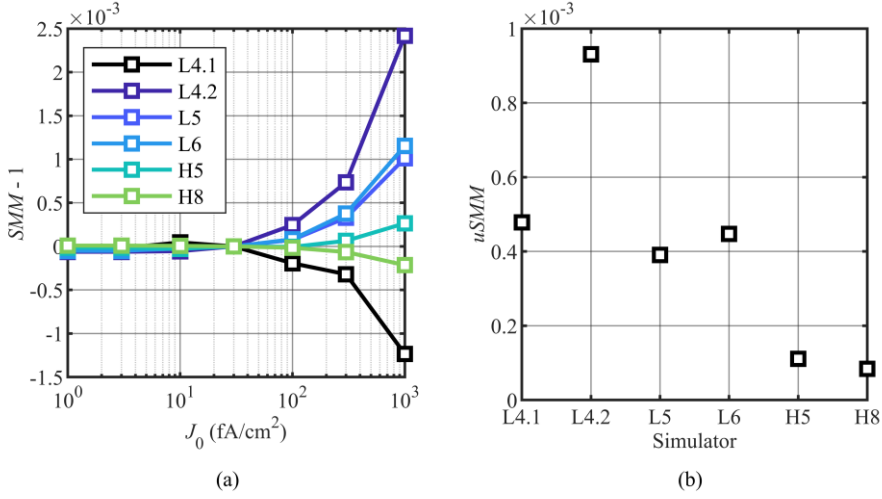


Fig. 69. (a) Spectral mismatch error ( $SMM - 1$ ) as a function of surface recombination currents and (b) sensitivity to the spectral mismatch effects for various illumination spectra on the IBC cell.

No spectral mismatch effects are seen for Al-BSF and PERC solar cells, in the context of varying surface recombination. In the case of IBC technology, spectral mismatch is negligible for lower values and increases with growing surface recombination currents (Fig. 69(a)), as the *EQE* spectrum gradually diminishes. Improvement of sensitivity to spectral mismatch effects with simulator spectrum iterations can be seen, with the exception of the L4.1 simulator (Fig. 69(b)), displaying similar sensitivity to L5 and L6. That can be attributed to the lack of irradiance on the corners of the spectrum, thus, little to no change to spectral mismatch is presented, resulting in a more minor deviation. Still, this spectrum has earlier been deduced as not optimal because of the lack of exactly those wavelengths. However, in novel solar cells recombination currents tend to be in the orders of ( $10^0 - 10^1$ ) fA/cm<sup>2</sup> and trend to go lower in the future [158], thus meaning that in real devices, including IBC cells, emitter doping concentration also practically does not influence *EQE* and is not to be considered in spectral mismatch context.

### 3.6.2 Al-BSF solar cell

Other parameters are quite more influential on *EQE* spectra and spectral mismatch effects. Batches of Al-BSF solar cells with a *p*-type multi-crystal Si absorptive layer were simulated. Default cell parameters, which later would be varied, were: doping concentration  $N_p = 7 \cdot 10^{15} \text{ cm}^{-3}$ ; wafer thickness  $h = 180 \text{ }\mu\text{m}$ ; minority carrier recombination time in bulk  $\tau_n = 30 \text{ }\mu\text{s}$ ; majority carrier recombination time in bulk  $\tau_p = 300 \text{ }\mu\text{s}$ .

First, simulation of varying base doping concentration, ranging in  $(7 \cdot 10^{14} - 7 \cdot 10^{16}) \text{ cm}^{-3}$  values, was made (Fig. 70).

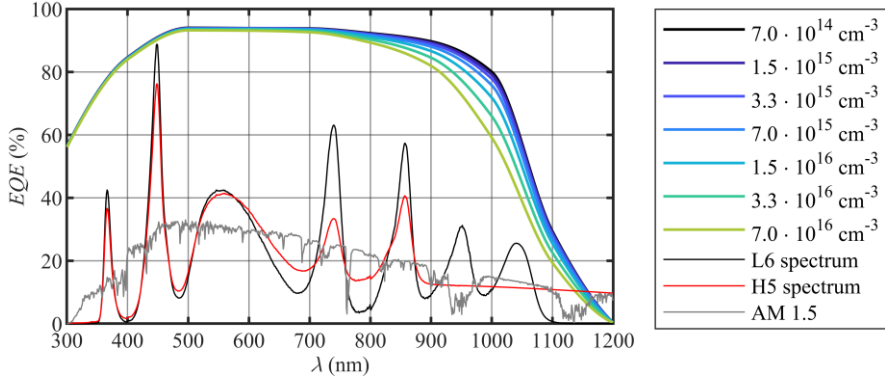


Fig. 70. *EQE spectra of simulated Al-BSF solar cells with different base p-doping concentrations.*

Increasing hole doping concentration slightly lowers *EQE* throughout the whole spectrum, but more importantly, it gradually lowers it on the IR side because of the decreasing minority carrier diffusion length in the base.

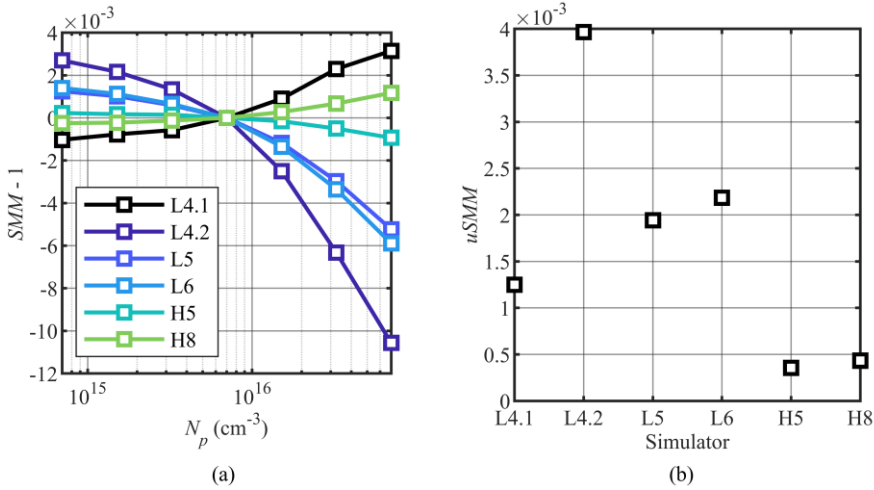


Fig. 71. (a) *Spectral mismatch error ( $SMM - 1$ ) as a function of doping concentration and (b) sensitivity to the spectral mismatch effects for various illumination spectra on the Al-BSF cell.*

Main changes of the *EQE* spectrum are happening in the 850 – 1100 nm region and *EQE* diminishes greatly but evenly at around 1050 nm, that is why spectral mismatch for almost all simulator spectra experience one-way gradual change (Fig 71), with: L4.2, L5 and L6 spectra deviating the most (because they include a discrete 1050 nm LED); H5 and H8 deviating the least (because

they contain continuous illumination in this range) and L4.1 deviating less than L5 or L6 (because it does not include 1050 nm LED, Fig. 44) .

Simulation of varying absorptive layer thickness, ranging in (120 – 240)  $\mu\text{m}$  values, was made (Fig. 72).

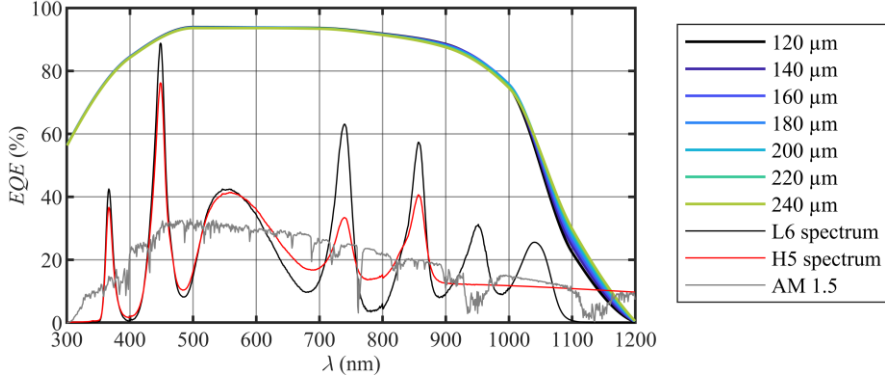


Fig. 72. *EQE spectra of simulated Al-BSF solar cells with different absorptive layer thickness.*

The growing thickness of the absorptive layer expands the *EQE* spectrum to the IR side, as the maximum absorption depth for the photons with energy close to the bandgap energy is being reached.

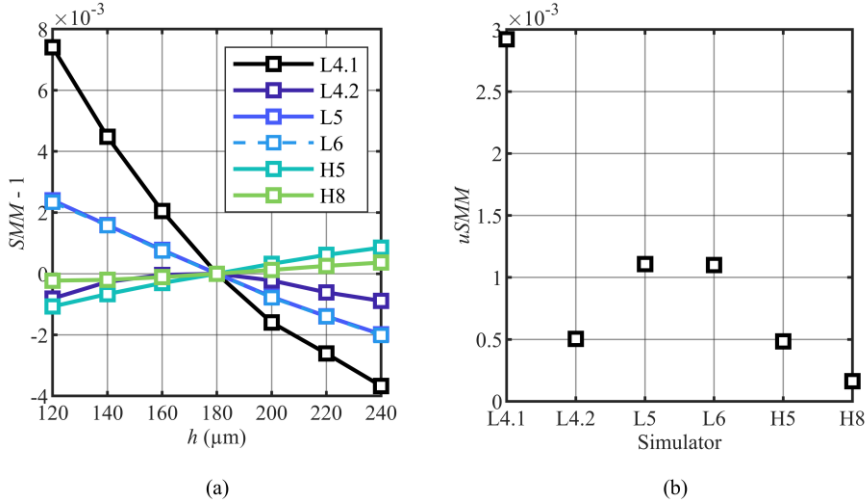


Fig. 73. (a) *Spectral mismatch error (SMM – 1) as a function of absorptive layer thickness and (b) sensitivity to the spectral mismatch effects for various illumination spectra on Al-BSF cell.*

As the IR edge of the *EQE* spectrum moves towards longer wavelengths, L4.1 spectrum results in the greatest spectral mismatch deviation (Fig. 73(a)), because, while the available absorption spectrum expands, no additional

irradiance is being provided. Meanwhile, L4.2 contains 1050 nm LED – the wavelength, around which the greatest development is experienced, thus showing one of the least spectral mismatch deviations as well as sensitivity to the spectral mismatch effects (Fig. 73(b)). In this case, the sensitivity for L5 and L6 spectra is exactly the same, because they only differ by an additional UV LED, where no *EQE* changes happen, and hybrid spectra show the opposite sign of spectral mismatch deviations compared to the others, while being the least sensitive of all (Fig. 73(b)).

Simulation of varying lifetime of excess minority carriers (electrons), ranging in (3 – 300)  $\mu\text{s}$  values, was made (Fig. 74).

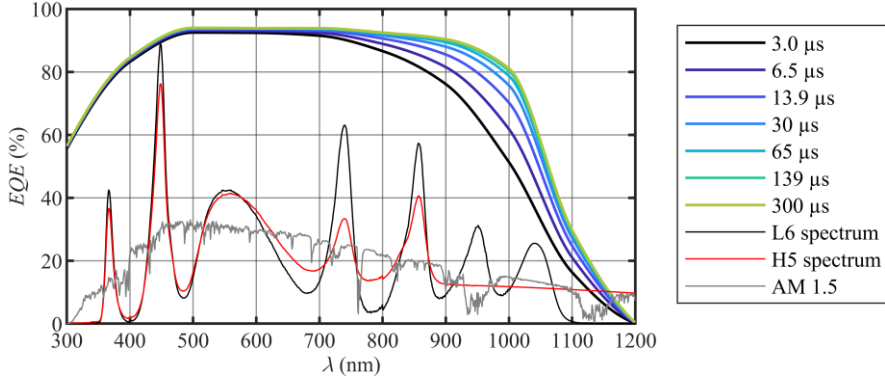


Fig. 74. *EQE spectra of simulated Al-BSF solar cells with different lifetimes of excess minority carriers.*

Longer lifetime of excess electrons, thus greater diffusion length of minority charge carriers, improves *EQE* at the IR side up to around 100  $\mu\text{s}$ . After that, the changes become negligible as the minority diffusion length becomes more than 3 times greater than the default base thickness ( $>550 \mu\text{m}$ ).

The saturation-like effects for spectral mismatch can be recognized in Fig. 75(a), as changes to the *EQE* spectrum become negligible. The trend of hybrid simulators being less sensitive to mismatch effects stays (Fig. 75(b)), while LED-only spectra hold similar sensitivity, as most changes of *EQE* happen between the wavelengths of 940 nm and 1050 nm LEDs, with yet again an exception of L4.1 simulator spectrum, because almost all variation of the *EQE* spectrum steadily moves out of this simulator's illumination spectrum.

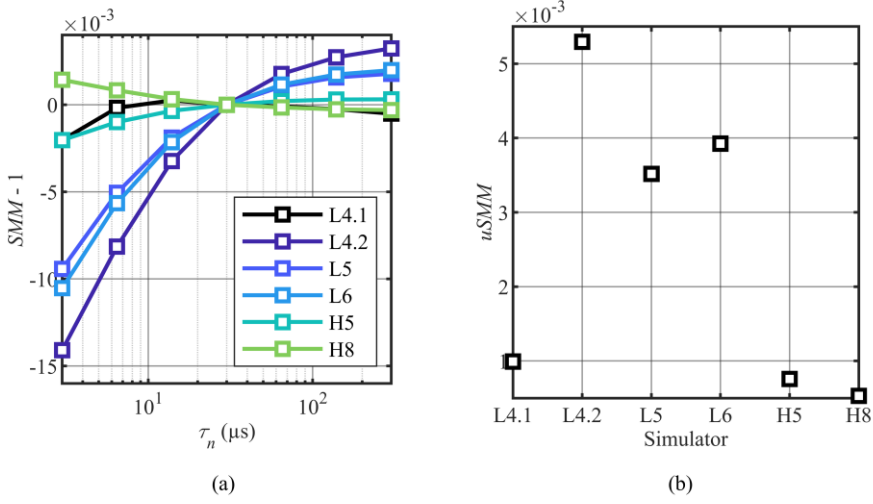


Fig. 75. (a) Spectral mismatch error ( $SMM - 1$ ) as a function of excess minority carrier lifetime and (b) sensitivity to the spectral mismatch effects for various illumination spectra on the Al-BSF cell.

Simulation of varying lifetime of excess majority carriers (holes), ranging in  $(1 - 1000) \mu s$  values, was made, and throughout the whole range practically no influence on  $EQE$  of the device was found. Therefore, spectral mismatch and sensitivity to the spectral mismatch effects are negligible.

All in all, as Fig. 76 shows, varying minority carrier lifetime has the most influence on the sensitivity to the spectral mismatch effect in Al-BSF cells, at least while ranging in  $(3 - 300) \mu s$  values. However, real-life minority carrier lifetime tends to stay in the  $(1 - 10) \mu s$  range [159], which would result in lower spectral mismatch. As a reminder, the physical variables ranged in the values of:  $N_p = 7 \cdot 10^{14} \text{ cm}^{-3} - 7 \cdot 10^{16} \text{ cm}^{-3}$ ;  $h = 120 \mu m - 240 \mu m$ ;  $\tau_n = 3 \mu s - 300 \mu s$ .

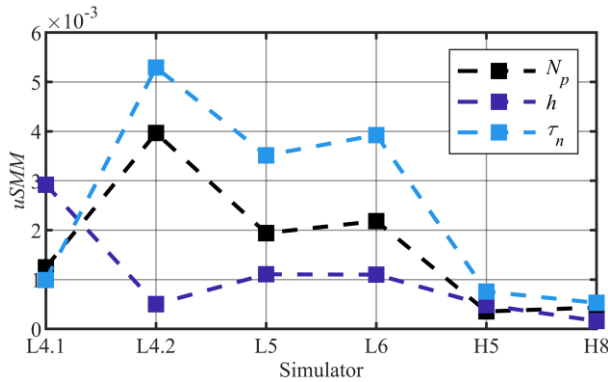


Fig. 76. Sensitivity to the spectral mismatch effects for various illumination spectra on the Al-BSF cell, in the case of different solar cell variables.



Also, while L5 and L6 spectra are not the best in absolute  $uSMM$  values all the time, L4.1 and L4.2 not only do not provide sufficient irradiation, but also their sensitivity values are less stable, imposing more complicated compensation of spectral mismatch effects for real-life measurements. Meanwhile, H5 and H8 simulators would be even less sensitive, mainly because most of the changes in  $EQE$  spectrum happen in the IR region, where broad-wavelength-range halogen lamps continually provide a great share of the irradiance.

Current-Voltage curves of Al-BSF solar cell, illuminated by various simulator spectra, were simulated (Fig. 77).

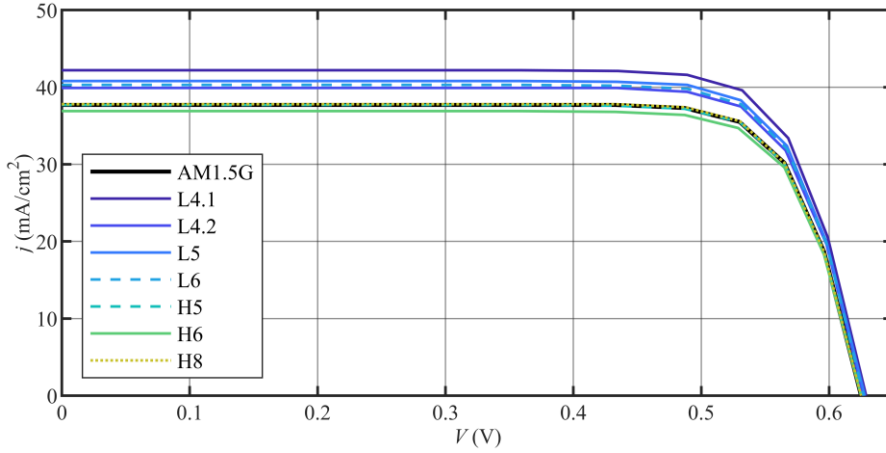


Fig. 77. Simulated  $j$ - $V$  curves for various illumination spectra for Al-BSF technology.

For AM1.5 G illumination spectrum, the values of  $V_{OC} = 0.625$  V and  $j_{SC} = 37.7$  mA/cm<sup>2</sup> are obtained. Although it is not an exact match, the  $j_{SC}$  and  $V_{OC}$  values correspond well with those simulated using TCAD software. Moreover, the basic trend of LED-only simulators generating excess photocurrent, H6 simulator generating too little photocurrent, and H5 with H8 simulators both matching the reference  $j$ - $V$  curve very closely (with no significant improvement in the H8 case). Also, all PC3D simulations result in 1.7 – 3.4 % greater  $j_{SC}$  values compared to TCAD ones for a similar device.

### 3.6.3 PERC solar cell

Batches of PERC solar cells with a  $p$ -type monocrystalline Si absorptive layer were simulated. Default cell parameters, which later would be varied, were: doping concentration  $N_p = 10^{16}$  cm<sup>-3</sup>; wafer thickness  $h = 180$  μm;

minority carrier recombination time in bulk  $\tau_n = 100 \mu\text{s}$ ; majority carrier recombination time in bulk  $\tau_p = 1 \text{ ms}$ .

First, simulation of varying base doping concentration, ranging in  $(10^{15} - 10^{17}) \text{ cm}^{-3}$  values, was made (Fig. 78).

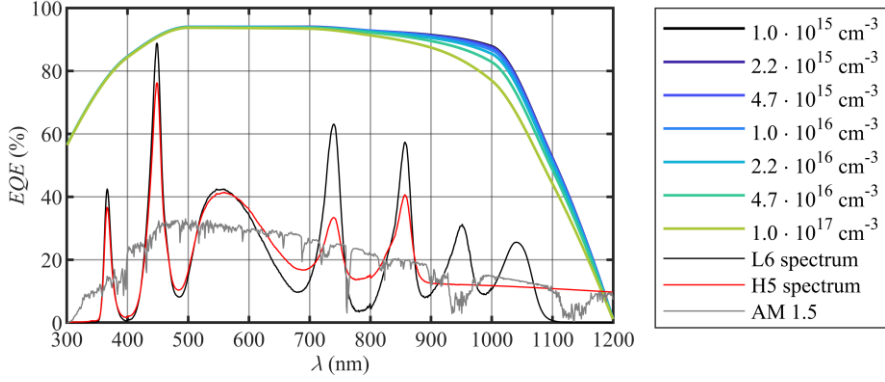


Fig. 78. EQE spectra of simulated PERC solar cells with different base p-doping concentrations.

Similar to the Al-BSF case, starting with around  $N_p = 10^{15} \text{ cm}^{-3}$ , increasing doping concentration gradually lowers EQE on the IR side because of decreasing minority carrier diffusion length in the base.

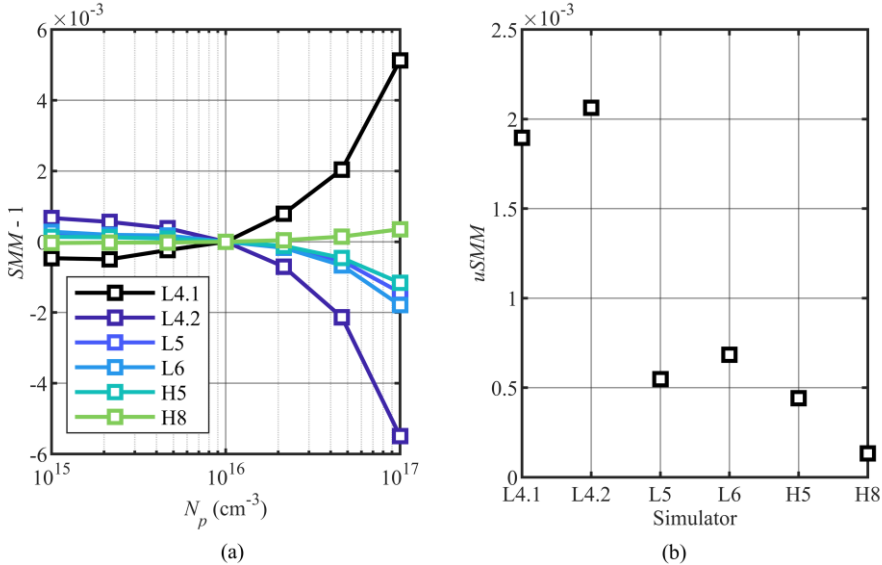


Fig. 79. (a) Spectral mismatch error ( $SMM - 1$ ) as a function of doping concentration and (b) sensitivity to the spectral mismatch effects for various illumination spectra on the PERC cell.

Similar to the Al-BSF case, spectral mismatch for all simulators steadily grows with increasing doping concentration, and the deviation increases more

rapidly from around  $N_p = 10^{16} \text{ cm}^{-3}$ , as the changes in  $EQE$  localize on the IR edge (Fig. 79(a)). Also, sensitivity to spectral mismatch effects is the greatest for the L4.1 and L4.2 simulators, followed by L5 and L6, because of irradiation changes at around 1050 nm LED wavelength (Fig. 79(b)). H5 and H8 are the least sensitive to spectral mismatch effects, because they contain continuous illumination in the range of the most significant  $EQE$  variance.

Simulation of varying absorptive layer thickness, ranging in (120 – 240)  $\mu\text{m}$  values, was made (Fig. 80).

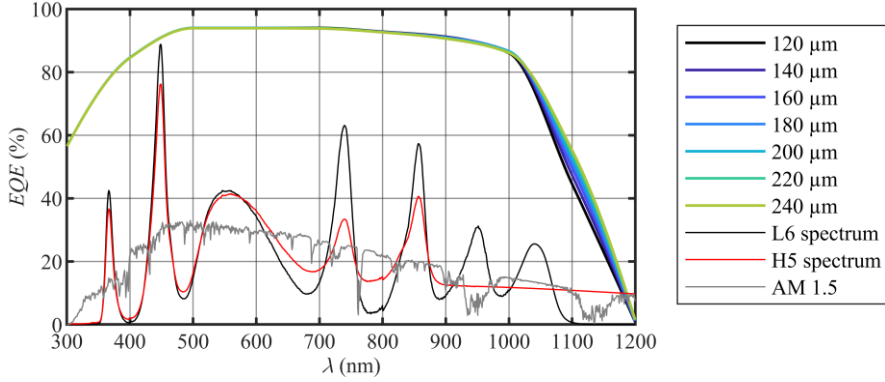


Fig. 80.  $EQE$  spectra of simulated PERC solar cells with different absorptive layer thickness.

As in Al-BSF technology, growing thickness of absorptive layer expands  $EQE$  spectrum to the IR side as the maximum absorption depth is being reached.

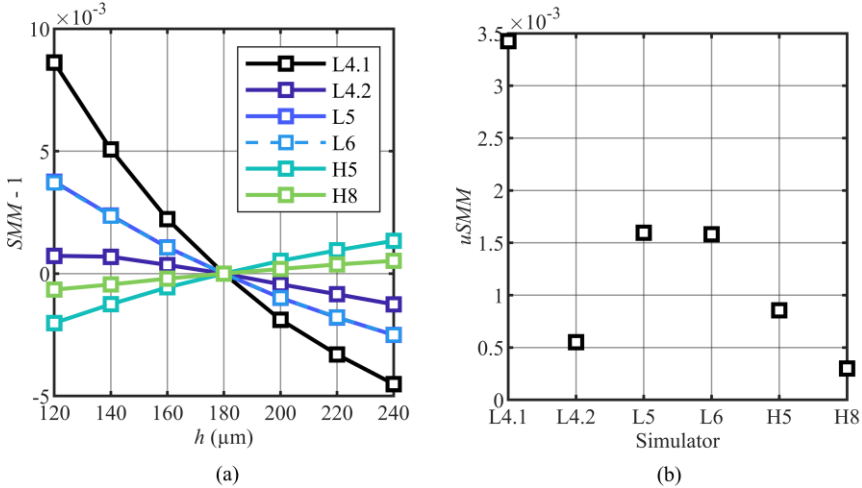


Fig. 81. (a) Spectral mismatch error ( $SMM - 1$ ) as a function of absorptive layer thickness and (b) sensitivity to the spectral mismatch effects for various illumination spectra on the PERC cell.

Similar to Al-BSF case, as the IR edge of the *EQE* spectrum moves towards longer wavelengths, L4.1 spectrum results in the greatest spectral mismatch deviation (Fig. 81(a)), because, while the available absorption spectrum expands, no additional irradiance is provided. Meanwhile, L4.2 contains 1050 nm LED – the wavelength, around which the greatest development is experienced, thus showing one of the least spectral mismatch deviations as well as sensitivity to the spectral mismatch effects (Fig. 81(b)). Also, while all of the values are higher compared to the Al-BSF case, the sensitivities for L5 and L6 spectra are basically the same, because they only differ by an additional UV LED, where no *EQE* changes happen, and hybrid spectra show the opposite sign of spectral mismatch deviations, with H8 being the least sensitive of all (Fig. 81(b)).

Yet again, well-defined improvement of sensitivity to spectral mismatch effects is achieved with each iteration of the solar simulator spectrum, beginning with the L5 simulator, where L6 enhances the UV side, and hybrid simulators employ wide-range sources on the IR side of the spectrum.

Simulation of varying lifetime of excess minority carriers (electrons), ranging in (10 – 1000)  $\mu\text{s}$  values, was made (Fig. 82).

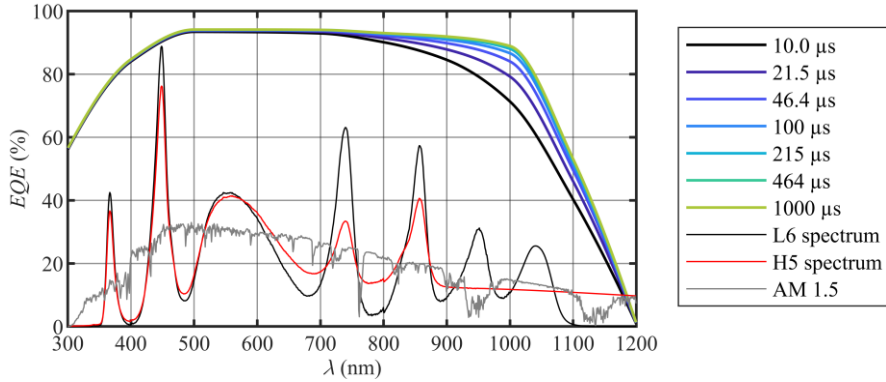


Fig. 82. *EQE* spectra of simulated PERC solar cells with different lifetimes of excess minority carriers.

Longer minority carrier lifetime, again, expands *EQE* in the IR region up until around 100  $\mu\text{s}$  while slightly enhancing *EQE* throughout the whole spectrum, as charge carriers generated by longer wavelengths gain a better chance to be collected.

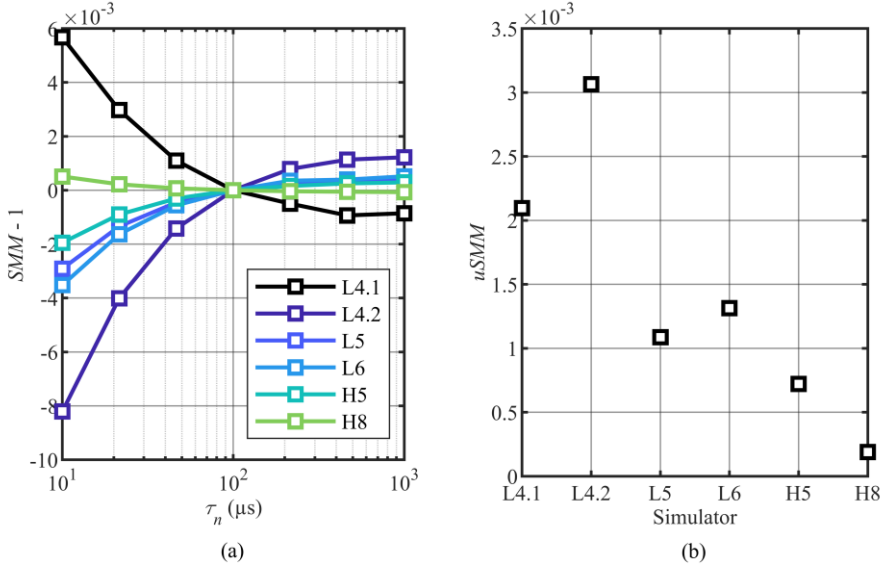


Fig. 83. (a) Spectral mismatch error ( $SMM - 1$ ) as a function of excess minority carrier lifetime and (b) sensitivity to the spectral mismatch effects for various illumination spectra on the PERC cell.

Similar to the Al-BSF case, the saturation-like effects for spectral mismatch errors can be recognized in Fig. 83(a), as changes to the *EQE* spectrum become negligible at large lifetimes. L4.2 spectrum appears the most sensitive (Fig. 83(b)), as *EQE* gains the most around 1050 nm wavelength LED, while L4.1 simulator spectrum deviates less, because almost all variation of the *EQE* spectrum steadily happens out of this simulator's spectral irradiance. Hybrid simulators show the least sensitivity, where H8 one reaches  $uSMM = 1.9 \cdot 10^{-4}$ .

Simulation of varying lifetime of excess majority carriers (holes), ranging in  $(1 - 1000) \mu s$  values, was made and it was determined that majority carrier lifetime does not influence *EQE* at all.

All in all, sensitivity to the spectral mismatch effects improves with each iteration of simulator spectrum (Fig. 84) with an exception on L4.2 spectrum in case of base thickness variation. As a reminder, the physical variables ranged in the values of:  $N_p = 10^{15} \text{ cm}^{-3} - 10^{17} \text{ cm}^{-3}$ ;  $h = 120 \mu m - 240 \mu m$ ;  $\tau_n = 10 \mu s - 1000 \mu s$ .

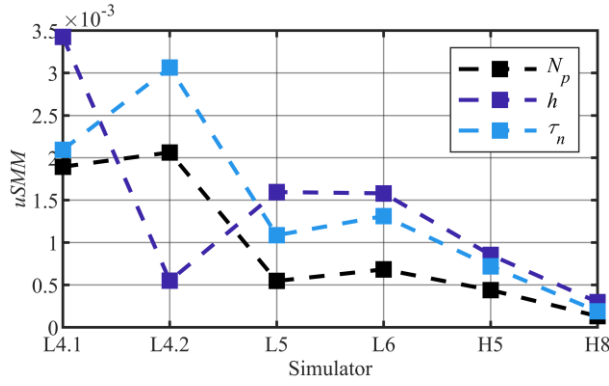


Fig. 84. Sensitivity to the spectral mismatch effects for various illumination spectra on the PERC cell, in the case of different solar cell variables.

H5 and H8 simulators would be even less sensitive, mainly because most of the changes in  $EQE$  spectrum happen in the IR region, where a broad-wavelength-range halogen lamp continually provides a predominant part of the irradiance. However, distinctively from the Al-BSF case, H8 stands out more because of the additional 1050 nm LED, providing illumination in the most turbulent region of the  $EQE$  spectrum.

Current-Voltage curves of PERC solar cell, illuminated by various simulator spectra, were simulated (Fig. 85). For AM1.5 G illumination spectrum, the values of  $V_{OC} = 0.662$  V and  $j_{SC} = 39.5$  mA/cm<sup>2</sup> are obtained.

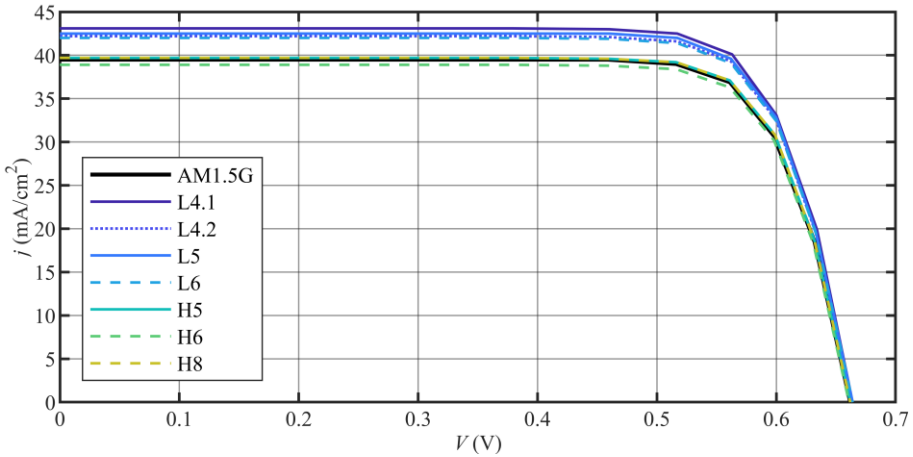


Fig. 85. Simulated  $j$ - $V$  curves for various illumination spectra for PERC technology.

The same trend can be seen, where LED-only simulators generate excess photocurrent, H6 simulator generates too little photocurrent, and the  $j$ - $V$  curves of H5 with H8 simulators are the closest to the reference, with no

significant improvement in the H8 case, although with a bit higher  $j_{sc} = 39.7 \text{ mA/cm}^2$  value.

### 3.6.4 IBC solar cell

Batches of IBC solar cells with an  $n$ -type monocrystalline Si absorptive layer were simulated. Default cell parameters, which later would be varied, were: doping concentration  $N_n = 10^{15} \text{ cm}^{-3}$ ; wafer thickness  $h = 140 \text{ }\mu\text{m}$ ; minority carrier recombination time in bulk  $\tau_p = 20 \text{ ms}$ ; majority carrier recombination time in bulk  $\tau_n = 2 \text{ ms}$ .

First, simulation of varying base doping concentration, ranging in  $(10^{14} - 10^{16}) \text{ cm}^{-3}$  values, was made (Fig. 86).

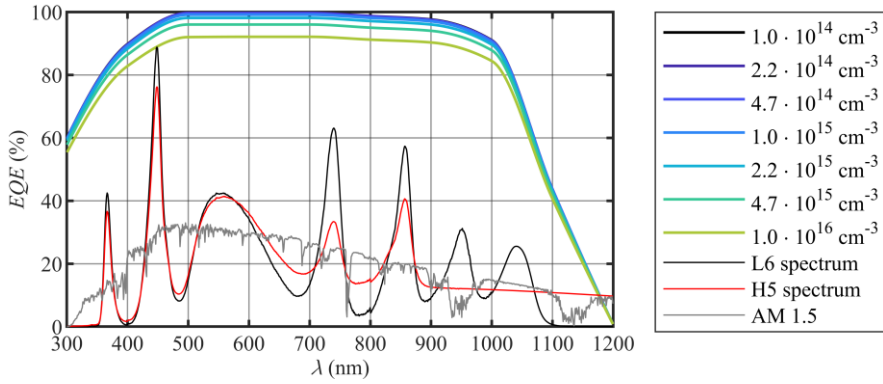


Fig. 86. *EQE spectra of simulated IBC solar cells with different base  $n$ -doping concentration.*

In contrast to Al-BSF and PERC cases, increasing base doping concentration steadily lowers  $EQE$  throughout the spectrum, notably accelerating at the  $N_n = 10^{15} \text{ cm}^{-3}$  value. This can be attributed to the increase of bulk recombination rate, leading to a decrease of photocurrent overpowering the built-in potential gains, as discussed by *O. Nichiporuk et al.* [160].

As the  $EQE$  changes take place throughout the whole spectrum, the spectral mismatch errors tend to be smaller by at least an order of magnitude, compared to Al-BSF and PERC technologies (Fig. 87(a)), with no distinct direction for all simulators. As a result, sensitivity to the mismatch effects is also at least an order of magnitude smaller, and a step-like improvement of sensitivity to spectral mismatch effects with each couple of simulators (L4.1 – L4.2, L5 – L6, H5 – H6) can be seen (Fig. 87(b)). Although real-life doping concentration should not exceed  $10^{15} \text{ cm}^{-3}$ , potentially resulting in even smaller sensitivity values.

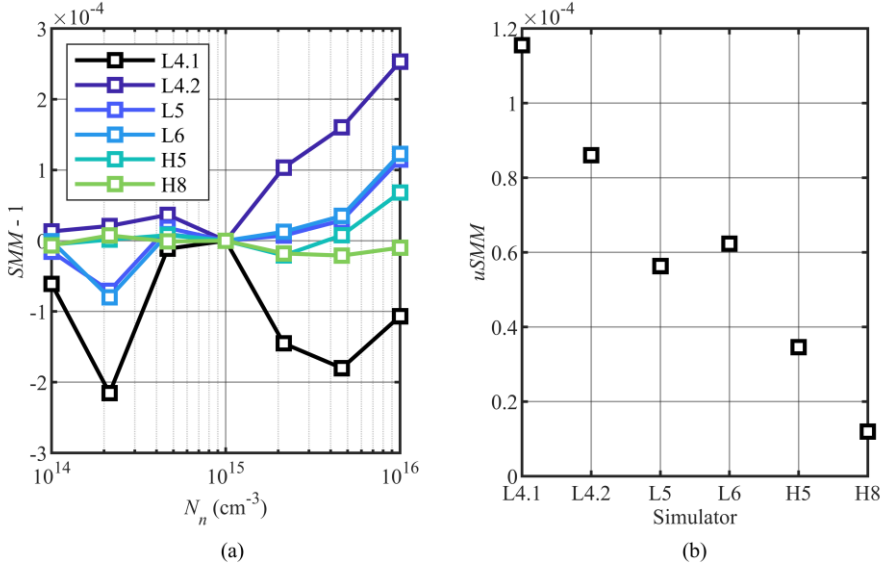


Fig. 87. (a) Spectral mismatch error ( $SMM - 1$ ) as a function of doping concentration and (b) sensitivity to the spectral mismatch effects for various illumination spectra on the IBC cell.

Simulation of varying absorptive layer thickness, ranging in ( $80 - 200$ )  $\mu\text{m}$  values, was made (Fig. 88).

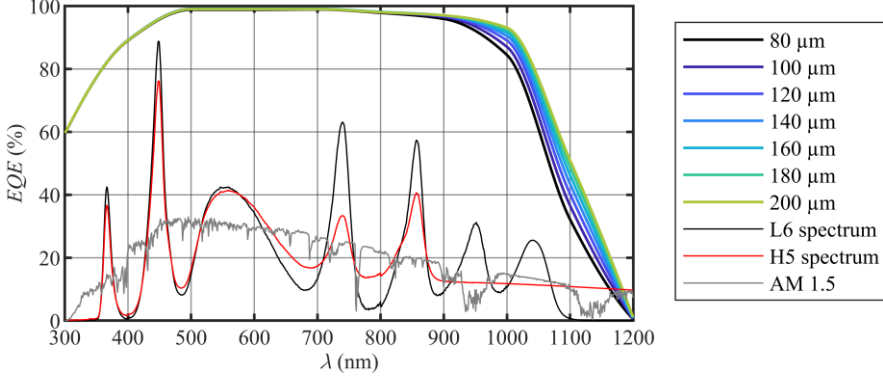


Fig. 88. EQE spectra of simulated IBC solar cells with different absorptive layer thickness

The growing thickness of the IBC absorptive layer also expands  $EQE$  to the IR side, and the wavelength where  $EQE$  begins to drop corresponds well with the absorption depth of silicon. Also, long lifetimes of charge carriers are presented in this PC3D example, ensuing collection of the carriers, generated at the front of a cell by shorter wavelength irradiation.



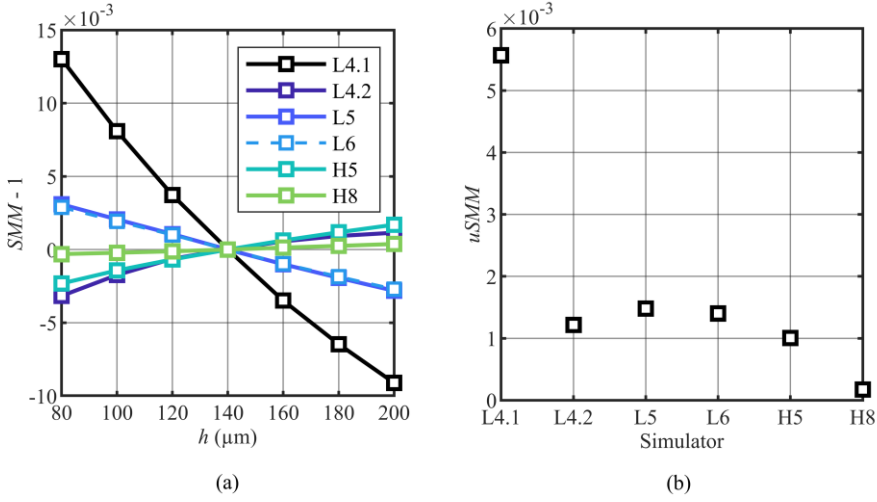


Fig. 89. (a) Spectral mismatch error ( $SMM - 1$ ) as a function of absorptive layer thickness and (b) sensitivity to the spectral mismatch effects for various illumination spectra on the IBC cell.

As the modeled thickness starts at  $80 \mu m$  with the IR edge of  $EQE$  already being at longer wavelengths than  $940 \text{ nm}$  LED, spectral mismatch of L4.1 simulator steadily goes down significantly with growing thickness (Fig. 89(a)). As a consequence, sensitivity to the spectral mismatch errors for L4.1 simulator is far greater compared to the others (Fig. 89(b)). Meanwhile, H8 ensures continuous spectral irradiance in the IR region, resulting in only  $uSMM = 1.7 \cdot 10^{-4}$  sensitivity.

Simulation of varying excess carrier recombination time in bulk was made. The nominal values of  $\tau_p = 20 \text{ ms}$  and  $\tau_n = 2 \text{ ms}$  are really high, converting to diffusion lengths considerably greater than device thickness. Also, varying one while leaving another at the default value does not change the  $EQE$  noticeably. While smaller fixed lifetime values could be chosen for both charge carriers to see more illustrative effects for IBC solar cells, in real life IBC devices excess carrier recombination time practically does not influence  $EQE$  and does not need to be considered in spectral mismatch context.

Overall, distinctively from the Al-BSF and PERC cases, the influence of wafer thickness on spectral mismatch effects is stronger compared to varying doping concentration (Fig. 90), as the latter affects  $EQE$  a lot more evenly throughout the whole spectrum. Meanwhile, in addition to majority carrier lifetime, minority carrier lifetime also does not influence  $EQE$ , as well as sensitivity to the spectral mismatch errors. As a reminder, the physical variables ranged in the values of:  $N_n = 10^{14} \text{ cm}^{-3} - 10^{16} \text{ cm}^{-3}$ ;  $h = 80 \mu m - 200 \mu m$ ;

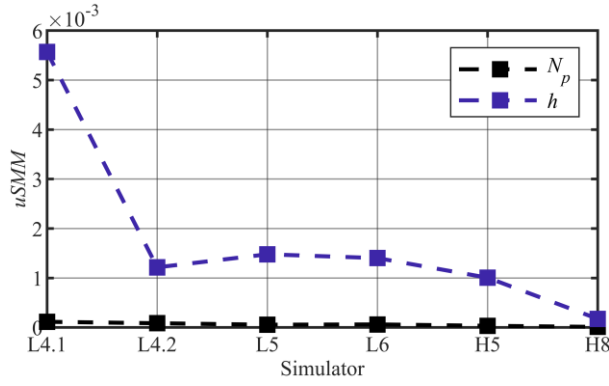


Fig. 90. Sensitivity to the spectral mismatch effects for various illumination spectra on the IBC cell, in the case of different solar cell variables.

Current-Voltage curves of IBC solar cell, illuminated by various simulator spectra, were simulated (Fig. 91). For AM1.5 G illumination spectrum, the values of  $V_{OC} = 0.681$  V and  $j_{SC} = 41.3$  mA/cm<sup>2</sup> are obtained.

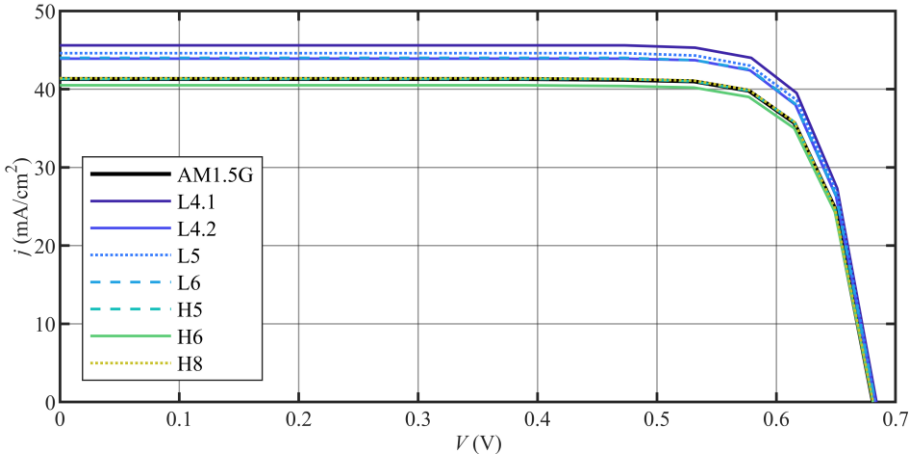


Fig. 91. Simulated  $j$ - $V$  curves for various illumination spectra for the IBC technology.

The same trend can be seen, where LED-only simulators generate excess photocurrent, H6 simulator generates too little photocurrent, and the  $j$ - $V$  curves of H5 with H8 simulators are the closest to the reference, although in the H8 case, a bit higher  $j_{SC} = 41.4$  mA/cm<sup>2</sup> value is obtained.

### 3.6.5 A comparison between different technologies

Fig. 92 and Fig. 93 compare the influence of the same varying solar cell parameter on the sensitivity of spectral mismatch effects for different silicon solar cell technologies.

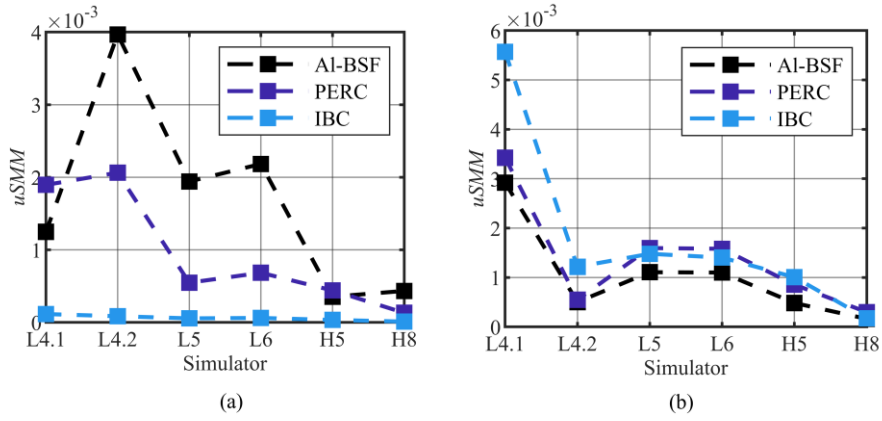


Fig. 92. Sensitivity to the spectral mismatch effects for distinct illumination spectra on different technology cells in the case of varying (a) base doping concentration and (b) base thickness.

While the absolute values differ, similar trends with each simulator iteration can be observed in each variable case:

- Simulators L5 and L6 provide similar sensitivity to spectral mismatch effects;
- Hybrid simulators are better than LED-only ones, spectral mismatch effect-wise, with H8 providing the least sensitivity;
- L4.2 simulator being the worst, except while varying base thickness, because spectral mismatch deviation changes direction as the IR edge of  $E_{QE}$  crosses 1050 nm wavelength, lowering the standard deviation of the data;
- The relative sensitivity to spectral mismatch effects of L4.1 simulator is the least predictable but proves to be the smallest LED-only one for many variables, mainly because the most significant developments of the  $E_{QE}$  happen outside simulators spectral irradiance.
- The lifetime of majority carriers influences external quantum efficiency far less than other variables. In case of IBC technology, the influence of both carrier lifetimes would be minimal and even negligible, as the lifetime values are usually found in the millisecond range.

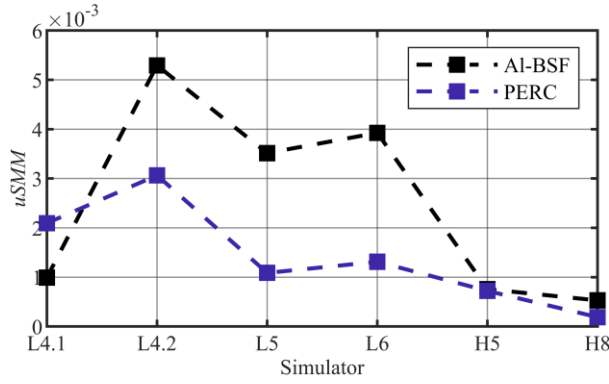


Fig. 93. Sensitivity to the spectral mismatch effects for distinct illumination spectra on different technology cells in the case of varying minority carrier lifetime.

Four different technologies were examined in a spectral mismatch context (Fig. 94). In addition to the three discussed before, PC3D provides a sample cell of the Back Point Contact (BPC) cell. The *EQE* of this cell is very similar to IBC, so it was not detailed previously. However, the standard requires at least four spectral responsivity data series to calculate spectral mismatch-related uncertainty.

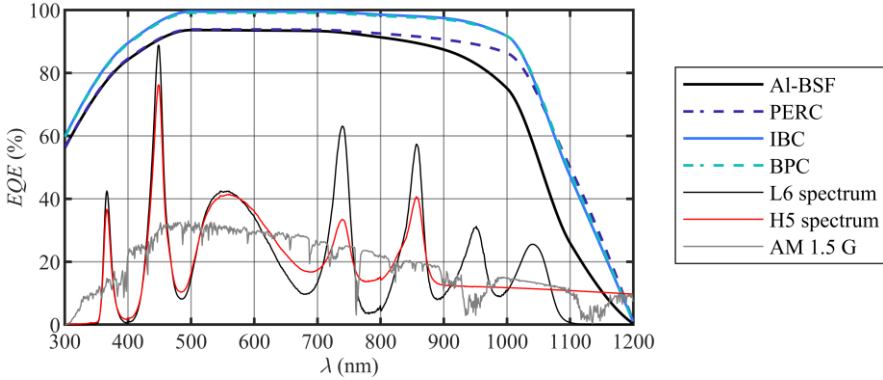


Fig. 94. *EQE* spectra of simulated solar cells with provided standard parameters.

The *EQE* spectrum of Al-BSF was defined as a reference, and spectral mismatch values for all simulators irradiating different technology cells were calculated (Fig. 95(a)).

There should be no particular trend in spectral mismatch ( $SMM - 1$ ) values, but the trend of improvement of spectral sensitivity with each simulator iteration can be seen (Fig. 95(b)), with the exception of H5 having a bit higher  $uSMM$  value compared to L5, L6 and H8 simulators, mainly because of the lack of irradiation around 1050 nm.

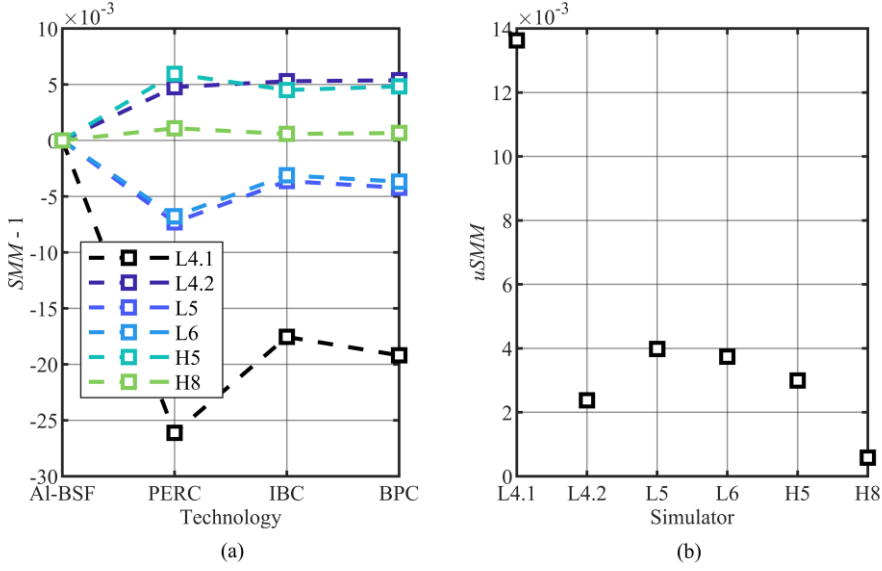


Fig. 95. (a) Spectral mismatch factor ( $SMM - 1$ ) with Al-BSF technology as a reference and (b) sensitivity to the spectral mismatch effects for various illumination spectra through all technologies. (All cell parameters used were standard, provided in PC3D).

Also, it should be noted that the order in which spectral responsivity data is compared (e.g., PERC – IBC vs. IBC – PERC), inverts the  $SMM$  value and ultimately changes the absolute  $uSMM$  values. Anyhow, the changes are not grand, and the trends for simulator iterations persist.

To sum it up, modeling solar cells with expansive but real-life parameters proves the usage of virtual spectral responsivities valuable, as the simulated hybrid, especially H8, spectra remain robust and stable to spectral mismatch effects. While not as consistently, steps for initial optimization of LED-only simulator spectra were also profitable, as L5 and L6 simulators seem to be more stable than L4.1 and L4.2 sensitivity-wise for modeled solar cells while also improving other spectral parameters.

### 3.7 Manufacturability of proposed designs

To evaluate the manufacturability of the proposed designs, we used the simulator presented in Fig. 37 as a starting point. Ample irradiance margins from cool white, 660 nm, 740 nm, 850 nm, and 940 nm LEDs would be readily available at 1-Sun irradiance in this design, since it was tested at approximately 1.4-Sun irradiance. Gray translucent shading in Fig. 96 indicates the area already occupied by these light sources.

Two additional 365 nm and 1050 nm LEDs were installed in positions indicated by the solid lines in the same sketch. Afterward, the induced photocurrent distribution in a sample plane was measured using a Thorlabs PM100D power meter with a compact Osram BPW34 photodiode mounted on motorized Standa 8MT195 and 8MT295 stages in XY configuration. We have repeated the measurements both with and without the individual reflectors. In addition, the irradiance at the maximum generated photocurrent point was measured using the Ophir PD300-UV-SH photodiode sensor.

The back plane of the simulator also potentially can have sufficient additional space for halogen lamp-based emitters of up to 51 mm reflector diameter. Full integration of these emitters with LED arrays has many technical challenges due to height differences of reflectors and increased thermal loads, which are already beyond the scope of this work. Nevertheless, an experiment with a halogen emitter and the same external reflector, (solid black external line in Fig. 96), allows us to estimate the achievable irradiance levels.

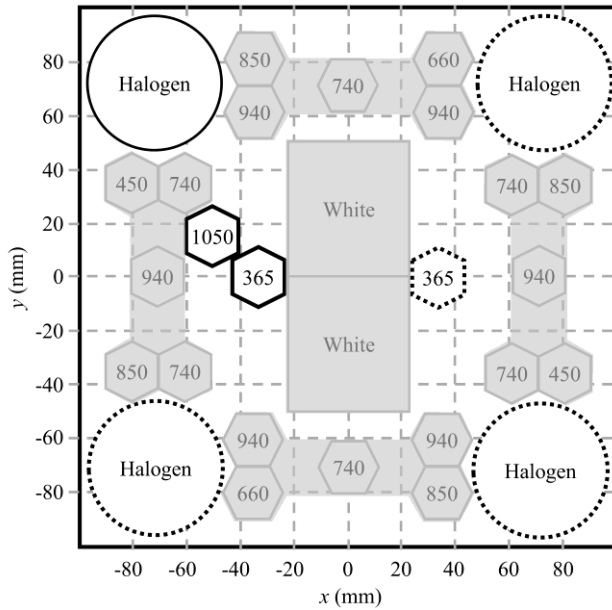


Fig. 96. Experimental design of a hybrid solar simulator. Gray translucent zones indicate the area already occupied by LEDs presented in Fig. 37, solid line borders indicate mounted and measured LEDs, and dotted lines indicate equal-irradiance symmetrically simulated LEDs.

We have repeated the measurements of the induced photocurrent distribution after installing an Osram DECOSTAR 51 ALU 35 W bulb instead of the LED array. In addition, photocurrent was measured using

Thorlabs FDS-1010-CAL photodiode at the maximum irradiance point. The influence of other sources indicated by a dashed line in Fig. 96 was accounted for by rotating the measured photocurrent distribution by either a  $90^\circ$  or  $180^\circ$  angle and adding up the results to obtain the photocurrent distribution data presented in Fig. 96.

When no individual reflectors are used, a relatively uniform distribution of the induced photocurrent is obtained with just two 365 nm LEDs, as seen in Fig. 97(a). Photocurrent values range from  $33.4 \mu\text{A}$  to  $36.0 \mu\text{A}$ , corresponding to  $23 \text{ W/m}^2$  to  $25 \text{ W/m}^2$  in the center part of the sample plane of  $160 \text{ mm} \times 160 \text{ mm}$ . Such irradiance is already close to the required one for optimum hybrid simulators and would already bring significant *SMM* – 1 reduction benefits in LED-only configurations. With 4 devices placed on both sides of the white LED arrays, the necessary irradiance in all optimal configurations would be achievable.

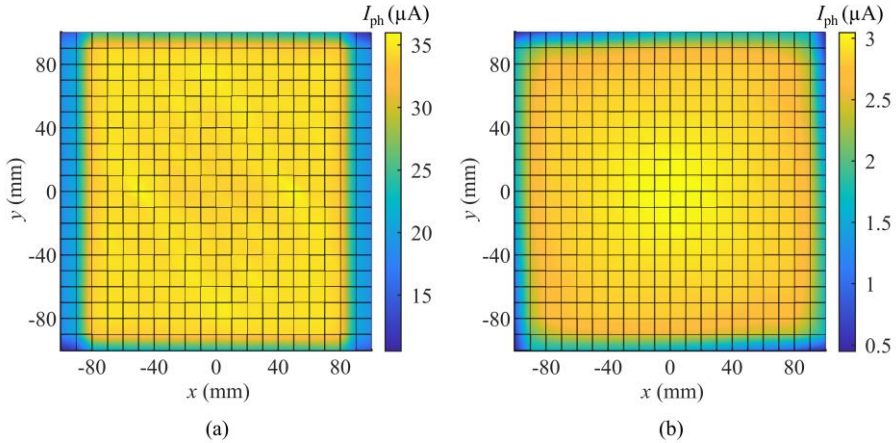


Fig. 97. (a) Simulated total irradiance distribution of two 365 nm LEDs and (b) simulated total irradiance distribution of four halogen light sources.

Photocurrent distribution for four 35 W halogen lamp emitters is shown in Fig. 97(b). A maximum photocurrent of 3.0 mA is obtained in the center of the sample plane. It drops to 2.9 mA near the edges of the  $80 \text{ mm} \times 80 \text{ mm}$  square area or 2.65 mA near the edges of the  $160 \text{ mm} \times 160 \text{ mm}$  square area. With just a single emitter, much less uniform distribution was obtained, and maximum photocurrents of 1.35 mA and 14.3 mA were recorded with Osram BPW34 and Thorlabs FDS-1010-CAL photodiodes, respectively. The maximum responsivity of the used FDS-1010-CAL photodiode is  $0.693 \text{ A/W}$  at 980 nm. Using this value for a very conservative estimation, it can be stated that irradiance exceeds  $307 \text{ W/m}^2$  in the center of the sample plane. Switching to 50 W halogen lamps of the same footprint would provide a further option

to increase the power by a factor of approximately 1.4. Therefore, it can be stated that the investigated spectrum optimization of hybrid solar simulators can potentially be achieved even within the existing footprint of already demonstrated solar simulators.

Maximum irradiance of  $14 \text{ W/m}^2$  was measured with an Ophir PD300-UV-SH photodiode sensor in the case of a 1050 nm LED with the individual reflector, and  $7.8 \text{ W/m}^2$  without it. These values are approximately an order of magnitude lower than those required for optimized LED-only simulators, demanding at least 10 LEDs of this type only. Therefore, either more powerful emitters or more comprehensive optimization of the layouts of LED arrays would be required to implement these simulators.

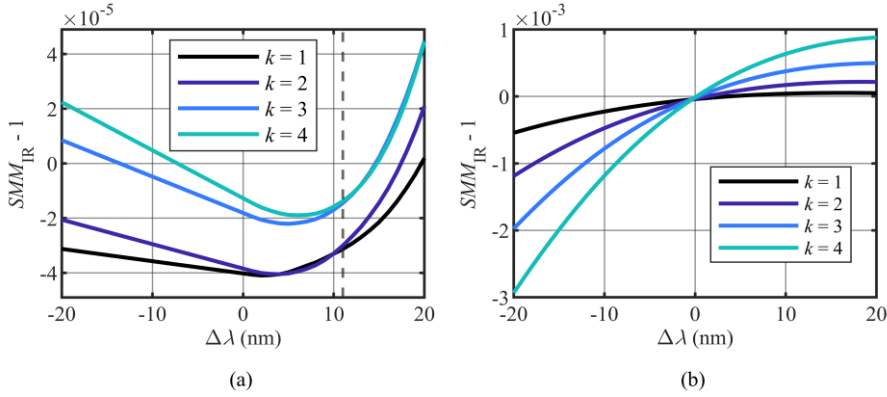


Fig. 98. Dependence of  $SMM-1$  factor on the peak wavelength shift  $\Delta\lambda$  in L5 configuration: (a) only emission spectrum of the 940 nm LED is varied, (b) only emission spectrum of the 1050 nm LED is varied. The vertical dashed line in panel (a) indicates the limit for the A+ class in the L5 configuration.

Emission wavelength variations can be expected when different batches of LEDs are used, or when different manufacturers produce devices for the same application. Dependence of  $SMM-1$  factor in L5 configuration on peak wavelength deviations  $\Delta\lambda$  of two LED devices is shown in Fig. 98. To obtain these results, peak wavelengths of 940 nm and 1050 nm LEDs were varied up to 20 nm. Modulus of  $SMM-1$  factor indeed increases due to these deviations. However, even with such relatively significant wavelength changes, L5 configuration retains a substantial advantage over unoptimized configurations L4.1 and L4.2, as can be seen when comparing with results of Fig. 47.



## 4 CONCLUDING STATEMENTS

1. Large white LED arrays and a mirror “box” application allow us to significantly increase the usable area compared to earlier works while maintaining a similar total number of LEDs. Twenty-two devices were used instead of nineteen, and an approximately six-fold area increase was achieved using a twofold electrical power increase compared to [3]. At the same time, the influence of homogenizing perimeter mirrors fully offsets the detrimental effects of concentrating white light sources in one device. The combination of individual reflectors with a common homogenizing mirror system allows reaching a  $14\text{ cm} \times 16\text{ cm}$  area illuminated according to AAA class requirements in the 400 nm – 1100 nm spectral range.

2. A+-class solar simulator spectra are achievable with only four types of LED sources: cool white, 740 nm, 850 nm, and 1050 nm. In comparison with the previous edition of the standard spectral intervals, redefinition plays a crucial role in this case, since the spectrum of cool white LEDs alone is sufficiently well-balanced to provide a compatible spectrum within A+-class specifications in the first three spectral intervals out of the required six. Our analysis and presented data show that careful adjustments of sources emitting near the responsivity spectrum's far red and/or IR edge can lead to  $SMM - 1$  parameter reduction. Spectral mismatch factors in the IR range can be reduced by more than one order of magnitude in the case of c-Si solar cells, if a carefully engineered combination of 940 nm and 1050 nm LEDs is used.

3. Adjustments of the irradiance from 740 nm LEDs have a more pronounced influence on spectral mismatch effects in the case of a-Si cells in comparison with c-Si cells. Such adjustments, however, might require switching from an A+-class spectrum to a nominally worse A-class spectrum. It should be noted that optimization challenges might be present at least in the case of CdTe solar cells; as our results demonstrate, minimization of  $SMM - 1$  deviation might lead to A-class classification of the spectrum. As our results indicate, the proposed designs of the spectra of solar simulators are expected to yield lower spectral mismatch errors than conventional Xe lamp-based simulators.

At present, there are no sufficiently powerful and efficient IR emitters of longer than 1000 nm wavelength; therefore, the use of halogen lamps for solar simulators can be a suitable compromise.

4. In the case of hybrid solar simulators with halogen lamp-based emitters included, a fifth type of light source is required for the first interval to achieve A+-class in spectral distribution, since the emission spectra of halogen lamps overlap with the emission spectra of cool white LEDs, resulting in need of reducing LED's irradiance. However, it should be noted, the configurations with halogen lamp-based emitters consistently possess much higher *SPC* values than LED-only configurations.

Even optimized for two solar cell types at a time, hybrid simulators possess much lower *SPD* compared to LED-only solar simulators, with the same number of distinct source types. A high *SPC* > 97 % is also obtained in all cases, further confirming the advantages of hybrid simulator configurations.

Even more importantly, using hybrid simulators of class A+ with just five or six different source types brings the photocurrent deviation to within 2% compared to the AM1.5G conditions for c-Si solar cells.

5. Adding UV emitters of 365 nm peak wavelength is beneficial for reducing spectral mismatch effects when testing all types of solar cells. This result applies to both the LED-only and hybrid simulator configurations, and the relevant irradiance is within the (25 – 43) W/m<sup>2</sup> range. This *SMM* – 1 parameter management factor effectively equalizes the number of light sources for both types of simulators.

A series of proof-of-concept experiments revealed that proposed optimized simulators can potentially be implemented within the same footprint as previous generation simulators by adding halogen lamp-based and 365 nm sources. However, more powerful 1050 nm LEDs or substantial optimizations of LED array layout are necessary for the LED-only configuration.

6. Numerical evaluations of spectral mismatch effects for simulated silicon solar cells while under optimized and in-progress illumination spectra were performed. After investigating Al-BSF, PERC and IBC solar cells with varying doping concentration, substrate thickness and carrier recombination parameters, it was deduced that the steps of optimization obtained with idealized spectral responsivity also hold with more sophisticated models of cells. The precise adjustments of target LEDs can lead to notably less sensitivity to varying physical properties between distinct devices or even different solar cell technologies. Also, hybrid simulators show the best robustness to spectral mismatch effects, with an 8-source, optimized spectral irradiance deviation (*SID* = 0 for all intervals), hybrid setup excelling in both spectral match and mismatch parameters as well as simulated short circuit current match with reference.

7. Three partially related future research directions can be envisaged based on the findings presented in this work. One is the simultaneous optimization of A+- class LED-based and hybrid solar simulators for multiple types of solar cells. The second is optimization, which considers more parameters of the solar cells, such as open-circuit voltage and maximum power of the solar cells. The third direction is a comprehensive evaluation of the expected uncertainties resulting from variations in the emission spectra of LEDs.

## 5 LIST OF REFERENCES

- [1] V. Esen, Ş. Sağlam, B. Oral, “Light sources of solar simulators for photovoltaic devices: A review,” *Renew. Sustain. Energy*, vol. 77, pp. 1240–1250, 2017, doi: 10.1016/j.rser.2017.03.062.
- [2] M. Bliss, T.R. Betts, R. Gottschalg, “An LED-based photovoltaic measurement system with variable spectrum and flash speed,” *Sol. Energy Mater. Sol. Cells*, vol. 93, pp. 825–830, 2009, doi: 10.1016/j.solmat.2008.09.056.
- [3] A. Novičkovas, A. Baguckis, A. Mekys, V. Tamošiūnas, “Compact light-emitting diode-based AAA class solar simulator: Design and application peculiarities,” *IEEE J. Photovolt.*, vol. 5, no. 4, pp. 1137–1142, Jul. 2015, doi: 10.1109/JPHOTOV.2015.2430013.
- [4] “Photovoltaic Devices - Part 9: Classification of Solar Simulator Characteristics,” *IEC 60904-9:2020, International Electrotechnical Commission, Geneva, Switzerland*, 2020.
- [5] “Statistical Review of World Energy 2024”, *Energy Institute*, 2024. ISSN 2976-7857, ISBN 978 1 78725 408 4.
- [6] G. Masson, E. Bosch, A. Van Rechem, M. de l’Epine, “Snapshot of Global PV Markets 2024,” *IEA Photovoltaic Power System Programme*, 2024, doi: 10.69766/VHRF4040.
- [7] “GISS Surface Temperature Analysis (v4)”, *NASA Goddard Institute for Space Studies*, 2025. [https://data.giss.nasa.gov/gistemp/graphs\\_v4/](https://data.giss.nasa.gov/gistemp/graphs_v4/) (last accessed in May 2025).
- [8] “Standard Tables for Reference Solar Spectral Irradiances: Direct Normal and Hemispherical on 37° Tilted Surface,” *ASTM G173-03, American Society for Testing and Materials, PA*, 2012, doi: 10.1520/G0173-03R12.
- [9] S. Rühle, “Tabulated values of the Shockley–Queisser limit for single junction solar cells,” *Solar Energy*, vol. 130, pp. 139–147, 2016, doi: 10.1016/j.solener.2016.02.015.
- [10] A. Nasir et al., “Beyond lead: Progress in stable and non-toxic lower-dimensional perovskites for high-performance photodetection,” *Sustainable Materials and Technologies*, vol. 38, 2023, doi: 10.1016/j.susmat.2023.e00759.
- [11] D. M. Chapin, C. S. Fuller, G. L. Pearson, “A New Silicon p-n Junction Photocell for Converting Solar Radiation into Electrical Power,” *J. Appl. Phys.*, vol. 25 (5): 676–677, May 1954, doi: 10.1063/1.1721711.
- [12] M. Telkes, “The Efficiency of Thermoelectric Generators,” *J. Appl. Phys.*, vol. 18 (12), pp. 1116–1127, 1947, doi: 10.1063/1.1697593.
- [13] S. Philipps, W. Warmuth, “Photovoltaics Report,” *Fraunhofer ISE*, Jul. 2024.
- [14] “China Produced 271 GW Crystalline Silicon Solar Modules During H1 2024,” *Taiyang News*, 2024. <https://taiyangnews.info/markets/china-produced-271-gw-crystalline-silicon-solar-modules-during-h1-2024> (last accessed in May 2025).

- [15]J. Czochralski, "Ein neues Verfahren zur Messung der Kristallisationsgeschwindigkeit der Metalle," *Zeitschrift für physikalische Chemie*, vol. 92, pp. 219–221, 1918.
- [16]K. Bothe, R. Sinton, J. Schmidt, "Fundamental boron-oxygen-related carrier lifetime limit in mono- and multicrystalline silicon," *Progress in Photovoltaics: Research and Applications*, vol. 13, pp. 287–296, 2005, doi: 10.1002/pip.586.
- [17]W. G. Pfann, "Zone-refining," *Trans. AIME*, vol. 194, 1952.
- [18]B. Chalmers, H.E. LaBelle, A.I. Mlavsky, "Edge-defined, film-fed crystal growth," *Journal of Crystal Growth*, vol. 13–14, pp. 84–87, 1972, doi: 10.1016/0022-0248(72)90067-X.
- [19]M.A. Green, "Self-consistent optical parameters of intrinsic silicon at 300K including temperature coefficients," *Solar Energy Materials and Solar Cells*, vol. 92, no. 11, pp. 1305–1310, 2008, doi: 10.1016/j.solmat.2008.06.009.
- [20]"Perc solar cells", <https://pv-manufacturing.org/perc-solar-cells/> (last accessed in May 2025).
- [21]M. A. Green, "The path to 25% silicon solar cell efficiency: History of silicon cell evolution," *Prog. Photovolt: Res. Appl.*, vol. 17, pp. 183–189, 2009, doi: 10.1002/pip.892.
- [22]Y. Zhao, et al., "Strategies for realizing high-efficiency silicon heterojunction solar cells," *Sol. Energy Mater. Sol. Cells*, vol. 258, 2023, doi: 10.1016/j.solmat.2023.112413.
- [23]"Unveiling the Future: TOPCon Solar Cell Technology", *EcoGreenEnergy*, Champs-sur-Marne, France. <https://ecogreenenergy.com/unveiling-the-future-topcon-solar-cell-technology/> (last accessed in May 2025).
- [24]S.W. Glunz, F. Feldmann, A. Richter, M. Bivour, C. Reichel, H. Steinkemper, J. Benick, M. Hermle, "The irresistible charm of a simple current flow pattern – 25% with a solar cell featuring a full-area back contact," *Proceedings of the 31st European Photovoltaic Specialists Conference and Exhibition, Hamburg, Germany*, pp. 259–263, 2015.
- [25]M. D. Lammert, R. J. Schwartz, "The interdigitated back contact solar cell: A silicon solar cell for use in concentrated sunlight," *IEEE Transactions on Electron Devices*, vol. 24, pp. 337–342, 1977, doi: 10.1109/T-ED.1977.18738.
- [26]A. Smets, K. Jäger, O. Isabella, R. van Swaaij, M. Zeman, "Solar Energy - The physics and engineering of photovoltaic conversion, technologies and systems," *UIT Cambridge, England*, 2016.
- [27]Dirk-Holger Neuhaus, A. Münzer, "Industrial Silicon Wafer Solar Cells," *Advances in OptoElectronics*, 2007, doi: 10.1155/2007/24521.
- [28]P. A. Basore, "Defining terms for crystalline silicon solar cells," *Prog. Photovolt: Res. Appl.*, vol. 2, pp. 177–179, 1994, doi: 10.1002/pip.4670020213.

- [29]Y. M. Yang, A. Yu, B. Hsu, W. C. Hsu, A. Yang, C. W. Lan, "Development of high-performance multicrystalline silicon for photovoltaic industry," *Prog. Photovolt: Res. Appl.*, vol. 23, pp. 340–351, 2015, doi: 10.1002/pip.2437.
- [30]S. Reiter, et al., "Parasitic Absorption in Polycrystalline Si-layers for Carrier-selective Front," *Junctions. Energy Procedia*, vol. 92, pp. 199–204, 2016, doi: 10.1016/j.egypro.2016.07.057.
- [31]M. A. Green, E. D. Dunlop, M. Yoshita, et al., "Solar cell efficiency tables (Version 63)," *Prog Photovolt Res Appl.*, vol. 32(1), pp. 3–13, 2024, doi: 10.1002/pip.3750.
- [32]K. L. Chopra, P. D. Paulson, V. Dutta, "Thin-film solar cells: an overview," *Progress in Photovoltaics: Research and applications*, vol. 12.2-3, pp. 69–92, 2004.
- [33]H. Kang, "Crystalline Silicon vs. Amorphous Silicon: the Significance of Structural Differences in Photovoltaic Applications," *IOP Conf. Ser.: Earth Environ. Sci.*, vol. 726, 2021, doi: 10.1088/1755-1315/726/1/012001.
- [34]A. Feltrin, et al., "An Introduction To The Technology Of Thin Film Silicon Photovoltaics," *Informacije MIDEA*, vol. 39, 2009.
- [35]A. Wang, G. Lucovsky, "PECVD: A New Thin-Film Photovoltaic Material," *Proc. IEEE Photovoltaic Specialists Conf.*, p. 1614. 5, 1990.
- [36]A. Matsuda, "Microcrystalline silicon.: Growth and device application," *J. Non-Cryst. Solids*, vol. 338–340, pp. 1–12, 2004, doi: 10.1016/j.jnoncrysol.2004.02.012.
- [37]M. Fonrodona, D. Soler, F. Villar, J. Escarré, J. M. Asensi, J. Bertomeu, J. Andreu, "Progress in single junction microcrystalline silicon solar cells deposited by Hot-Wire CVD," *Thin Solid Films*, vol. 501, pp. 247–251, 2006, doi: 10.1016/j.tsf.2005.07.146.
- [38]S. Hitoshi et al., "Thin-film microcrystalline silicon solar cells: 11.9% efficiency and beyond," *Appl. Phys. Express*, vol. 11, 2018, doi: 10.7567/APEX.11.022301.
- [39]A. Poruba, et al., "Optical Absorption and Light Scattering in Microcrystalline Silicon Thin Films and Solar Cells," *Journal of Applied Physics*, vol. 88, 2000, doi: 10.1063/1.373635.
- [40]J.S. Cashmore, et al., "Improved conversion efficiencies of thin-film silicon tandem (MICROMORPH<sup>TM</sup>) photovoltaic modules," *Solar Energy Materials and Solar Cells*, vol. 144, pp. 84–95, 2016, doi: 10.1016/j.solmat.2015.08.022.
- [41]S. Khosroabadi, R. Eghbali, A. Shokouhmand, "Enhancing efficiency in a-Si:H/ $\mu$ c-Si micromorph tandem solar cells through advanced light-trapping techniques using ARC, TRJ, and DBR," *J Mater. Sci: Mater Eng.*, vol. 19, 2024, doi: 10.1186/s40712-024-00174-8.
- [42]A. Luque, S. Hegedus, "Handbook of Photovoltaic Science and Engineering," *Ch. 13, 14*, 2011.

- [43] P. D. Antunez, D. M. Bishop, Y. Luo, R. Haight, "Efficient kesterite solar cells with high open-circuit voltage for applications in powering distributed devices," *Nat. Energy*, vol. 2, pp. 884–890, 2017.
- [44] "First Solar", <https://www.firstsolar.com/en> (last accessed in May 2025).
- [45] "First Solar achieves yet another cell conversion efficiency world record," *First Solar Press Release*, Feb. 2016.
- [46] D. Feldman, J. Hoskins, R. Margolis, "Q4 2017/Q1 2018 Solar Industry Update," *NREL/PR-6A20-71493*, NREL, 2018.
- [47] M. A. Scarpulla, et al., "CdTe-based thin film photovoltaics: Recent advances, current challenges and future prospects," *Sol. Energy Mater. Sol. Cells*, vol. 255, 2023, doi: 10.1016/j.solmat.2023.112289.
- [48] D. Kuciauskas, S. Farrell, P. Dippo, J. Moseley, H. Moutinho, J. V. Li, A. M. Allende Motz, A. Kanevce, K. Zaunbrecher, T. A. Gessert, D. H. Levi, W. K. Metzger, E. Colegrove, S. Sivananthan, "Charge-carrier transport and recombination in heteroepitaxial CdTe," *J. Appl. Phys.*, vol. 116, 123108, 2014.
- [49] J. N. Duenow, W. K. Metzger, "Back-surface recombination, electron reflectors, and paths to 28% efficiency for thin-film photovoltaics: A CdTe case study," *J. Appl. Phys.*, vol. 125, 2019, doi: 10.1063/1.5063799.
- [50] Prashun Gorai et al., "A search for new back contacts for CdTe solar cells," *Sci. Adv.*, vol. 9, 2023, doi: 10.1126/sciadv.ade3761.
- [51] J. Burst et al., "Carrier density and lifetime for different dopants in single crystal and polycrystalline CdTe," *Appl. Phys. Lett. Mater.*, vol. 4, 2016, doi: 10.1063/1.4966209.
- [52] J. M. Burst et al., "CdTe solar cells with open-circuit voltage breaking the 1 V barrier," *Nature Energy*, vol. 1, 2016, doi: 10.1038/nenergy.2016.15.
- [53] W. K. Metzger et al., "As-Doped CdSeTe Solar Cells Achieving 22% Efficiency With  $-0.23\%/^{\circ}\text{C}$  Temperature Coefficient," *IEEE J. Photovolt.*, vol. 12, no. 6, pp. 1435–1438, 2022, doi: 10.1109/JPHOTOV.2022.3201479.
- [54] M. A. Green, A. Ho-Baillie, H. Snaith, "The emergence of perovskite solar cells," *Nature Photon*, vol. 8, pp. 506–514, 2014, doi: 10.1038/nphoton.2014.134.
- [55] "Special Report on Solar PV Global Supply Chains," *IEA, OECD Publishing, Paris*, 2022, doi: 10.1787/9e8b0121-en.
- [56] M. A. Scarpulla, et al., "CdTe-based thin film photovoltaics: Recent advances, current challenges and future prospects," *Solar Energy Materials and Solar Cells*, vol. 255, 2023, doi: 10.1016/j.solmat.2023.112289.
- [57] J. E. Jaffe, A. Zunger, "Electronic structure of the ternary chalcopyrite semiconductors CuAlS<sub>2</sub>, CuGaS<sub>2</sub>, CuGaSe<sub>2</sub> and CuInSe<sub>2</sub>," *Phys. Rev. B*, vol. 29, 1984, doi: 10.1103/PhysRevB.28.5822.
- [58] M. Contreras, L. Mansfield, B. Egaas, J. Li, M. Romero, R. Noufi, E. RudigerVoigt, W. Mannstadt, "Improved Energy Conversion Efficiency in Wide Bandgap Cu(In,Ga)Se<sub>2</sub> Solar Cells," *37th IEEE Photovoltaic*

- Specialists Conference (PVSC)*, pp. 26–31, 2011, doi: 10.1109/PVSC.2011.6185837.
- [59] J. E. Granata, J. R. Sites, “Impact of sodium in the bulk and in grain boundaries of CIS,” *Proceedings of the 2nd World Conference on Photovoltaic Solar Energy Conversion, Vienna, Austria*, pp. 604–607, 1998.
- [60] F. Kessler, D. Rudmann, “Technological aspects of flexible CIGS solar cells and modules,” *Sol. Energ.*, vol. 77, pp. 685–695, 2004.
- [61] A. Chirilă, P. Reinhard, F. Pianezzi, P. Bloesch, A. R. Uhl, C. Fella, L. Kranz, D. Keller, C. Gretener, H. Hagendorfer, D. Jaeger, R. Erni, S. Nishiwaki, S. Buecheler, A. N. Tiwari, “Potassium-induced surface modification of Cu(In,Ga)Se<sub>2</sub> thin films for high-efficiency solar cells,” *Nat. Mater.*, vol. 12, 1107, 2013, doi: 10.1038/nmat3789.
- [62] T. Nakada, M. Mizutani, “18% efficiency Cd-free Cu(In,Ga)Se<sub>2</sub> thin-film solar cells fabricated using chemical bath deposition (CBD)-ZnS buffer layers,” *Jpn. J. Appl. Phys.*, vol. 41, Part 2, pp. 2–5, 2002, doi: 10.1143/JJAP.41.L165.
- [63] M. A. Mughal, R. Engelken, and R. Sharma, “Progress in Indium (III) sulfide (In<sub>2</sub>S<sub>3</sub>) buffer layer deposition techniques for CIS, CIGSSe, and CdTe-based thin film solar cells,” *Sol. Energy*, vol. 120, pp. 131–146, 2015.
- [64] P. M. P. Salomé et al., “CdS and Zn<sub>1-x</sub>Sn<sub>x</sub>O<sub>y</sub> buffer layers for CIGS solar cells,” *Sol. Energy Mater. Sol. Cells*, vol. 159, pp. 272–281, 2017, doi: 10.1016/j.solmat.2016.09.023.
- [65] M. Nakamura, K. Yamaguchi, Y. Kimoto, Y. Yasaki, T. Kato, H. Sugimoto, “Cd-free Cu (In,Ga)(Se,S)<sub>2</sub> thin-film solar cell with a new world record efficacy of 23.35%,” *IEEE Journal of Photovoltaics*, vol. 9, pp. 1863–1867, 2019, doi: 10.1109/JPHOTOV.2019.2937218.
- [66] B. Sweetman, “F-22 Raptor,” *MBI Publishing Company*, p. 48, ISBN 978-1-61060-143-6, 1998.
- [67] Danny H.W. Li, Gary H.W. Cheung, Joseph C. Lam, “Analysis of the operational performance and efficiency characteristic for photovoltaic system in Hong Kong,” *Energy Conversion and Management*, vol. 46, no. 7–8, pp. 1107–1118, 2005, doi: 10.1016/j.enconman.2004.06.029.
- [68] A. Guechi, M. Chegaar, “Effects of diffuse spectral illumination on microcrystalline solar cells,” *J. Electron Devices*, vol. 5, pp. 116–121, 2007.
- [69] C. Droz, J. Roux, S.B. Rouelle, P. Valitutti, P.R. Beljean, “Mastering the spectrum in class A pulsed solar simulators,” *Proceedings of the 23rd EUPVSEC, Valencia*, pp. 326–9, 2008.
- [70] “Photovoltaic devices - Part 1: Measurement of photovoltaic current-voltage characteristics,” *IEC 60904-1:2020, International Electrotechnical Commission, Geneva, Switzerland*, 2020.
- [71] C. Sorasan, P. Taladriz-Blanco, L. Rodriguez-Lorenzo, B. Espiña, R. Rosal, “New versus naturally aged greenhouse cover films: Degradation



- and micro-nanoplastics characterization under sunlight exposure,” *Science of The Total Environment*, vol. 918, 2024, doi: 10.1016/j.scitotenv.2024.170662.
- [72] Y. K. Song, S. H. Hong, S. Eo, W. J. Shim, “The fragmentation of nano- and microplastic particles from thermoplastics accelerated by simulated-sunlight-mediated photooxidation,” *Environmental Pollution*, vol. 311, 2022, doi: 10.1016/j.envpol.2022.119847.
- [73] K. K. Philippe, R. Timmers, R. van Grieken, J. Marugan, “Photocatalytic Disinfection and Removal of Emerging Pollutants from Effluents of Biological Wastewater Treatments, Using a Newly Developed Large-Scale Solar Simulator,” *Industrial & Engineering Chemistry Research*, vol. 55 (11), pp. 2952–2958, 2016, doi: 10.1021/acs.iecr.5b04927.
- [74] Á. García-Gil, M. D. Molina-Ramírez, R. A. García-Muñoz, R. Marasini, L. Buck, K. G. McGuigan, J. Marugán, “Weathering of plastic SODIS containers and the impact of ageing on their lifetime and disinfection efficacy,” *Chemical Engineering Journal*, vol. 435, Part 1, 2022, doi: 10.1016/j.cej.2022.134881.
- [75] R. M. Sayre, J. C. Dowdy, “Examination of solar simulators used for the determination of sunscreen UVA efficacy,” *Photochem Photobiol*, vol. 86(1), pp. 162–167, 2010, doi: 10.1111/j.1751-1097.2009.00633.x.
- [76] G. Seckmeyer, H. D. Payer, “A new sunlight simulator for ecological research on plants,” *Journal of Photochemistry and Photobiology B: Biology*, vol. 21, no. 2–3, pp. 175–181, 1993, doi: 10.1016/1011-1344(93)80180-H.
- [77] F. Ghetti, H. Herrmann, D.-P. Häder, H.K. Seidlitz, “Spectral dependence of the inhibition of photosynthesis under simulated global radiation in the unicellular green alga *Dunaliella salina*,” *Journal of Photochemistry and Photobiology B: Biology*, vol. 48, no. 2–3, pp. 166–173, 1999, doi: 10.1016/S1011-1344(99)00043-3.
- [78] M. Barron, C. Hankins, L. Courtney, D. Marcovich, “Experimental Bleaching of a Reef-Building Coral Using a Simplified Recirculating Laboratory Exposure System,” *Journal of Marine Biology*, 2010, doi: 10.1155/2010/415167.
- [79] A. Gallo, A. Marzo, E. Fuentealba, E. Alonso, “High flux solar simulators for concentrated solar thermal research: A review, Renewable and Sustainable,” *Energy Reviews*, vol. 77, pp. 1385–1402, 2017, doi: 10.1016/j.rser.2017.01.056.
- [80] M. Tawfik, X. Tonnellier, C. Sansom, “Light source selection for a solar simulator for thermal applications: A review,” *Renewable and Sustainable Energy Reviews*, vol. 90, pp. 802–813, 2018, doi: 10.1016/j.rser.2018.03.059.
- [81] L. Edwards, P. Torcellini, “Literature Review of the Effects of Natural Light on Building Occupants,” 2002, doi: 10.2172/15000841.
- [82] J. Xu, J. R. Woodyard, “Investigation of carbon arc source as an AM0 solar simulator for use in characterizing multijunction solar cells,”

- Proceedings of Conference Record of the Twenty-Eighth IEEE Photovoltaic Specialists Conference*, pp. 1324–1327, 2000, doi: 10.1109/PVSC.2000.916135.
- [83] R. Shankar, W. J. Shim, J. G. An, U. H. Yim, “A practical review on photooxidation of crude oil: Laboratory lamp setup and factors affecting it,” *Water. Res.*, vol. 68, pp. 304–315, 2015, doi: 10.1016/j.watres.2014.10.012.
- [84] J. W. Graham Jr., D. W. Healy Jr., “NASA Spece Environment Test Chamber and Solar Radiation Simulator, Final report,” *NASA technical documents, nasa\_techdoc\_19620000769*, 1961.
- [85] W. Wang, B. Laumert, “Simulate a ‘sun’ for solar research: a literature review of solar simulator technology,” *KTH Royal Institute of Technology*, 2014.
- [86] “‘94123A-CPV Solar Simulator’, Newport Corporation”, California, USA. <https://www.newport.com/p/94123A-CPV> (last accessed in January 2025).”
- [87] “SPIRE XENON Manufacturing and Laboratory solar Flasher”, *Eternal Sun, The Hague, The Netherlands*.  
<https://www.eternalsun.com/product/large-area-xenon-flash-solar-panel-simulator/> (last accessed in January 2025).
- [88] “SciSun Solar Simulator, AM0, 50 × 50 mm”, *Sciencetech inc., Ontario, Canada*.  
<https://www.sciencetech-inc.com/shop/product/160-9109-scisun-am0-scisun-solar-simulator-am0-class-aaa-50-50-mm-32288?category=46> (last accessed on January 2025).
- [89] “SS-X50 Solar Simulator”, *Trokutsolutions, Thane, India*.  
<https://trokutsolutions.com/ss-x-series> (last accessed in January 2025).
- [90] “Xenon Arc Accelerated Weathering Test Chamber”, *Xi’an LIB Environmental Simulation Industry, Shaanxi, China*.  
<https://www.lib-testchamber.com/accelerated-weathering-xenon-arc-test-chamber/> (last accessed in January 2025).
- [91] R. J. Matson, K.A. Emery, R.E. Bird, “Terrestrial solar spectra, solar simulation and solar cell short-circuit current calibration: a review,” *Solar Cells*, vol. 11, pp. 105–145, 1984, doi: 10.1016/0379-6787(84)90022-X.
- [92] R. A. Olson, J. H. Parker, “Carbon arc solar simulator,” *Applied Optics*, vol. 30 (10), pp. 1290–1293, 1991, doi: 10.1364/AO.30.001290.
- [93] G. Leary, G. Switzer, G. Kuntz, T. Kaiser, “Comparison of xenon lamp-based and LED-based solar simulators,” *IEEE 43rd Photovoltaic Specialists Conference (PVSC)*, pp. 3062–3067, 2016, doi: 10.1109/PVSC.2016.7750227.
- [94] J. P. Roba, N. P. Siegel, “The design of metal halide-based high flux solar simulators: Optical model development and empirical validation,” *Solar Energy*, vol. 157, pp. 818–826, 2017, doi: 10.1016/j.solener.2017.08.072.

- [95] D. Codd, A. Carlson, J. Rees, A. Slocum, "A low cost high flux solar simulator," *Solar Energy*, vol. 84, 2010, doi: 10.1016/j.solener.2010.08.007.
- [96] E. Bigaila, E. Rounis, P. Luk, A. Athienitis, "A Study of a BIPV/T Collector Prototype for Building Façade Applications," *Energy Procedia*, vol. 78, pp. 1931–1936, 2015, doi: 10.1016/j.egypro.2015.11.374.
- [97] H. Sabahi, A. Asghar, I. Mirzaee, H. Bungypoor-fard, "Design , construction and performance test of an efficient large-scale solar simulator for investigation of solar thermal collectors," *Sustain ENERGY Technol ASSESSMENTS*, vol. 15, pp. 35–41, 2016, doi: 10.1016/j.seta.2016.03.004.
- [98] A.L. Andrady, "Plastics and the Environment," pp. 339–352, 2003.
- [99] S.H. Choi, S.J. Scotti, K.D. Song, H. Ries, "Transpiring cooling of a scram-jet engine combustion chamber," *Proceedings of 32nd AIAA thermophysics conference, Atlanta, GA*, 1997.
- [100] D. Hirsch, P. V. Zedtwitz, T. Osinga, et al., "A new 75 kW high-flux solar simulator for high-temperature thermal and thermochemical research," *J. Sol. Energy Eng.*, vol. 125(1), pp. 117–120, 2003, doi: 10.1115/1.1528922.
- [101] J. F. Waymouth, "Electric discharge lamps (Monographs in Modern Electrical Technology)," *MIT Press, Cambridge, MA*, 1971.
- [102] J.T.C. van Kemenade, R.A.J. Keijser, B.F. Bolt, "New Possibilities for HPS Lamps in Indoor Lighting," *Journal of the Illuminating Engineering Society*, vol. 16:1, pp. 150–161, 1987, doi: 10.1080/00994480.1987.10748675.
- [103] A. Martín, N. Bordel, C. Blanco, J. C. Alvarez Anton and G. Zissis, "Comparison of the Emission of a High-Pressure Sodium Lamp Working at 50 Hz and at High Frequency," *IEEE Transactions on Industry Applications*, vol. 46, no. 5, pp. 1740–1745, Oct. 2010, doi: 10.1109/TIA.2010.2059610.
- [104] X. Guo, X. Hao, J. Zheng, C. Little, S. Khosla, "Response of greenhouse mini-cucumber to different vertical spectra of LED lighting under overhead high pressure sodium and plasma lighting," *Acta horticulturae*, vol. 1134, pp. 87–94, 2016, doi: 10.17660/ActaHortic.2016.1134.12.
- [105] J. M. Dudley, G. Genty, S. Coen, "Supercontinuum generation in photonic crystal fiber," *Rev. Mod. Phys*, vol. 78, pp. 1135–1184, 2006, doi: 10.1103/RevModPhys.78.1135.
- [106] T. Dennis, J. Schlager, K. Bertness, "A Novel Solar Simulator Based on a Supercontinuum Laser for Solar Cell Device and Materials Characterization," *IEEE Journal of Photovoltaics*, vol. 4, pp. 1119–1127, 2014, doi: 10.1109/JPHOTOV.2014.2321659.
- [107] M. Mundus, M. K. Dasa, X. Wang, J. Hohl-Ebinger, W. Warta, "Spectrally Shaped Supercontinuum for Advanced Solar Cell Characterization," *European Photovoltaic Solar Energy Conference and*

- Exhibition (EU PVSEC)*, 2015, doi: 10.4229/EUPVSEC20152015-2DO.4.6.
- [108] N. Papež, R. Dallaev, P. Kaspar, D. Sobola, P. Škarvada, Š. Ťálu, S. Ramazanov, A. Nebojsa, "Characterization of GaAs Solar Cells under Supercontinuum Long-Time," *Illumination. Materials*, vol. 14, 2021, doi: 10.3390/ma14020461.
- [109] L. S. Alban, J. Chen, S. Wang, X. Hao, M. Islam, T. Kato, H. Sugimoto, K. Akimoto, T. Sakurai, "Wavelength dependent J-V characteristics of  $\text{CuIn}_{1-x}\text{Ga}_x(\text{S,Se})_2$  solar cells and carrier recombination," *Applied Physics Express*, vol. 12, 2019, doi: 10.7567/1882-0786/ab1ad8.
- [110] T. Dennis, B. Fisher, M. Meitl J. Wilson, "A high-concentration programmable solar simulator for testing multi-junction concentrator photovoltaics," *IEEE 42nd Photovoltaic Specialist Conference (PVSC)*, New Orleans, LA, USA, pp. 1–5, 2015, doi: 10.1109/PVSC.2015.7356196.
- [111] L. Lombez, D. Ory, M. Paire, A. Delamarre, G. El Hajje, J. F. Guillemoles, "Spectrally Resolved Light Beam Induced Current on CIGS Solar Cells," *EUPVSEC*, 2013.
- [112] C. D. Elvidge, D. M. Keith, ; B. T. Tuttle, K. E. Baugh, "Spectral Identification of Lighting Type and Character," *Sensors*, vol. 10 (4): 3961–398, Apr. 2010, doi: 10.3390/s100403961.
- [113] A. Georgescu, G. Damache, M.A. Girtu, "Class A small area solar simulator for dye-sensitized solar cell testing," vol. 10, pp. 3003–3007, 2008.
- [114] D. Bickler, "The simulation of solar radiation," *Solar Energy*, vol. 6(2), 64–68, 1962, doi: 10.1016/0038-092x(62)90006-3.
- [115] F. Hussain, M. Y. H. Othman, B. Yatim, et al., "Fabrication and Irradiance Mapping of a Low Cost Solar Simulator for Indoor Testing of Solar Simulator for Indoor Testing of Solar Collector," *Journal of Solar Energy Engineering*, vol. 133, 2011, doi: 10.1115/1.4004548.
- [116] F. Aksoy, H. Karabulut, C. Çınar, H. Solmaz, Y.Ö. Özgören, A. Uyumaz, "Thermal performance of a Stirling engine powered by a solar simulator," *Appl Therm Eng*, vol. 86:161–7, 2015.
- [117] C. Landrock, B. Omrane, J. Aristizabal, B. Kaminska, C. Menon, "An Improved Light Source Using Filtered Tungsten Lamps as an Affordable Solar Simulator for Testing of Photovoltaic Cells," *Proceedings of IEEE 17th international mixed signals, sensors and systems test workshop (IMS3TW)*, vol. 153–158, 2011.
- [118] A. Namin, C. Jivacate, D. Chenvidhya, et al., "Construction of tungsten halogen, pulsed LED, and combined tungsten halogen-LED solar simulators for solar cell i - V characterization and electrical parameters determination," *Int. J. Photoenergy*, 2012, doi: 10.1155/2012/527820.
- [119] M. Guvench, C. Gurcan, K. Durgin, D. MacDonald, "Solar simulator and I-V measurement system for large area solar cell testing," *ASEE Annual Conference Proceedings*, 2004.

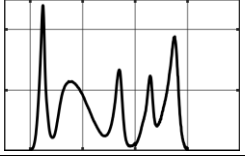
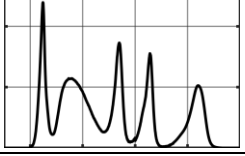
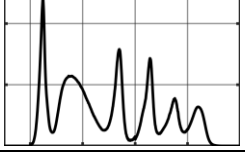
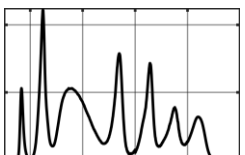
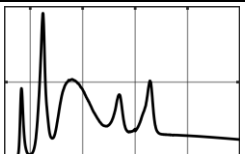
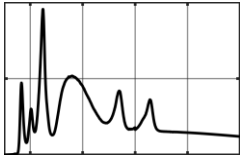
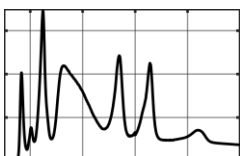
- [120] G. Routledge, "Lighting the way to a low-energy future," *IEE Review*, vol. 48(5), pp. 21–25, 2002, doi: 10.1049/ir:20020503.
- [121] J. R. Richter, R. Van Buskirk, C. Dalhammar, P. Bennich, "Optimal durability in least life cycle cost methods: the case of LED lamps," *Energy Efficiency*, vol. 12, pp. 107–121, 2019, doi: 10.1007/s12053-018-9662-4.
- [122] "Sol3A Class AAA Solar Simulators", Newport Corporation, California, USA. <https://www.newport.com/f/class-aaa-solar-simulators> (last accessed in June 2025).
- [123] S. Kohraku, K. Kurokawa, "New methods for solar cells measurement by LED solar simulator," *Proceedings of 3rd World Conference on Photovoltaic Energy Conversion, Osaka, Japan*, vol. 2, pp. 1977–1980, 2003.
- [124] D. Kolberg, F. Schubert, N. Lontke, A. Zwigart, D. M. Spinner, "Development of tunable close match LED solar simulator with extended spectral range to UV and IR," *Energy Procedia*, vol. 8, pp. 100–105, 2011, doi: 10.1016/j.egypro.2011.06.109.
- [125] J. Heerlein, M. Behringer, C. Jäger, "Near-infrared power LED for emerging security and defence applications," *Proc. SPIE 8186, Electro-Optical Remote Sensing, Photonic Technologies, and Applications V, 81860O*, Oct. 2011, doi: 10.1117/12.897992.
- [126] L.L. Han, C.H. Du, W.H. Gong, X.S. Tang, Z.W. Wang, R.Z. Zhai, Z.Q. Jia, "High-reflectivity composite metal substrate for high-power IRLED," *Results in Physics*, vol. 61, 2024, doi: 10.1016/j.rinp.2024.107784.
- [127] Y. Ma, et al., "Cr<sup>3+</sup> activated Gd<sub>3</sub>Sc<sub>2</sub>Al<sub>3</sub>O<sub>12</sub> garnet phosphor ceramic with broadband emissions and enhanced thermal stability toward high-power near-infrared LED/LD," *Ceramics International*, vol. 50, no. 15, pp. 26624–26633, 2024, doi: 10.1016/j.ceramint.2024.04.389.
- [128] B. Hamadani, K. Chua, J. Roller, M. Bennahmias, B. Campbell, H. Yoon, B. Dougherty, "Towards realization of a large-area light-emitting diode-based solar simulator," *Progress in Photovoltaics: Research and Applications*, vol. 21, pp. 779–789, 2012, doi: 10.1002/pip.1231.
- [129] K. Linden, W. R. Neal, H. Serreze, "Adjustable spectrum LED solar simulator system and method," *Light-Emitting Diodes: Materials, Devices, and Applications for Solid State Lighting XVIII, SPIE*, vol. 9003, 2014, doi: 10.1117/12.2035649.
- [130] P. Pust, P. Schmidt, W. Schinck, "A revolution in lighting," *Nature Mater*, vol. 14, pp. 454–458, 2015, doi: 10.1038/nmat4270.
- [131] A. Bazzi, Z. Klein, M. Sweeney, K. Kroeger, P. Shenoy, P. Krein, "Solid-State Solar Simulator. Industry Applications," *IEEE Transactions*, vol. 48, pp. 1195–1202, 2012, doi: 10.1109/TIA.2012.2199071.
- [132] E. López-Fraguas, J. Sánchez-Pena, R. Vergaz, "A Low-Cost LED-Based Solar Simulator," *IEEE Transactions on Instrumentation and Measurement*, pp. 1–11, 2019, doi: 10.1109/TIM.2019.2899513.

- [133] V. Esen, S. Saglam, B. Oral, , Ö. Ceylan Esen, “Toward Class AAA LED Large Scale Solar Simulator With Active Cooling System for PV Module Tests,” *IEEE Journal of Photovoltaics*, vol. 12, pp. 364–371, 2022, doi: 10.1109/JPHOTOV.2021.3117912.
- [134] “Steady State LED solar simulator”, *Eternal Sun, The Hague, The Netherlands*. <https://www.eternalsun.com/product/class-aaa-steady-state-led-based-solar-simulator/> (last accessed in January 2025).
- [135] “VeraSol-2 LED Class AAA Solar Simulator”, *Newport Corporation, California, USA*. <https://www.newport.com/f/class-aaa-led-solar-simulators> (last accessed in January 2025).
- [136] “Sunbrick™ Large Area AAA LED Solar Simulator”, *G2V Optics Inc., Edmonton, Canada*. <https://g2voptics.com/products/led-solar-simulator-sunbrick/> (last accessed in January 2025).
- [137] “LED Solar Simulator LumiSun™ 50”, *Primelite GmbH, Gruenwald, Germany*. <https://www.primelite.com/products/specialty-led-lighting/led-solar-simulator-lumisun-50> (last accessed in January 2025).
- [138] A. Al-Ahmad, D. Clark, J. Holdsworth, B. Vaughan, W. Belcher, P. Dastoor, “An Economic LED Solar Simulator Design,” *IEEE Journal of Photovoltaics*, vol. 12, 2022, doi: 10.1109/JPHOTOV.2022.3143460.
- [139] “Photovoltaic Devices - Part 9: Solar Simulator Performance Requirements,” *IEC 60904-9:2007, International Electrotechnical Commission, Geneva, Switzerland*, 2007.
- [140] E44 Committee, *Specification for Solar Simulation for Photovoltaic Testing*. doi: 10.1520/E0927-19.
- [141] H.B. Curtis, “Errors in short circuit current measurements due to spectral mismatch between sunlight and solar simulators,” *National Aeronautics and Space Administration, ERDA/NASA-1022/76/3*, 1976.
- [142] C.H. Seaman, “The correction for spectral mismatch effects on the calibration of a cell when using a solar simulator,” *JPL-PUB-81-1, Jet Propulsion Laboratory, California Inst. of Tech. Pasadena, CA, USA*, 1981.
- [143] “Download center | ams OSRAM,” *ams-OSRAM AG, Premstaetten, Austria*. <https://ams-osram.com/support/download-center?search=LZ4> (last accessed in May 2025).
- [144] “Bridgelux RS Array Series Product Data Sheet DS25. 2013.” [www.bridgelux.com/sites/default/files/resource\\_media/DS25-Bridgelux-RS-Array-Data-Sheet-2014.01.27.pdf](http://www.bridgelux.com/sites/default/files/resource_media/DS25-Bridgelux-RS-Array-Data-Sheet-2014.01.27.pdf) (last accessed March 2022).
- [145] “ANSI/IES LM-63-02 (R2008) Standard File Format for Electronic Transfer of Photometric Data and Related Information,” *Illuminating Eng. Soc. North America, New York, NY, USA*, 2008.
- [146] A. W. Stockmar, “EULUMDAT/2–Extended version of a well established luminaire data format,” *Proc. CIBSE Nat. Lighting Conf., Lancaster, U.K.*, pp. 353–362, 1998.

- [147] R. Kopecek, J. Libal, “Bifacial Photovoltaics 2021: Status, Opportunities and Challenges,” *Energies*, vol. 14, 2021, doi: 10.3390/en14082076.
- [148] “Matlab optimization toolbox,” *The MathWorks, Inc.*, 2022. [https://se.mathworks.com/help/pdf\\_doc/optim/optim.pdf](https://se.mathworks.com/help/pdf_doc/optim/optim.pdf).
- [149] J. Zhao, et al., “Simulation of Crystalline Silicon Photovoltaic Cells for Wearable Applications. IEEE Access,” *IEEE Access*, vol. 9, pp. 20868–20877, 2021, doi: 10.1109/ACCESS.2021.3050431.
- [150] J. G. Fossum, “Computer-aided numerical analysis of silicon solar cells,” *Solid-State Electronics*, vol. 19, no. 4, pp. 269–277, 1976, doi: 10.1016/0038-1101(76)90022-8.
- [151] “Three-Dimensional Optical Simulation of Textured Surface Silicon Solar Cell,” *Synopsys Inc.*, 2020.
- [152] A. Kowsar, S. Chandra Debnath, Md. Shafayet-Ul-Islam, M. Jobayer Hossain, M. Hossain, AFM K. Chowdhury, G. Hashmi, S. F. U. Farhad, “An overview of solar cell simulation tools, Solar Energy Advances,” *Solar Energy Advances*, vol. 5, 2025, doi: 10.1016/j.seja.2024.100077.
- [153] “Sentaurus technology template: EQE and I–V curve calculation of a textured silicon solar cell using the raytracer,” *Synopsys Inc.*, 2023.
- [154] “Reference air mass 1.5 spectra, 2023,” National Renewable Energy Laboratory, <https://www.nrel.gov/grid/solar-resource/spectra-am1.5.html>. (last accessed in January 2023).
- [155] Paul Basore, “About PC3D”. <https://www.pc3d.info/about-pc3d> (last accessed in January 2025).
- [156] A. Y. Al-Ahmad et al., “Modular LED arrays for large area solar simulation,” vol. 27, no. 2, pp. 179–189, Feb. 2019.
- [157] “Spectral Mismatch Calculator,” *PVLighthouse*. <https://www2.pvlighthouse.com.au/calculators/spectral%20mismatch%20calculator/spectral%20mismatch%20calculator.aspx> (last accessed on May 2025).
- [158] “International Technology Roadmap for Photovoltaic (ITRPV) - 2023 Results, 15th edition”, *VDMA Photovoltaic Equipment, VDMA*, 2023.
- [159] X. T. Zeng et al., “Influence of different parameter profiles on the formation of aluminum back surface field (Al-BSF) using for HIT solar cell,” *Proceedings of SPIE - The International Society for Optical Engineering*, vol. 7518, 2009, doi: 10.1117/12.840584.
- [160] O. Nichiporuk, A. Kaminski, M. Lemiti, A. Fave, V. Skryshevsky, “Optimisation of interdigitated back contacts solar cells by two-dimensional numerical simulation,” *Solar Energy Materials and Solar Cells*, vol. 86, no. 4, pp. 517–526, 2005, doi: 10.1016/j.solmat.2004.09.010.

## APPENDIX

### A1. Properties of simulator configurations with abbreviated names

Abbr.	Light sources and their irradiances (W/m <sup>2</sup> )	$d_1, \dots d_6$ (%)	$SPC$ (%); $SPD$ (%).	Visual cue
L4.1	c. white, 440; 740 nm, 97; 850 nm, 88; 940 nm, 211.	-10.9; -5.6; 10.9; -10.5; 5.5; 10.6.	81.2; 75.9.	
L4.2	c. white, 440; 740 nm, 127; 850 nm, 121; 1050 nm, 148.	-10.9; -5.7; 10.9; 10.9; -10.9; 5.7.	86.1; 67.8.	
L5	c. white, 440; 740 nm, 116; 850 nm, 108; 940 nm, 80; 1050 nm, 92.	-10.9; -5.6; 10.9; 2.7; -4.5; 7.5.	88.9; 63.0.	
L6	c. white, 408; 365 nm, 32; 740 nm, 116; 850 nm, 108; 940 nm, 80; 1050 nm, 92.	5.7; -12.5; 2.9; 1.4; -4.6; 7.6.	91.8; 61.1.	
H5	c. white, 339; 365 nm, 27; 740 nm, 39; 850 nm, 55; halogen, 376.	-4.6; -12.3; 12.3; -12.2; 4.6; 12.2.	97.2; 38.1.	
H6	c. white, 339; 365 nm, 28; 405 nm, 23; 740 nm, 39; 850 nm, 32; halogen, 375.	12.2; -12.2; 12.2; -12.2; -11.8; 11.8.	98.3; 34.0.	
H8	c. white, 309; 365 nm, 30; 405 nm, 14; 523 nm, 33; 740 nm, 73; 850 nm, 69; 1050 nm, 20; halogen, 375.	0; 0; 0; 0; 0; 0.	98.2; 39.5.	



## A2. Models of considered light sources.

Manufacturer and model	Color, peak wavelength	Remarks
Bridgelux: BXRA-56C9000-J	Cool white	LED array on a square PCB.
Osram (Ledengin): LZ4-40B200 LZ4-40R200 LZ4-40R300 LZ4-40R400 LZ4-40R508	455 nm 660 nm 740 nm 850 nm 940 nm	Direct color LEDs used in addition to white LED arrays to achieve A class spectrum [P1].
Osram (Ledengin): LZ4-00G108 LZ4-00A108 LZ4-00R108 LZ1-00R802	523 nm 590 nm 623 nm 1050 nm	Additional LEDs of interim wavelengths in 400 nm to 1100 nm range.
SeoulViosys: CUD4AF1B Osram (Ledengin): LZ4-04UV00 LZ4-40UB00-00U4 LZ4-40UB00-00U7	340 nm 365 nm 385 nm 405 nm	Additional LEDs for spectrum extension into UV range.
Bentham CL2	Warm white	Calibrated halogen emitter

### A3. Examples of MATLAB scripts

#### A3.1 Global analysis of PC3D modelling results

```
%Analysis of PC3D data

PC3D_EQE_failas = PC3D_AlBSF_doping_BATCH_EQE_OG; %Original
EQE values modeled with PC3D
PC3D_kint_failas = PC3D_AlBSF_doping_values_cm_3; %Values of
the variable

tech_name = "Al-BSF" ;
Batch_size = 7;
Option = 1; % Select, what is calculated (doping, thickness,
tau_n, tau_p)

clear Batch_tmp
clear Batch_legend
clear hold_SMM_minus_vienas
clear hold_uSMM

PC3D_namingas %function for graph and variable automatic
naming
%----- INTERPOLATION AND EQE PLOTTING -----
for Batch_ID = 1:Batch_size

    PC3D_EQE_interpoliacija_250219 %returns tmpEQE()
    EQE_tmp(Batch_ID,:) = tmp_EQE(1,:); %Left for EQE
plotting
    Batch_tmp(Batch_ID,:) = tmp_EQE(1,:)'.*LAMBDA' * 1e-9 *
q / (h * c) / 100; %SR recalculation

    PLOT(LAMBDA , squeeze(EQE_tmp(Batch_ID,:)))
    hold on
end

plot(LAMBDA , L6_spectrum_cSi*20 , 'k','linewidth',0.5)
plot(LAMBDA , H5_spectrum_cSi*20 , 'r','linewidth',0.5)
plot(LAMBDA , AM*20 , 'color', [0.5, 0.5
,0.5],'linewidth',0.5)

ylabel('{\itEQE} (%)')
%-----
```

```

%Calculation of SMM-1 and uSMM for all spectra
for aa = 1:6
    switch aa
        case 1
            Spectrum_name = "L4.1, ";
            spectrum = L41_spectrum;
        case 2
            Spectrum_name = "L4.2, ";
            spectrum = L42_spectrum;
        case 3
            Spectrum_name = "L5, ";
            spectrum = L5_spectrum_cSi;
        case 4
            Spectrum_name = "L6, ";
            spectrum = L6_spectrum_cSi;
        case 5
            Spectrum_name = "H5, ";
            spectrum = H5_spectrum_cSi;
        case 6
            Spectrum_name = "H8, ";
            spectrum = H8_spectrum_f0;
    end

    %----- uSMM calculation -----
    PC3D_EQE_uSMM_250219 %returns uSMM for a spectrum in each
    cycle
    hold_uSMM(aa) = uSMM;
    %-----

    %----- SMM - 1 calculation -----
    PC3D_EQE_SMM_minus_1_palyg_su_pirmu %returns SMM_minus (SMM -
    1) and plots SMM-1(k)
    hold_SMM_minus_vienas(aa,:) = SMM_minus;
    %-----
    --
end

PC3D_uSMM_spektrinimas %uSMM plotting

% ---Saving calculated values---
PC3D_AlBSF_doping_BATCH_EQE_full = EQE_tmp;
PC3D_AlBSF_doping_uSMMs_results = hold_uSMM;
PC3D_AlBSF_doping_SMM_minus_vienas_results =
hold_SMM_minus_vienas;

```

### A3.2 uSMM calculation

```
%SMM -1 calculation, according to IEC A.2 formula
set_No = 1;
SRinput = Batch_tmp';
clear SMM

for i = 1:Batch_size-1
    for j = ((i+1):Batch_size)

        SRtemp1(:) = SRinput(:,i);
        SRtemp2(:) = SRinput(:,j);

        q1 = sum((AM(:).*SRtemp1'));
        q2 = sum((spectrum(:).*SRtemp2'));
        q3 = sum((spectrum(:).*SRtemp1'));
        q4 = sum((AM(:).*SRtemp2'));

        SMM(set_No)=q1*q2/(q3*q4);
        set_No = set_No + 1;
    end
end

%uSMM calculation, according to IEC A.2 - A.4 formulae
nnn = Batch_size;
mmm = (nnn^2 - nnn) / 2;
miu = sum(SMM) / mmm;

tmpSMM = 0;

for skt1 = 1 : mmm
    tmpSMM = tmpSMM + (SMM(skt1) - miu)^2;
end

uSMM = sqrt(tmpSMM / mmm) / miu;
```

*(This page is intentionally left blank)*

## SANTRAUKA

Saulės imitatoriai yra prietaisai, skirti išmatuoti saulės elementų savybes kontroliuojamomis sąlygomis uždaroje patalpoje. Skirtingos lempų rūšys gali būti naudojamos kaip prietaiso šviesos šaltinis – įvairios dujų išlydžio lempos, halogeninės lemputės, LED šaltiniai, ar jų kombinacijos [1].

Vienas pirmųjų tyrimų, pasiekė vienos Saulės apšvietą  $200\text{ mm} \times 200\text{ mm}$  matavimo plote. Jame LED buvo panaudoti kaip halogeninių lempučių spektrą papildantys šaltiniai, sugeneruojantys iki  $590\text{ W/m}^2$  energinės apšvietos ir reikalingi  $375\text{ nm} - 680\text{ nm}$  bangos ilgių ruože [2]. Didelės galios LED šviestukų prieinamumo augimas paskatino įvairius, kartais labai skirtingus imitatorių optimizavimo sprendimus. Pavyzdžiui, pademonstruotas išskirtinai šviestukus (toliau – vien LED) naudojantis imitatorius [3], skirtas mažiems laboratoriniams prietaisams (iki  $5\text{ cm}$  dydžio) matuoti, naudojo iš viso 19 vienetų, 6 skirtingų modelių šviestukus, su žymiai supaprastintais šviesos koncentravimo sprendimais bei individualius šviestukų reflektorius.

Neseniai atnaujintas Tarptautinės elektrotechnikos komisijos (IEC) IEC 60904-9 Ed. 3 [4] standartas nustato reikalavimus saulės imitatoriams. Remiantis šiuo standartu, saulės imitatoriams suteikiamos trys klasifikuojančios raidės pagal spektrinę sudėtį, erdvinį pasiskirstymą ir laikinį stabilumą. Atitinkamai, A+, A, B, C arba U (neklasifikuojama) klasės gali būti priskiriamos prietaisui, remiantis kiekviena iš šių trijų charakteristikų, sudarant trijų raidžių kombinaciją (pvz., ABA), nurodančią imitatoriaus kuriamos apšvietos kokybę. Pagal naujausią standarto versiją, spektrinė sudėtis yra vertinama šešiuose bangos ilgių intervaluose,  $300\text{ nm} - 1200\text{ nm}$  režiuose. Vis dėlto, vertinimas pagal ankstesnes technines sąlygas, apibrėžiamas  $400\text{ nm} - 1100\text{ nm}$  intervale, vis dar yra pateikiamas atgalinio suderinamumo tikslais.

Spartus didelės galios, didelio našumo ir plataus spektrų pasirinkimo šviestukų technologijos vystymasis sudarė galimybes sukurti kompaktiškus, ekonomiškus, įvairaus masto, aukščiausios klasės vien LED imitatorius. Visgi, LED spektrų diskretiškumas ir galingų IR šviestukų trūkumas kelia naujus iššūkius, susijusius su spektriniu atitikimu.

Geometrinės saulės imitatoriaus optinių sistemų savybės bei fizikinių saulės elementų parametrų nulemti spektrų nesutapimo atvejai gali lemti neatitikimą tarp elemento veikimo testavimo metu ir naudojimo realiomis sąlygomis. Šių reiškinių skaitmeniniai tyrinėjimai suteikia įžvalgų, leidžiančių sumažinti nepageidaujamus nuokrypius.

## Darbo tikslas

Pagrindinis šio darbo tikslas – sukurti ir pademonstruoti modernius saulės imitatorius, paremtus vien puslaidininkiais šviestukais, kurie atitiktų bent AAA klasės reikalavimus, panaudojant mažiausią galimą skirtingų šviesos šaltinių tipų skaičių, ištirti spektrų nesutapimo lemtus reiškinius įvairių tipų saulės elementuose bei pateikti išsamią šių reiškinių įtakos mažinimo strategiją.

## Darbo uždaviniai

1. Sukurti ir pademonstruoti AAA klasės puslaidininkiais šviestukais paremtą saulės imitatorių, skirtą 5 colių ar didesniems pramoniniams saulės elementams, panaudojant mažiausią įmanomą pramoninėje prieinamų skirtingų šviestukų tipų skaičių, idealiu atveju – po vienos rūšies šaltinį kiekvienam intervalui, nustatymam IEC 60904-9 standarte.
2. Pateikti racionalius vien LED ar hibridinių saulės imitatorių spektro valdymo metodikas, skirtas sumažinti spektrų nesutapimo sukeltus reiškinius kristalinio silicio (c-Si), amorfinio silicio (a-Si), kadmio telūrido (CdTe) ir mikrokristalinio silicio ( $\mu$ c-Si) saulės elementuose, pasitelkiant standartizuotus spektrinius jautrius, pateikiamus IEC 60904-9 standarte.
3. Patikrinti pateiktų spektrų nesutapimo reiškinių mažinimo metodikų patikimumą, atliekant išsamius įvairių pramoninių saulės elementų tipų modeliavimus, įtraukiant legiravimo lygio, rekombinacijos parametrų ir sugėriklio sluoksnio storio įtakos tyrimus.

## Mokslinis naujumas ir svarba

Pademonstruotas modernus, modulinis ir keičiamo masto AAA klasės vien šviestukais paremtas saulės imitatoriaus dizainas leidžia testuoti pramoninius, iki 5 colių dydžio, saulės elementus, panaudojant vos 22 LED prietaisus. Šis dizainas atveria kelią ekonomiškam ir našiam skirtingų dydžių saulės elementų ar modulių analizei. Šis lankstumas yra reikšmingas fotovoltinių technologijų tyrimams ir plėtrai, leidžiantis atlikti bandymus įvairiomis sąlygomis.

Fotosrovių nuokrypių ypatumai, spektrinio padengimo pokyčiai ir spektrų nesutapimo reiškiniai buvo detalčiai ištirti kelioms saulės elementų technologijoms, apšvietai sukurti naudojant šviestukais paremtus saulės imitatorius. Parodytas metodas, leidžiantis beveik visiškai eliminuoti spektrų nesutapimo lemtus reiškinius populiariausio tipo (c-Si) pramoninių saulės elementuose. Pademonstruota, jog tai pasiekti galima tikslingai pritaikius vos

du papildomus – 365 nm ir 1050 nm smailės bangos ilgio LED tipus. Panaši efektyvi metodika, pagrįsta UV šviestukų taikymu, pasiūlyta ir CdTe bei mikrokristalinio silicio technologijų saulės elementams.

Atlikta eilė išsamių fizikinių reiškinių saulės elementuose modeliavimų, keičiant legiravimo lygį, sugėriklio sluoksnio storį ir krūvininkų gyvavimo trukmę, elementą apšviečiant šviestukais paremtais saulės imitatoriais. Šių modeliavimų rezultatai patvirtina pasiūlytų spektrų nesutapimo reiškinių mažinimo metodikų efektyvumą platesniame kontekste, nei reikalauja supaprastinti pavyzdžiai einamajame IEC 60904-9:2020 standarte.

## Darbo struktūra

Ši disertacija susideda iš literatūros apžvalgos, metodikos, rezultatų ir apibendrinimo.

Literatūros apžvalgoje (*1 skyrius*) trumpai apžvelgiami saulės elementai ir saulės imitatoriai, didesnę dėmesį skiriant silicio saulės elementams ir LED paremtiems saulės imitatoriams. Taip pat apžvelgiami einamieji saulės imitatorių standartai su įvairių parametrų įvertinimo specifikacija.

Metodika (*2 skyrius*) apžvelgia reikalingus ir naudotus duomenis bei įrankius, siekiant sumodeliuoti saulės imitatoriaus energinės apšvietos bei spektrinius skirstinius, o taip pat, saulės elementų išorinį kvantinį našumą ir voltamperines charakteristikas. Šiame skyriuje dar apžvelgiamos sistemos, naudotos sukonstruotų saulės imitatorių savybėms išmatuoti.

Rezultatų skyrius (*3 skyrius*) apima tris pagrindines dalis, suskirstytas į septynis poskyrius. Poskyris 3.1 nagrinėja vien LED saulės imitatoriaus konstravimą ir tobulinimą, panaudojant dvigubą reflektorių sistemą. Poskyriai 3.2 – 3.5 gilinasi į spektrų nesutapimo reiškinių mažinimą vien LED bei hibridinių (papildytų halogeninėmis lemputėmis) saulės imitatorių dizainams, pasitelkiant mažiausią įmanomą skirtingų šviesos šaltinių tipų skaičių, idealizuoto spektrinio jautrio c-Si, a-Si,  $\mu$ c-Si ir CdTe saulės elementų kontekste. Poskyris 3.6 tyrinėja fizikinių saulės elementų parametrų įtaką spektrų nesutapimo sukeltiems reiškiniams. Išsamiai įvertinti legiravimo lygio, sugėriklio storio ir krūvininkų gyvavimo trukmės svyravimai Al-BSF, PERC ir IBC saulės elementuose.

Apibendrinimas (*4 skyrius*) reziiumuoja energinės apšvietos skirstinio, spektrinio pasiskirstymo bei saulės elementų fizikinių parametrų svyravimų modeliavimų rezultatus.



## Autoriaus indėlis

Autorius sukūrė pirmojo pateikto saulės imitatoriaus prototipą ir išmatavo jo sugeneruotos energinės apšvietos bei spektrinį skirstinius. Autorius taip pat atliko visus spektrinio skirstinio bei saulės elementų atsako modeliavimus, panaudojant POV-Ray, MATLAB ir PC3D programinę įrangą.

Konceptą ir metodiką sukūrė prof. dr. Vincas Tamošiūnas (Vilniaus universiteto Fotonikos ir nanotechnologijų institutas); antrojo imitatoriaus dizainą užbaigė dr. Klemensas Laurinavičius (Fizikos ir technologijos mokslų centras); abu imitatorius sukonstravo dr. Algirdas Novičkovas (Vilniaus universiteto Fotonikos ir nanotechnologijų institutas); saulės elementų atsako modeliavimus, naudojant TCAD programinę įrangą atliko Dariusš Antonovič ir prof. dr. Eugenijus Gaubas (Vilniaus universiteto Fotonikos ir nanotechnologijų institutas).

## Ginamieji teiginiai

1. Vos 22 LED šaltiniai yra reikalingi siekiant apšviesti  $14\text{ cm} \times 16\text{ cm}$  plotą AAA klasės reikalavimus saulės imitatoriams atitinkančia apšvieta  $400\text{ nm} - 1100\text{ nm}$  bangos ilgių ruože, naujajame saulės imitatoriuje, pateiktame šiame darbe ir su juo susijusioje publikacijoje.
2. A+ klasės spektras, kaip apibrėžta IEC 60904-9:2020 standarte, gali būti sukurtas panaudojant vos keturis skirtingus pramoninių LED tipus (šaltai baltą,  $740\text{ nm}$ ,  $850\text{ nm}$  ir  $1050\text{ nm}$ ).
3. Kristalinio silicio saulės elementų atveju, spektrų nesutapimas *SMM* – 1 gali būti sumažintas bent eile, prie pirmojo šviestukų komplekto pridėjus du papildomus  $365\text{ nm}$  bei  $940\text{ nm}$  LED tipus.
4. Tas pats šešių šviesos šaltinių tipų komplektas gali būti optimizuotas ir CdTe bei  $\mu\text{c-Si}$  saulės elementams, pasiekiant mažesnes *SMM* – 1 vertes lyginant su komerciniais Xe lempų saulės imitatoriais.
5. Optimizacijos rezultatų, naudojant idealizuoto išorinio kvantinio našumo spektrus, pateiktus IEC 60904-9:2020 standarte, naudingumas yra patvirtintas detalesniais pramoninių c-Si saulės elementų modeliavimais, atsižvelgiant į legiravimo lygio, rekombinacijos parametrų ir sugėriklio storio svyravimus.

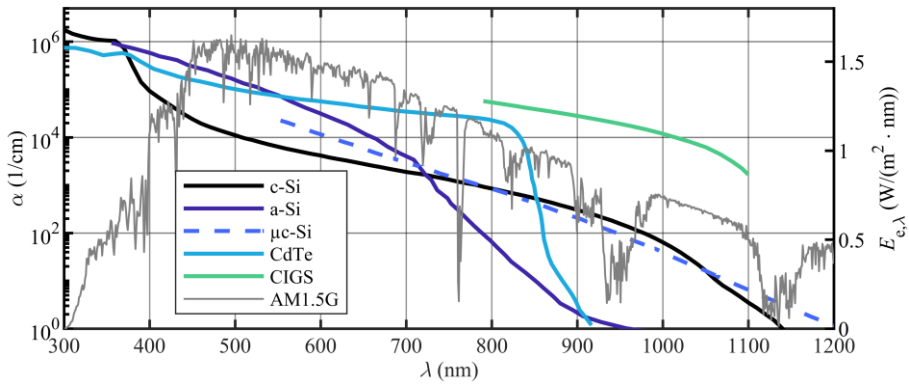
### *Saulės elementai*

Saulės elementai – fotovoltiniai prietaisai, tiesiogiai konvertuojantys saulės energiją į elektros energiją, be tarpinių termovariklių ar besisukančių mechanizmų. Judančių dalių nebuvimas stipriai sumažina fotovoltinių saulės modulių priežiūros reikalavimus ir prailgina tarnavimo trukmę, jie generuoja energiją neišmesdami į aplinką šiltnamio efektą stiprinančių ar kitų dujų bei neskleidžia triukšmo.

Pasaulinė fotovoltinių prietaisų generuotina galia per 2022 m. – 2023 m. išaugo nuo 1.2 TW iki 1.6 TW ir šiuo metu sudaro 5.3 % suminės pasaulinės generuojamos galios [5]. Atsinaujinanti energetika išlieka vienu geriausių sprendimų klimato kaitai stabdyti, kol vidutinė pasaulinė temperatūra ir išmetami į aplinką šiltnamio efektą skatinančių dujų kiekiai kasmet pasiekia naujas aukštumas (+1.28°C [7] ir 40 GtCO<sub>2</sub>e [5] atitinkamai, 2024 metais). Būtent dėl to, fotovoltinių sistemų ir susijusių technologijų (saulės imitatorių, energijos keitimo ir kaupimo prietaisų, energijos perdavimo) tyrimai tampa vis aktualesni.

Pirmasis saulės elementas buvo sukurtas iš kristalinio silicio (c-Si). Silicis pasižymi plačiu sugerties spektru (1 pav.), praktiškai padengiančiu saulės apšvietos spektrą, geromis elektrinėmis savybėmis, yra lengvai prieinamas ir nesudėtingai apdirbamas. Dėl šių priežasčių, c-Si paremtos technologijos sudaro apie 97 % pasaulinės rinkos. Taip pat, sukurta daug įvairių prietaisų dizainų, iš kurių populiariausi – Al-BSF (aliuminio užpakalinio paviršiaus lauko), PERC (pasyvuoto emiterio galinio kontakto), IBC (šukinių galinių kontaktų), ir jų kombinacijos. Kristalinio silicio technologijomis paremti saulės elementai gali pasiekti 26 % našumą, tačiau tam dažniausiai reikia apie 100 μm šviesą sugeriančio sluoksnio storio [29].

Kitos silicio formos taip pat pasižymi geromis optinėmis, tačiau prastesnėmis elektrinėmis savybėmis. Todėl amorfinis silicis (a-Si) ir mikrokristalinis silicis (μc-Si) geriausiai tinka plonasluoksnių saulės elementų gamybai, įskaitant kelių sluoksnių įvairiatarpių sandūrų technologijas, aprėpiančias platų apšvietos spektrą ir galinčias pasiekti 14 % našumą [37].



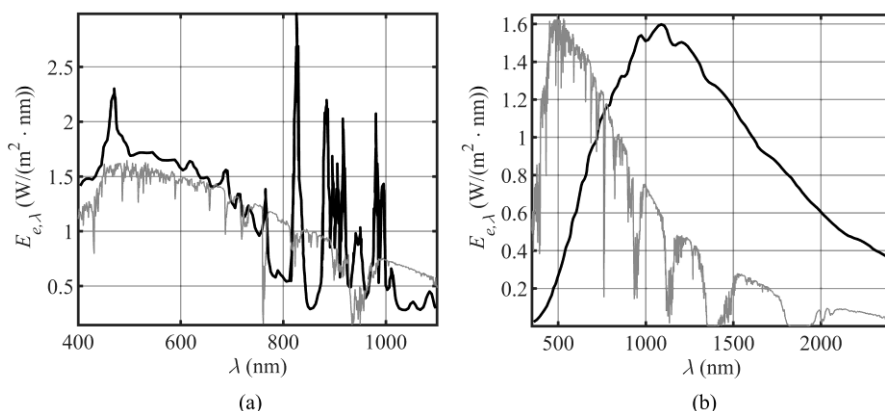
1 pav. Kristalinio silicio (c-Si) [16], amorfinio silicio (a-Si) [30], mikrokristalinio silicio ( $\mu$ c-Si) [35], CdTe ir CIGS [50] sugerties spektrai, kartu su AM1.5G etaloniniu energinės apšvietos spektru.

CdTe sugėrikliu paremtos saulės elementų technologijos yra puikus pavyzdys, kaip nauji apdirbimo metodai gali praplėsti didelės sugerties spektrinę sritį medžiagoje. Praeityje šiuos 16 % našumo prietaisus sudarydavo paprastos struktūros iš variu legiruoto CdTe sugėriklio ir kadmio sulfido (CdS) buferinio sluoksnių. Šiuolaikinius CdTe saulės elementus gali sudaryti laipsniško draustinių energijų tarpo ir legiravimo lygio sugėrikliai su alternatyviais buferiniais sluoksniais ir papildomais galiniais kontaktais, taip sumažinant krūvininkų rekombinaciją sandūrose ir sudarant galimybę pasiekti net 25 % našumą [44]. Nuo 2018 m. CdTe saulės elementų apimtys smarkiai išaugo, o gamintojai bando pasiekti 20 GW metinę gamybą, kas atitinka šiuo metu iš viso įdiegtų CdTe saulės elektrinių generuojamos galios kiekius.

Kita perspektyvi plonasluoksnių elementų technologija – vario-indžio-galio-selenido/sulfido (CIGS) junginiu paremti prietaisai. Šis tiesiatarpis lydinys pasižymi labai gera sugertimi (1 pav.) ir, reguliuojant elementų santykį ( $[\text{Cu}(\text{In}_x\text{Ga}_{1-x})(\text{Se}_y\text{S}_{1-y})]$  junginyje, galimybe keisti draustinių energijų tarpo plotį, siekiant maksimalaus prietaiso našumo. Taip pat, panašios gardelių konstantų vertės leidžia lengviau suderinti gardeles tandeminiuose ar laipsniško draustinių juostų tarpo sugėriklio saulės elementuose. Vis dėlto, CIGS auginimas išlieka sudėtingu procesu, ypač apsunkinant didelio ploto elementų gamybą, o retųjų žemės elementų poreikis daro CIGS technologiją brangesne už CdTe. Dėl to CIGS technologija niekada nepasiekė 2 GW pasaulinės gamybos ir šiuo metu netgi juntama mažėjančio pramonės susidomėjimo tendencija.

Saulės imitatoriai – prietaisai, skirti išmatuoti saulės elementų savybes kontroliuojamomis sąlygomis uždaroje patalpose. Saulės imitatoriai (kartais vadinami dirbtine saule) taip pat gali būti naudojami ir kitiems tykimams, tokiems kaip senstančių plastikų fotokaidymo [67] ar apšvietos sukeltų charakteristikų blogėjimo tyrimuose, ekologiniuose augalų, grybų ar bakterijų tyrimuose [72], koncentruotos saulės šviesos energetikos tyrimuose [75]. Tuo pačiu, geros kokybės dirbtinė šviesa pastatuose gerina gyventojų sveikatą, produktyvumą ar saugą, padidinant vitamino D pasisavinimą, spalvų atgavą ir bendrą apšvietos kiekį [77].

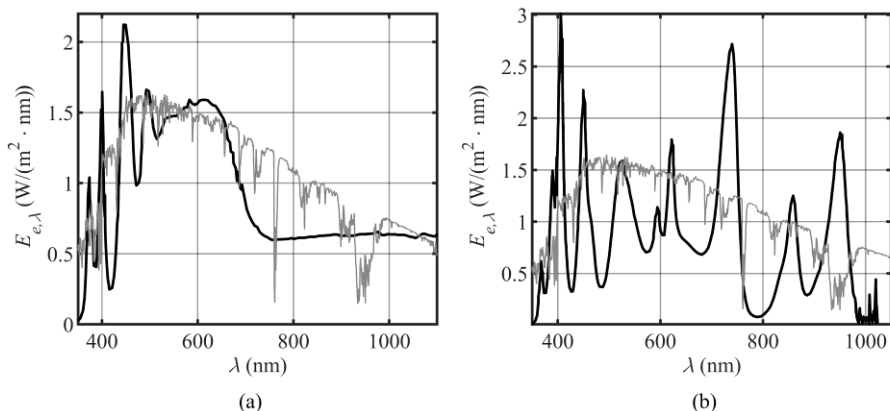
Šiuo metu populiariausi pramoniniai saulės imitatoriai vis dar naudoja ksenono (Xe) išlydžio lempas su filtrais [82]. Elektros lanko išlydžio didelio slėgio (iki 40 bar) jonizuotose Xe dujose [81] sukurta šviesa pasižymi itin plačiu spektru, įskaitant UV sritį (2a pav.). Tačiau didelis elektros energijos suvartojimas, trumpa tarnavimo trukmė, nuolatinės priežiūros poreikis ir saugumo sumetimai lemia lėtą, bet kryptingą šios technologijos atsisakymą.



2 pav. (a) Ksenono dujų išlydžio lempos [89] ir (b) kvarco-volframo halogeninės lemputės [108] energinės apšvietos spektrai.

Apie 2000 m. LED technologija smarkiai ištobulėjo, dėl ko puslaidininkiniai šviestukai pradėti naudoti nebe tik prietaisų įjungimo indikacijai, bet ir kaip pagrindiniai šviesos šaltiniai [116]. Lyginant su kitais šaltiniais, LED pasižymi ilgesniu tarnavimo laiku, greitesniu atsaku ir spartesne stabilizacija; fiziniu patvarumu, nuodingų medžiagų nebuvimu ir bendrai didesne sauga dėl mažesnių darbinių temperatūrų ir slėgių [116]. Pirmieji LED saulės imitatoriai pademonstruoti 2003 m. [117], o 2009 m. Bliss *et al.* pristatė šviestukais paremtą saulės imitatorių (3a pav.), sudarytą iš

kelių šimtų, 8 rūšių šviestukų, apimančių 375 nm – 680 nm bangos ilgių sritį, o IR sričiai padengti panaudojo halogenines lemputes (2b pav.).



3 pav. LED šaltiniais paremtų saulės imitatorių energinės apšvietos spektrai, kuriuos pademonstravo (a) Bliss et al. (2009) [2] ir (b) López-Fraguas et al. (2019) [125].

Didelės galios LED šaltiniai pradėjo rasti tik nuo 2010 m. [119], o didelės galios IR šviestukai vis dar tobulinami. Šiuo metu LED šaltiniais paremti pramoniniai saulės imitatoriai yra lengvai prieinami ir atitinkantys aukščiausius stabilumo, tolygumo ir spektrinės sutapties standartų reikalavimus. Visgi, diskretusis spektro pobūdis, mažesnės kainos ar didesnio masto imitatorių poreikis [125], o taip pat augantys standartų reikalavimai, ypatingai spektrinio padengiamumo, nuokrypių ir spektrų nesutapimo srityse, LED paremtų saulės imitatorių nišai kelia naujus iššūkius ir tyrimų kryptis.

### *Naudoti standartai ir įrankiai*

Tam, kad šviesos šaltinis būtų pripažintas saulės imitatoriumi, jis turi būti įvertintas pagal vieną iš šių standartų:

- IEC 60904-9 Edition 3 (2020) Photovoltaic Devices – Part 9: Classification of solar simulator characteristics [4];
- JIS C 8904-9 (2017), Part 9: Solar Simulator Performance Requirements (paremtas IEC 60904-9 Ed. 2 (2007) standartu [132]);
- ASTM E 927-19 (2019) Standard Specification for Solar Simulation for Electrical Performance Testing of Photovoltaic Devices [133].

Šie standartai apibrėžia reikalingas prietaiso charakteristikas ir metodus jų įvertinimui ir klasifikacijai. Šiame darbe išskirtinai remiamasi IEC 60904-9 standartu. Pagal naujausią šio standarto versiją, saulės imitatoriai gali būti klasifikuojami į A+, A, B ir C klases pagal tris kriterijus: maksimalų spektrinį nuokrypį, erdvinį netolygumą, ir laikinį apšvietos nestabilumą. Įvertinus šiuos

parametrus atskirai, saulės imitatoriui priskiriama atitinkama trijų raidžių kombinacija (pvz., ABA) nusakanti jo kuriamos energinės apšvietos kokybę.

1 lentelė. Saulės imitatorių klasifikavimo kriterijai [4].

Klasė	Maksimalus spektrinis nuokrypis (SID)	Erdvinis netolygumas (NU)	Laikinis apšvietos nestabilumas	
			Trumpalaikis (STI)	Ilgalaikis (LTI)
A+	0,875 – 1,125	1 %	0,25 %	1 %
A	0,75 – 1,25	2 %	0,5 %	2 %
B	0,6 – 1,4	5 %	2 %	5 %
C	0,4 – 2,0	10 %	10 %	10 %

Naujausioje IEC 60904-9 Ed. 3 versijoje įtraukti keli svarbūs pakeitimai:

- Spektrinio atitikimo klasifikavimo režiai praplėsti nuo 400 nm – 1100 nm iki 300 nm – 1200 nm;
- Įtraukta nauja A+ klasė;
- Apibrėžti papildomi parametrai spektrinės apšvietos įvertinimui.

2 lentelė. „Senojo“ ir atnaujinto IEC standarto nustatyti bangos ilgių intervalų skirstinys.

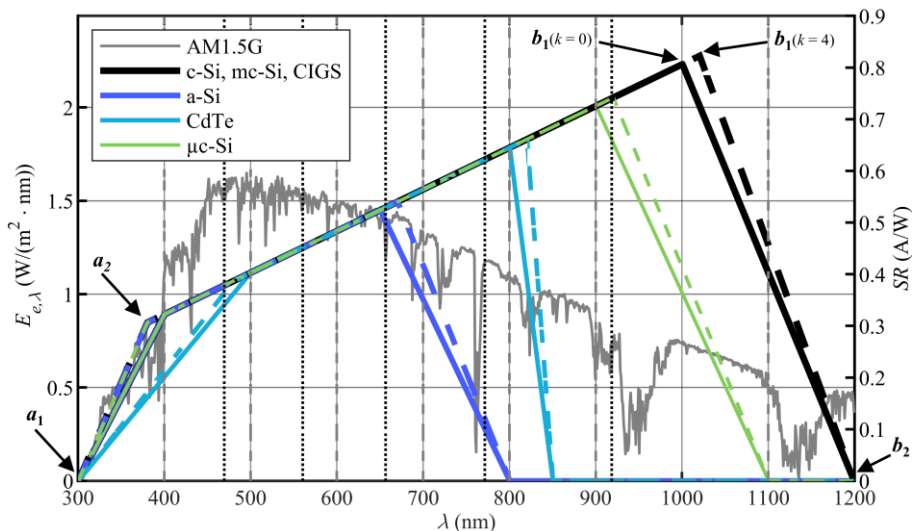
Intervalas	1	2	3	4	5	6
IEC 60904-9 Edition 2 (2007)						
Bangos ilgių režiai (nm)	400 – 500	500 – 600	600 – 700	700 – 800	800 – 900	900 – 1100
Bendros apšvietos dalis	18,4 %	19,9 %	18,4 %	14,9 %	12,5 %	15,9 %
IEC 60904-9 Edition 3 (2020)						
Bangos ilgių režiai (nm)	300 – 470	470 – 561	561 – 657	657 – 772	772 – 919	919 – 1200
Bendros apšvietos dalis	16,61 %	16,74 %	16,67 %	16,63 %	16,66 %	16,69 %

Vienas iš naujai įtrauktų parametru – spektrų nesutapimas (angl. *Spectral Mismatch*, *SMM*) – įvertina galimus voltamperinių charakteristikų matavimo neatitikimus apšvietai naudojant skirtingus šaltinius ir matuojant skirtingos, ar netgi tos pačios technologijos saulės elementus. Nors šiuo metu įvertinant imitatorius nėra reikalaujama pateikti šio (ir kitų naujai įvestų spektrinės apšvietos) parametro vertės, standartas pateikia du atvejus galimam spektrų nesutapimo įvertinimui – žinomo spektrinio jautrio „realiems“ saulės elementams, ir atvejams, kai prietaisų spektriniai jautriai nėra žinomi.

Pirmuoju atveju, nustatomas jautris spektrų nesutapimo reiškiniams (*uSMM*), kuris yra statistinis spektrų nesutapimo įvertinimas, naudojant bent

keturis fotovoltinius prietaisus. Pagal Eq. (8) apskaičiavus spektrų nesutapimą visoms prietaisų poroms, arba visų prietaisų poroms palyginant su atskaitiniu prietaisu, jautris atitinka verčių standartinį nuokrypį, ir apskaičiuojamas pagal Eq. (9).

Kai matuojamų prietaisų spektrinis jautris nėra žinomas, imitatoriaus įvertinimui galima naudoti virtualius spektrinius jautrius su nedidelėmis verčių sklaidomis ties jautrio kraštais (pvz.,  $x = 5$  nm, Eq. (10) ir Eq. (11)). Vertės, skirtos šešių skirtingų technologijų spektriniam jautriui modeliuoti yra pateikiamos standarte (4 pav.), o imitatoriaus spektro patikimumas įvertinamas kaip spektrų nesutapimo funkcija nuo sklaidos ( $SMM(k) - 1$ ) kurios mažesnis polinkio koeficientas indikuoja didesnį spektro patikimumą.



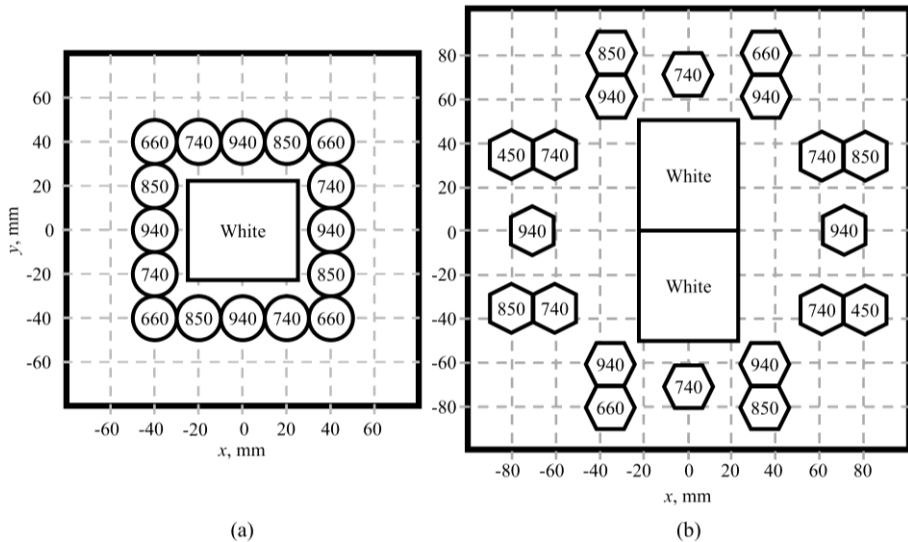
4 pav. AM1.5G etaloninis spektras (pilkos vertikalios punktyrinės linijos nurodo „senojo“ standarto intervalus [132], taškinės linijos – atnaujintojo standarto [4] intervalus) ir virtualūs įvairių saulės elementų technologijų sugerties spektrai. Punktyrinės linijos atspindi verčių sklaidą  $x = 5$  nm, kai  $k = 4$ .

Šiame darbe skaitmeniškai nagrinėjami imitatorių patikimumai naudojant MATLAB programinę įrangą virtualiems c-Si, a-Si, CdTe ir μc-Si spektriniam jautriams, o taip pat realiems c-Si saulės elementams, Al-BSF, PERC ir IBC technologijų atvejais, sumodeliuotais PC3D programine įranga. Taip pat, naudojant TCAD ir PC3D programines įrangas įvertintos prietaisų voltamperinės charakteristikos, apšviečiant tiriamųjų imitatorių generuojamais spektrais. Geometrinių sukonstruotųjų saulės imitatorių savybių tyrimams buvo pasitelktos MATLAB ir POV-Ray programinės įrangos.

## Rezultatai

### *Imitatoriaus dizaino geometrinis patobulinimas*

Kuriant šviestukinio saulės imitatoriaus dizainą, buvo atsižvelgta į kelis kriterijus: paprastą masto praplėtimą, minimalų šviestukų ir skirtingų jų rūšių kiekį bei kuo paprastesnes optinę bei elektrinę schemas. Skirtingai nuo anksčiau pademonstruotų šešiakampių dizainų [3, 148], šiame darbe pasirinkta kvadratinė geometrija su vertikaliais veidrodžiais. Ant aušinamos aliuminio plokštelės buvo sumontuoti 17 LED šaltinių, priklausančių penkioms skirtingoms rūšims, ir įrengta  $16 \times 16$  cm dydžio, 20 cm aukščio, maždaug 4 mm storio sidabruotų veidrodžių sistema (5a pav.). Tarpas tarp veidrodžių sistemos apačios ir matavimo plokštumos siekė 5 mm. Suregulavus šviestukų galią, siekiant geresnio atitikimo standartų reikalavimams, buvo išmatuotas energinės apšvietos skirstinys (6a pav.).



5 pav. (a) Pirmojo ir (b) antrojo saulės imitatorių dizainai ir LED smailių bangos ilgiai (nm) kiekvienam LED šaltiniui [P1]. (Juoda stora linija išorėje – vertikalus veidrodžiai)

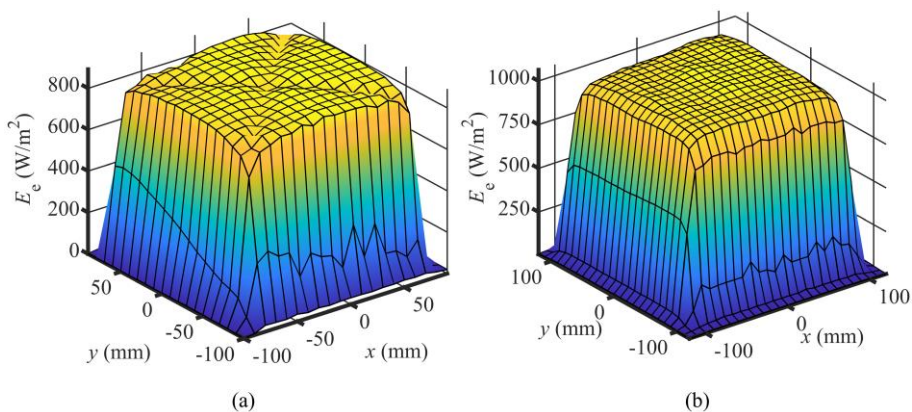
Pirmasis imitatoriaus dizainas generavo  $(820 - 892) \text{ W/m}^2$  energinę apšvietą  $11 \text{ cm} \times 11 \text{ cm}$  plote, kas atitiko minimalios energinės apšvietos reikalavimus ( $759 \text{ W/m}^2$ , 400 nm – 1100 nm bangos ilgių ruože). Tačiau dėl „X“ formos mažesnės energinės apšvietos zonos, A klasės reikalavimus atitinkantis plotas sumažėjo iki  $(8 \times 8) \text{ cm}^2$ , o mėlynos šviesos trūkumas šioje zonoje lėmė tik B klasės spektrinės sutapties atitikimą. Be to, matavimo



plokštumos kraštuose stebėtas didesnis energinės apšvietos kryptis nei prognozuota modeliavimu.

Siekiant sušvelninti nepageidaujamus reiškinius, buvo atlikti veidrodžių sistemos modeliavimai, naudojant spindulių sekimo (angl. *ray-tracing*) programinę įrangą. Nustatyta, jog atstumas tarp veidrodžių sistemos apačios ir matavimo plokštumos turi įtakos energinės apšvietos kryčio statumui. Sumažinus šį atstumą, galima tikėtis didesnės energinės apšvietos matavimo plokštumos kraštuose. Apšvietos kryčio statumą taip pat gali pagerinti veidrodžių sistemos padidėjimas ir paaukštinimas. Vis dėlto, dėl netobulo veidrodžių atspindžio gali prireikti daugiau šviestukų ir papildomų individualių reflektorių. Taip pat nustatyta, kad „X“ formos energinės ir spektrinės apšvietos sumažėjimas atsiranda dėl netobulų veidrodžių sistemos sujungimų, suklijavimo. Dėl simetriškumo tai ypač veikia centre esančio baltos LED šaltinio kuriamą apšvietą. Nuspręsta naudoti plonesnius veidrodžius su geresniais sujungimais bei pakeisti vieną centrinį baltą LED dviem greta sumontuotais šaltiniais, siekiant sumažinti nukrypimus matavimo plokštumos įžambinėse.

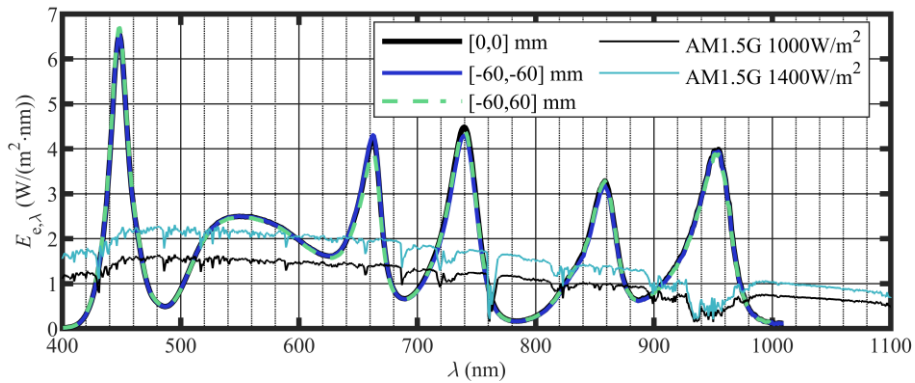
Remiantis šiais modeliavimais buvo sukurtas antrasis, 22 vienetų, 5 rūšių šviestukų imitatoriaus dizainas su 20 cm × 20 cm dydžio, 50 cm aukščio kvadratine veidrodžių sistema ir individualiais reflektoriais ant šviestukų (5b pav.). Išmatuotas šio imitatoriaus energinės apšvietos skirstinys pateiktas 6b paveiksle.



6 pav. Išmatuoti (a) pirmojo ir (b) antrojo dizainų saulės imitatorių energinės apšvietos skirstiniai [P1].

Antrojo dizaino saulės imitatoriaus energinės apšvietos skirstinys pasižymi modeliuotomis savybėmis – nebeliko „X“ formos zonos, o apšvietos kryptis matavimo plokštumos kraštuose tapo statesnis. Dėl padidėjusio montavimo ploto antrajame dizaine padvigubintas ne tik šaltai baltos LED, bet ir 750 nm

bei 940 nm šviestukų kiekis. Pirmajame dizaine šie šaltiniai veikė arti maksimalios galios ribos. Be to, didesnio aukščio veidrodžių sistema leido efektyviai sumaišyti visų šaltinių spektrinę apšvietą, net ir naudojant individualius reflektorius.

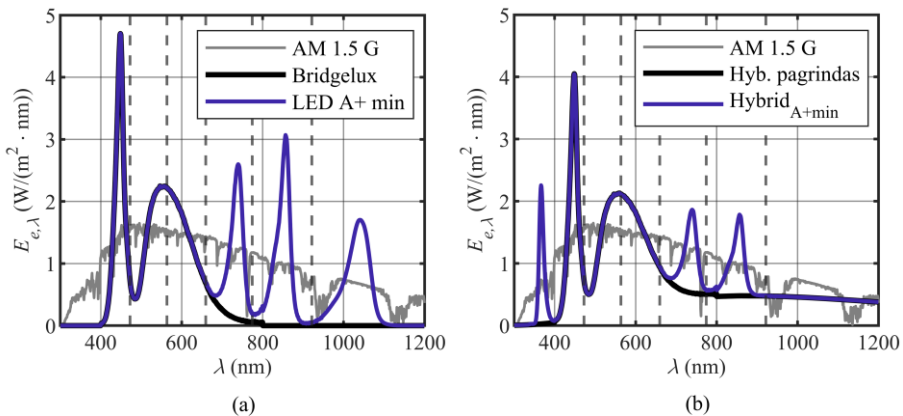


7 pav. Antrojo saulės imitatoriaus spektrai matavimo plokštumos centre ir A klasės apšvietą atitinkančio ploto kraštuose [P1].

Visi įgyvendinti patobulinimai padidino A klasės energinės apšvietos tolygumą iki 14 cm × 13 cm ploto, išlaikant beveik nepakitusią spektro sudėtį ir spektrinę sutaptį, atitinkančią A klasės reikalavimus (7 pav.).

#### *Spektrų nesutapimo faktoriaus (SMM – 1) mažinimas*

Remiantis pademonstruotais saulės imitatorių dizainais buvo atliktas spektrų nesutapimo parametrų tyrimas. Pirmiausia buvo įvertintas minimalus skirtingų šviesos šaltinių tipų skaičius, reikalingas saulės imitatoriui. Atnaujinti bangos ilgių intervalai standarte [4] lėmė, kad 660 nm šviestukas nebėra reikalingas, o šaltai baltas „Bridgelux BXRA“ LED pakankamai aprėpia pirmus tris intervalus, kad atitiktų A+ klasės spektrinės atitikties reikalavimus ( $d_1 = -12.5\%$ ,  $d_2 = -7.3\%$ ,  $d_3 = 8.6\%$ ). Ketvirtajam ir penktajam intervalui padengti vis dar tinka 740 nm ir 850 nm LED. Vien LED saulės imitatoriaus atveju, šeštajam intervalui užpildyti pridėjus 1050 nm šviestuką, pakanka vos keturių skirtingų rūšių šaltinių, kad būtų pasiekti A+ klasės spektrinės atitikties reikalavimai (8a pav.). Šiame darbe vien LED saulės imitatorių modeliai žymimi raide „L“, o hibridiniai (Hyb.) – raide „H“. Abiem atvejais po raidės sekantis skaičius, nurodys skirtingų šviesos šaltinių kiekį (apjungtąjį sutrumpintai pavadintų spektrų sąrašą galima rasti priede A1).

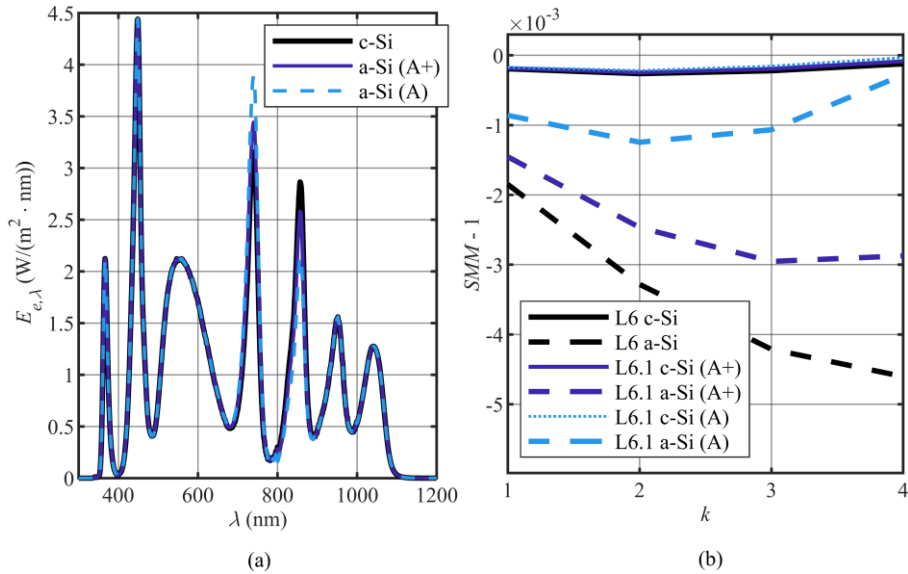


8 pav. Pirminiai sumodeliuoti A+ klasės spektrai, naudoti tolimesniam spektrų optimizavimui: (a) vien LED ( $LED_{A+min}$ ) ir (b) hibridinio ( $Hybrid_{A+min}$ ) imitatoriaus atveju. Vertikalios punktyrinės linijos atspindi bangos ilgių intervalus, numatytus naujausiame standarte [P2].

Hibridinio saulės imitatoriaus atveju, šaltai balto LED ir halogeninės lempučių kombinaciją galima naudoti kaip puikų pagrindą vėlesniems žingsniais, tačiau dėl spektrų persidengimo būtina sumažinti balto LED indėlį, siekiant išlaikyti A+ klasės spektrinę sutaptį trečiajame intervale ( $d_3 = 12.5\%$ ,  $d_2 = -10.25\%$ ). To pasekoje, pirmajame intervale atsiranda apšvietos stoka, kurią galima kompensuoti 365 nm šviestuku. Raudonojoje srityje pridėjus 740 nm ir 850 nm LED, užtenka vos 5 skirtingų rūšių šviesos šaltinių, norint atitikti A+ klasės spektrinės sutapties reikalavimus (8b pav.). Pradedant 8 pav. pateiktais spektrais, buvo įvertinti spektrinio nesutapimo efektai c-Si, a-Si, CdTe ir  $\mu$ c-Si virtualaus spektrinio jautrio saulės elementams. Svarbu pažymėti, kad bendras spektrų nesutapimas gali būti apskaičiuojamas kaip IR ir UV sričių spektrų nesutapimų suma.

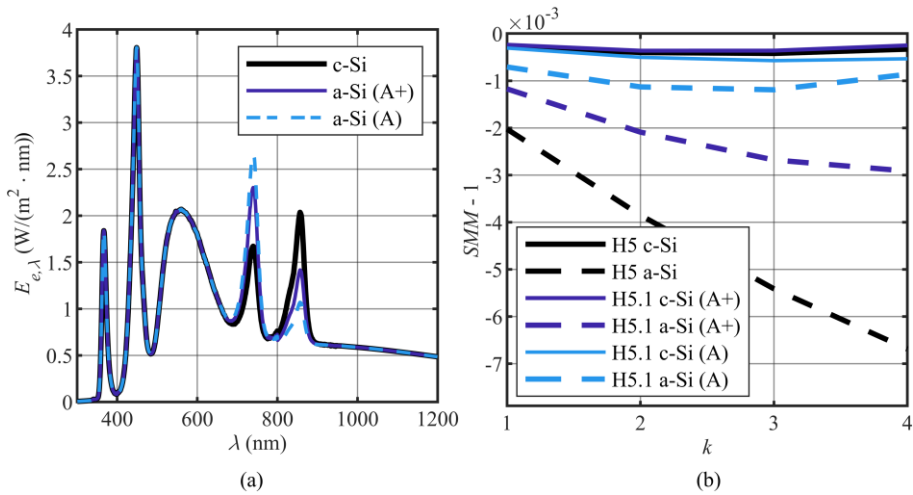
Vien LED imitatoriaus atveju, 1050 nm LED (L4.2) pakeičiant 940 nm (L4.1), sukurtas alternatyvus keturių šaltinių spektras, kurio spektrų nesutapimo funkcija c-Si saulės elementui buvo priešingo ženklo, todėl nuspręsta apjungti šiuos du atvejus į L5 imitatoriaus dizainą, taip sumažinant  $SMM - 1$  raudonojoje spektro pusėje. Tuo pačiu, pridėjus 365 nm šviestuką, sumažinamas spektrų nesutapimas UV srityje. Galiausiai buvo sumodeliuotas L6 imitatoriaus spektras, atitinkantis A+ klasės spektrinę sutaptį ir pasižymintis minimaliu  $SMM - 1$  parametru (9 pav.). Kadangi a-Si spektrinis jautris skiriasi nuo c-Si tik IR spektro pusėje, L6 spektrą galima nesudėtingai pakoreguoti, padidinant 740 nm LED indėlį ir sumažinant 850 nm indėlį, taip pasiekiant mažesnę spektrų nesutapimą abiem technologijoms lygiagrečiai. Leidžiant spektrinei sutapčiai nusileisti iki A klasės,  $SMM - 1$  galima dar

labiau sumažinti a-Si saulės elementams, be didesnės įtakos c-Si technologijai.



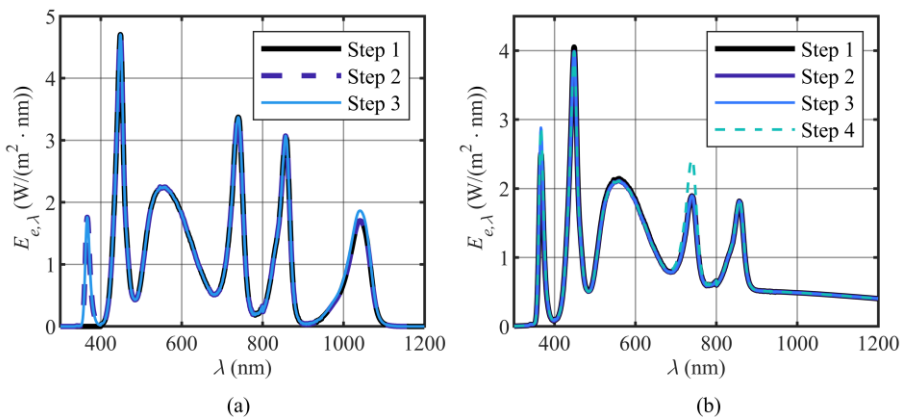
9 pav. (a) Sumodeliuoti vien LED saulės imitatoriaus spektrai (L6), optimizuojant spektrų nesutapimus vien c-Si saulės elementų technologijai, vien a-Si technologijai ir pagerinant spektrų nesutapimą a-Si technologijai, aukojant spektrinio nuokrypio klasę. (b) Spektrų nesutapimo ( $SMM-1$ ) priklausos nuo  $k$  parametro visais minėtais atvejais.

Hibridinio imitatoriaus atveju, UV šviestukas jau buvo pridėtas pirmajame komplekte, o IR sritį pilnai padengia halogeninė lemputė. Pakoregavus šaltinių galių vertes, sumodeliuotas A+ klasės spektrinės sutapties H5 imitatoriaus spektras, su minimaliu  $SMM-1$  parametru c-Si saulės elementams (10 pav.). Kaip ir vien LED imitatoriaus atveju, didinant 740 nm LED galios indėlį ir mažinant 850 nm LED galią, šį spektrą galima lygiagrečiai optimizuoti ir a-Si technologijai. Hibridiniai saulės imitatoriai pasižymi mažesniu spektrų nesutapimu, didesniu spektriniu padengiamumu (SPC) ir mažesniu spektriniu nuokrypiu (SPD).



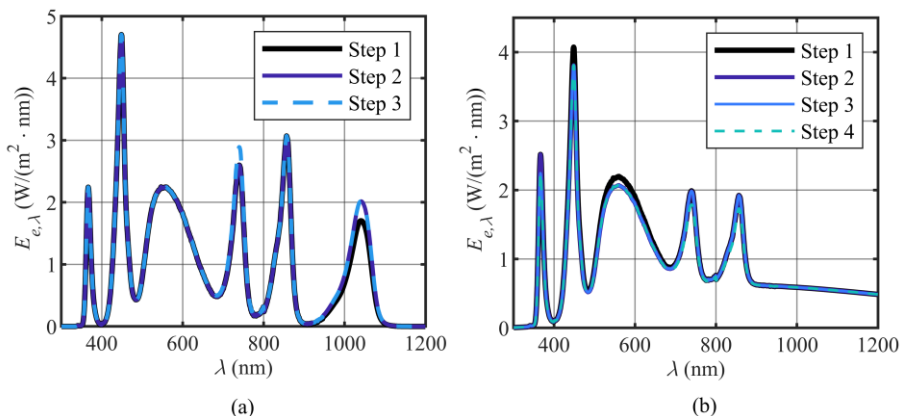
10 pav. (a) Sumodeliuoti hibridinio saulės imitatoriaus spektrai, optimizuojant spektrų nesutapimus vien c-Si saulės elementų technologijai, vien a-Si technologijai ir pagerinant spektrų nesutapimą a-Si technologijai, aukojant spektrinio nuokrypio klasę. (b) Spektrų nesutapimo (SMM – 1) priklausos nuo  $k$  parametro visais minėtais atvejais.

CdTe saulės elemento atveju, pakoreguojant esamų šviestukų galias ir, vien LED atveju, pridėjus papildomą 365 nm UV šviestuką, buvo sumodeliuoti A+ klasės spektrinę sutaptį atitinkantys vien LED ir hibridinio tipo imitatorių spektrai (11 pav.). Kadangi CdTe spektrinis jautris baigiasi ties 850 nm, skirtingai nei silicio atveju, nebuvo poreikio pridėti 940 nm LED, o 1050 nm šviestukas iš esmės reikalingas tik šeštojo intervalo energinės apšvietos užtikrinimui.



11 pav. Žingsniai (step), atlikti modeliuojant (a) vien LED ir (b) hibridinio saulės imitatorių spektrų optimizaciją CdTe saulės elementų technologijai.

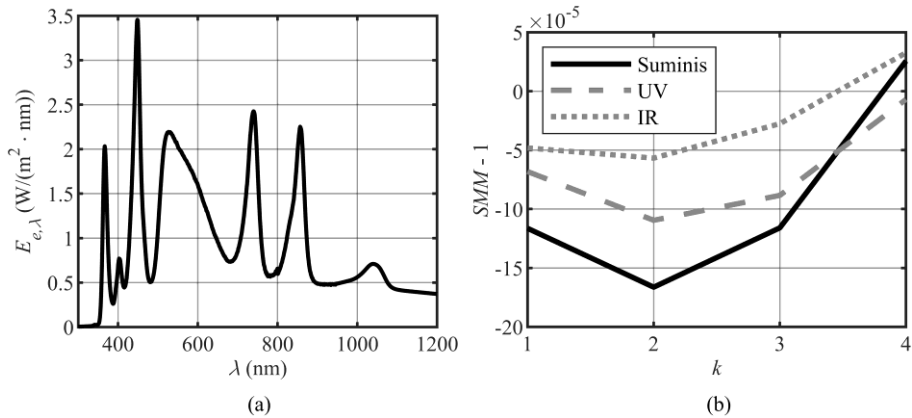
Siekiant sumažinti mikrokristalinio silicio prietaiso spektrų nesutapimą, vien LED imitatoriaus atveju pirmuoju žingsniu buvo pridėtas 365 nm šviestukas UV sričiai. Abiem imitatoriaus tipams buvo pakoreguotos esamų šaltinių galios, siekiant A+ klasės spektrinės sutapties su minimaliu  $SMM - 1$  parametru (12 pav.).



12 pav. Žingsniai (step), atlikti modeliuojant (a) vien LED ir (b) hibridinio saulės imitatorių spektrų optimizaciją  $\mu\text{-Si}$  saulės elementų technologijai.

Optimizavimo rezultatai parodė, jog siekiant kuo mažesnių spektrų nesutapimo reiškinių, skirtingoms technologijoms reikalingi šiek tiek skirtingi optimalūs spektrai, pavyzdžiui, CdTe technologijos atveju vien LED imitatoriaus dizaine reikalingi mažesnis 365 nm LED ir didesnis 740 nm LED indėliai nei  $\mu\text{-Si}$  atveju. Visgi, reikalingos šviesos šaltinių energinės apšvietos variacijos siekia vos dešimtis  $\text{W}/\text{m}^2$ , kas atveria galimybes naudoti tą patį imitatorių skirtingoms technologijom, tiesiog pakeičiant atskirų šaltinių grupių nominalią galią.

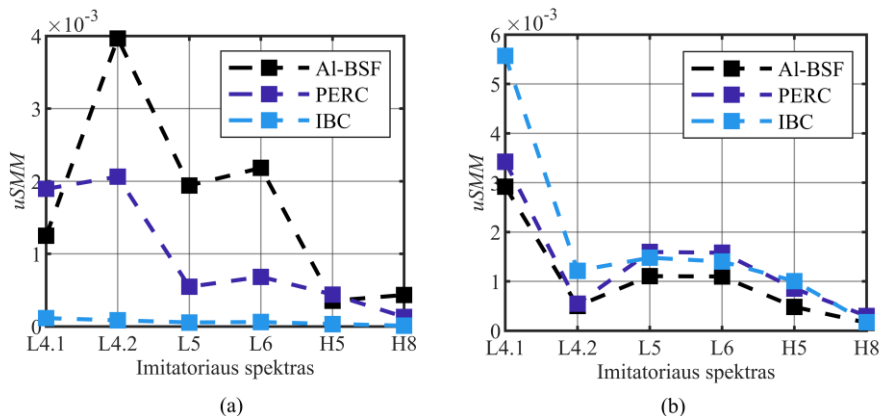
Siekiant sukurti spektrą su tobula spektrine sutaptimi ( $SID = 0$ ), buvo sumodeliuotas H8 spektras (13 pav.). c-Si atveju, 365 nm ir 405 nm šviestukų kombinacija, kartu su balto LED indėliu leidžia efektyviai sumažinti  $SMM - 1$  parametą UV srityje (ir padengti pirmojo intervalo energinės apšvietos poreikį), o halogeninės lempučių ir 1050 nm LED kombinacija leidžia sumažinti spektrų nesutapimą IR srityje (ir padengti šeštojo intervalo energinės apšvietos poreikį). Šaltai balto LED ir halogeninės lempučių kombinacija pilnai patenkina trečiojo intervalo energinės apšvietos poreikį, tačiau tuo atveju atsiranda poreikis geltonam 523 nm šviestukui – pasiekti  $d_2 = 0$ . Kaip ir kitais atvejais, 740 nm ir 850 nm šviestukų energinės apšvietos užtenka padengti ketvirtąjį ir penktąjį intervalus. Šis spektras pasižymi ne tik tobula spektrine sutaptimi, bet ir itin mažu spektrų nesutapimu, o jo spektrinis padengiamumas siekia 98 %.



13 pav. (a) Sumodeliuotas H8 hibridinio saulės imitatoriaus spektras, su tobula spektrine sutaptimi visuose intervaluose ir (b) jo spektrų nesutapimo priklausos nuo  $k$  parametro, išskiriant UV bei IR dedamąsias.

### Detalesnis silicio saulės elementų modeliavimas

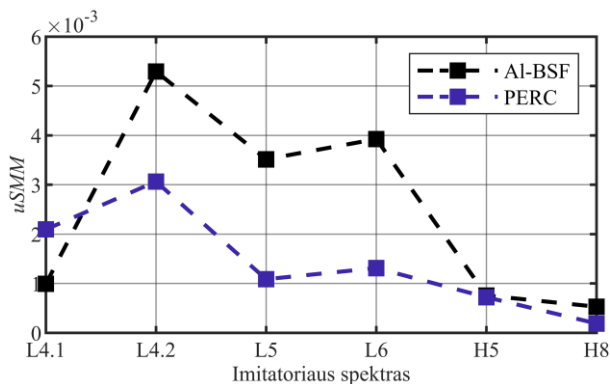
Remiantis 9 ir 10 paveiksluose pateiktais sumodeliuotais c-Si technologijai optimizuotais spektrais, buvo atlikti išsamesni skaitmeniniai modeliavimai, vertinant jautrį spektrų nesutapimo reiškiniams Al-BSF, PERC ir IBC tipo c-Si saulės elementams. Siekiant prietaisų išorinio kvantinio našumo įvairovės, įvertintos sugėriklio legiravimo lygio ir storio (14 pav.), taip pat krūvininkų gyvavimo trukmės (15 pav.) įtakos išoriniam kvantiniam našumui bei jautriui spektrų nesutapimo reiškiniams.



14 pav. Įvairių optimizuojamų imitatorių apšvietos spektrų jautris spektrų nesutapimo reiškiniams, skirtingoms saulės elementų technologijoms varijuojant (a) legiravimo lygį ir (b) sugėriklio sluoksnio storį.

Nors absoliučios vertės skiriasi, nustatyti keli dėsningumai:

- L5 ir L6 (su pridėtu 365 nm šviestuku) jautris spektrų nuokrypių reiškiniams yra labai panašus;
- Hibridiniai imitatoriai pasižymi žymiai mažesniu jautriu spektrų nuokrypių reiškiniams nei vien LED imitatoriai; H8 spektras yra mažiausiai jautrus visais atvejais;
- L4.2 spektras pasižymi didžiausiu jautriu, išskyrus atvejus, kai varijuojamas sugėriklio storis – tuomet slenkantis išorinio kvantinio našumo IR kraštas kerta 1050 nm bangos ilgį, keisdamas spektrų nesutapimo kitimo kryptį ir mažindamas rezultatų standartinį nuokrypį;
- L4.1 spektras pasižymi nestabiliu, bet dažnai mažiausiu jautriu spektrų nesutapimo reiškiniams tarp vien LED spektrų, daugiausia dėl to, jog didžiausi *EQE* pokyčiai dažnai vyksta ilgesniuose bangos ilgiuose nei 940 nm.
- Pagrindinių krūvininkų gyvavimo trukmė daro itin mažą įtaką išoriniam kvantiniam našumui, o kartu ir jautriui spektrų nesutapimo reiškiniams. Realiose IBC saulės elementuose ilgos (milisekundžių trukmės) abiejų tipų krūvininkų gyvavimo trukmės turi nykstamai mažą įtaką jautriui.

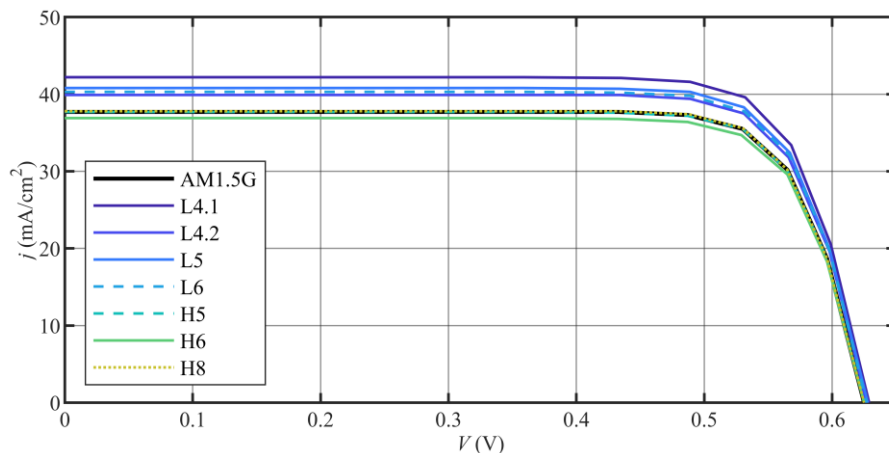


15 pav. Įvairių optimizuojamų imitatorių apšvietos spektrų jautris spektrų nesutapimo reiškiniams, skirtingoms saulės elementų technologijoms varijuojant šalutinių krūvininkų gyvavimo trukmes.

Atlikus voltamperinių charakteristikų modeliavimus nustatyta, kad tiriamų saulės imitatorių spektrai generuoja panašaus dydžio sroves c-Si saulės elementuose, lyginant su etaloniniu AM1.5G spektru (16 pav.). Tačiau vien LED imitatoriai generuoja iki 12 % didesnes fotosroves, pagrinde dėl to, jog siekiant  $1000 \text{ W/m}^2$  bendros energinės apšvietos, šie imitatoriai sugeneruoja gerokai didesnę energinę apšvietą didelio spektrinio jautrio



bangų ilgių ruože (400 nm – 1100 nm). Hibridiniai imitatoriai pasižymi gerokai artimesnėmis fotosrovės vertėmis, dėl geresnio etaloninio spektro atitikimo 1000 nm – 1200 nm bangos ilgių srityje.



16 pav. Sumodeliuotos Al-BSF saulės elemento voltamperinės charakteristikos, įvairiais optimizuojamų saulės imitatorių spektrų apšvietų atvejais.

## Apibendrinimas

1. Didelių baltų matricinių LED šaltinių ir veidrodinės „dėžės“ pritaikymas saulės imitatoriaus dizaine leidžia reikšmingai padidinti naudingai apšviečiamą plotą, palyginti su ankstesniais darbais, išlaikant panašų LED šaltinių kiekį. Naujame dizaine buvo panaudoti 22 šaltiniai vietoj 19, tačiau pasiektas šešis kartus didesnis naudingai apšviečiamas plotas, nors suvartota tik du kartus daugiau elektros energijos, palyginti su [3]. Homogenizuojantieji perimetro veidrodžiai visiškai kompensuoja koncentruotos baltos šviesos sukuriamus nepageidaujamus reiškinius. Tuo pačiu, naudojant individualius reflektorius sumažinami energinės apšvietos nuostoliai. Galiausiai buvo pasiekta AAA klasės energinė apšvieta 14 cm × 16 cm ploto matavimo plokštumoje, 400 nm – 1100 nm bangos ilgių ruože.

2. Norint pasiekti A+ klasės spektrinę sutaptį, pakanka vos keturių skirtingo tipo LED šaltinių – šalto baltos, 740 nm, 850 nm ir 1050 nm. Lyginant su ankstesniais rezultatais, spektrinių intervalų perskirstymas naujausiame standarte turėjo didelę reikšmę, nes šaltai baltos LED apšvieta leidžia padengti tris iš šešių 300 nm – 1200 nm bangos ilgių ruožo intervalų A+ klasės ribose. Taip pat nustatyta, kad kruopštus šviesos šaltinių parinkimas ir jų galios reguliavimas ties raudonos–IR srities sugerties kraštu reikšmingai sumažina  $SMM - 1$  parametą, o spektrų nesutapimo veiksnys IR srityje c-Si

saulės elementų atveju, gali būti sumažintas daugiau nei dešimt kartų, kruopščiai nustatant 940 nm ir 1050 nm šviestukų energines apšvietas.

**3.** Panašus rezultatas UV srityje gali būti pasiektas panaudojant 365 nm LED. 740 nm LED galios korekcijos turi reikšmingesnę įtaką a-Si saulės elementų atveju nei c-Si atveju. Tai yra sietina su išorinio kvantinio našumo spektro savybėmis visų tipų saulės elementų atvejais, tačiau tai gali būti išnaudojama lygiagrečiai optimizacijai dviem ar daugiau saulės elementų tipams. Vis dėlto, tokios lygiagrečios optimizacijos gali lemti mažesnę, spektrinės sutapties klasę. Mūsų imitatorių atveju, optimizuojant CdTe technologijai gali kilti iššūkių, ir siekiant mažesnio spektrų nesutapimo gali taip pat pririnkti sumažinti spektrinės sutapties klasę. Šiame darbe pasiūlyti imitatorių spektrų dizainai turėtų pasižymėti mažesniu spektrų nesutapimu, lyginant su pramoniniais Xe išlydžio lempų imitatoriais.

Deja, šiuo metu nėra pakankamai galingų ir našių IR LED šaltinių, kurių bangos ilgis viršytų 1000 nm, todėl halogeninių lempučių panaudojimas saulės imitatoriuose gali būti geras kompromisas.

**4.** Hibridinio saulės imitatoriaus atveju, panaudojant halogeninę lempuotę, pririnkia penkto tipo šviesos šaltinio. Taip yra todėl, kad halogeninių lempučių emisijos spektras persidengia su šaltai balto LED spektru, ir šaltai balto LED galia turi būti sumažinta, o UV srityje reikia pridėti 365 nm LED šaltinį, siekiant padengti pirmąjį spektrinį intervalą. Vis dėlto, tokios konfigūracijos su halogeniniu šviesos šaltiniu pasižymi reikšmingai didesniu spektriniu padengimu nei vien-LED imitatoriai, o papildomo 365 nm UV šaltinio įtraukimas padeda sumažinti spektrų nesutapimo efektus UV srityje.

Net ir optimizuojant kelioms technologijoms vienu metu, hibridiniai imitatoriai pasižymi reikšmingai mažesniu spektriniu nuokrypiu (*SPD*), o spektrinio padengiamumo (*SPC*) vertė viršija 97 % visiems nagrinėtiems saulės elementų tipams.

Naudojant A+ klasės hibridinius saulės imitatorius, su vos 5 – 6 skirtingų tipų šviesos šaltiniais, galima pasiekti mažesnę nei 2 % fotosrovės nuokrypį c-Si saulės elementuose, lyginant su etalonine AM1.5G spektrine apšvieta.

**5.** Ultravioletinio 365 nm bangos ilgio šviestuko įtraukimas į dizainą sumažina spektrų nesutapimą visų tipų saulės elementams – tiek vien LED, tiek hibridinių saulės imitatorių atvejais. Nagrinėtais atvejais šio LED šaltinio galia siekė (25 – 43) W/m<sup>2</sup>.

Keli koncepciniai eksperimentai parodė, kad optimizuotą hibridinį dizainą galima sėkmingai pritaikyti realiame saulės imitatoriuje, įtraukiant

halogeninius ir 365 nm bangos ilgio LED šaltinius. Vis dėl to norint išvystyti vien LED imitatorius, reikalingi galingesni 1050 nm LED šaltiniai. Alternatyviai, būtini reikšmingi LED šaltinių išdėstymo patobulinimai.

6. Buvo atliktas skaitmeninis spektrų nesutapimo reiškinių įvertinimas modeliuotiems c-Si saulės elementams, apšviestiems įvairių imitatorių spektrais. Ištirti Al-BSF, PERC ir IBC tipo saulės elementai, keičiant legiravimo lygį, sugėriklio sluoksnio storį ir krūvininkų rekombinacijos parametrus. Nustatyta, kad optimizacijos žingsniai, atlikti naudojant idealizuotą spektrinį jautrį, yra tinkami ir naudojant sudėtingesnius saulės elementų modelius. Tikslūs konkrečių šviestukų pritaikymai leidžia reikšmingai sumažinti jautrį spektrų nesutapimo reiškiniams nulemtiems skirtingų saulės elemento fizikinių parametrų ar netgi technologijų. Taip pat nustatyta, kad hibridiniai imitatoriai pasižymi didžiausiu patikimumu, vertinant spektrų nesutapimo jautrį įvairiomis sąlygomis. 8 skirtingo tipo šaltinių hibridinis dizainas pranoksta kitus ne tik spektrinės sutapties ar spektrų nesutapimo parametrais, bet ir sumodeliuotos trumpo jungimo srovės atitikimu c-Si saulės elementuose.

7. Šiame darbe numatyti trys iš dalies susiję ateities tyrimų keliai: lygiagretus optimizavimas įvairiems saulės elementams, naudojant A+ klasės spektrinę apšvietą generuojančius vien LED ir hibridinius saulės imitatorius; spektrų optimizacija, orientuota į kitus apšviesto saulės elemento parametrus, tokius kaip atviro jungimo įtampa ar maksimali galia; išsamus tyrimas, nagrinėjantis atskirų LED spektrų nuokrypių įtaką galimiems matavimo neapibrėžtumams.

## TRUMPOS ŽINIOS APIE DISERTANTĄ

Vardas, pavardė: Žygimantas Vosylius

Gimimo data: 1993-02-07

el. paštas: zygimantas.vosylius@ff.vu.lt

### **Išsilavinimas:**

- |              |  |
|--------------|--|
| 2011 – 2015  | Vilniaus universiteto Fizikos fakultetas,<br>Fizikos bakalauro laipsnis                                |
| 2015 – 2017  | Vilniaus universiteto Fizikos fakultetas, Medžiagotyros<br>ir puslaidininkių fizikos magistro laipsnis |
| 2019 – dabar | Vilniaus universiteto Fotonikos ir nanotechnologijų<br>institutas, fizikos doktorantūros studijos      |

### **Darbo patirtis:**

- |              |  |
|--------------|--|
| 2013 – 2018  | Vilniaus universiteto Fizikos fakulteto Puslaidininkių<br>fizikos katedra, technikas                 |
| 2018 – 2020  | Vilniaus universiteto Fotonikos ir nanotechnologijų<br>institutas, technikas                         |
| 2020 - dabar | Vilniaus universiteto Fotonikos ir nanotechnologijų<br>institutas,<br>jaunesnysis mokslo darbuotojas |

## CURRICULUM VITAE

Name, Surname: Žygimantas Vosylius

Date of birth: 1993-02-07

E-mail: zygimantas.vosylius@ff.vu.lt

### Education:

- |                |  |
|----------------|--|
| 2011 – 2015    | Vilnius University, Faculty of Physics<br>Bachelor's degree in Physics   |
| 2015 – 2017    | Vilnius University, Faculty of Physics<br>Master's degree in Physics, Materials Science and<br>Semiconductor Physics |
| 2019 – present | Vilnius University, Institute of Photonics and<br>Nanotechnology<br>PhD studies in Physics                           |

### Work experience:

- |                |  |
|----------------|--|
| 2013 – 2018    | Vilnius University, Faculty of Physics, Semiconductor<br>Physics Department,<br>Technician |
| 2018 – 2020    | Vilnius University, Institute of Photonics and<br>Nanotechnology,<br>Technician            |
| 2020 - present | Vilnius University, Institute of Photonics and<br>Nanotechnology,<br>Junior scientist      |





Vilniaus universiteto leidykla  
Saulėtekio al. 9, III rūmai, LT-10222 Vilnius  
El. p. [info@leidykla.vu.lt](mailto:info@leidykla.vu.lt), [www.leidykla.vu.lt](http://www.leidykla.vu.lt)  
[bookshop.vu.lt](http://bookshop.vu.lt), [journals.vu.lt](http://journals.vu.lt)  
Tiražas 16 egz.